POLITECNICO DI TORINO

FACOLTA' DI INGEGNERIA

Corso di Laurea Magistrale in Ingegneria Energetica e Nucleare

MASTER THESIS

Implementation and validation of a hydrodynamic analysis model in the BEMUse library for floating platforms

SUPERVISORS
Ing. Giovanni Bracco
MSc. Joseph Saverin

CANDIDATE
Vittorio Martini

ADVISOR
Prof. Giuliana Mattiazzo

October 2019

ABSTRACT

The ambitious goal set at the Climate Conference in Paris in 2015 (COP21) to try and contain the world's average temperature increment below 1.5 °C with respect to the pre-industrial era requires the introduction of more efficient and productive technologies for the exploitation of renewable energy sources in all their forms.

Among these technologies, wind power is at the moment one of the most reliable and advanced, as it's been effectively operating for decades now. Wind turbines are currently scattered all around the world, both on land and at sea. Finding a suitable installation site on land is becoming increasingly difficult in a lot of countries, though, a factor that has increased the interest in offshore solutions in recent years.

Unfortunately, current technology has quite strict requirements when it comes to the choice of a suitable site, specifically on the water depth. To increase the exploitable surface for wind energy production, the concept of floating offshore wind turbines (FOWTs) has recently gained increasing interest in the sector. As the name suggests, wind turbines are in this case mounted on floating platforms instead of being anchored to the seafloor.

This solution increases enormously the sea surface suitable for wind farms, but at the same time requires accurate simulations of the behavior and performance of the turbines, when subjected to forces and motions caused by both waves and wind.

This analysis requires precise and reliable hydrodynamic analysis softwares like WAMIT and Ansys AQWA. At the Technische Universität Berlin, a new such model called BEMUse has been developed and needs to be validated.

In this thesis, the results given by BEMUse are compared with the ones obtained with the two softwares mentioned before for a set of geometries ranging from a simple hemisphere to prototypes of platforms of great interest for commercial installations. The comparison will examine four crucial hydrodynamic parameters: added mass, radiation damping, exciting forces, and Response Amplitude Operators (RAOs).

If the results agree, BEMUse can be considered validated and can be used as an alternative to expensive softwares like WAMIT

SUMMARY

LIST OF FIGURES

LIST OF TABLES

1. INTRODUCTION

1.1 WIND ENERGY TODAY

Ever since the initial stages of the now impelling transition to green energy, wind power has always represented a vital source of clean and renewable energy, one of the main actors in the much-needed reduction of fossil fuels' predominance in the world energy mix.

Starting from the late 1980s, when the first wind farm started generating electric power in New Hampshire, USA, the industry has been on a continuous search for new markets and installation sites around the world [1].

In the last 20 years, the sector has experienced continuous and remarkable growth, with an overall installed capacity, in 2017, of 539,123 MW globally. The graph below gives an excellent overlook of this evolution during that time.

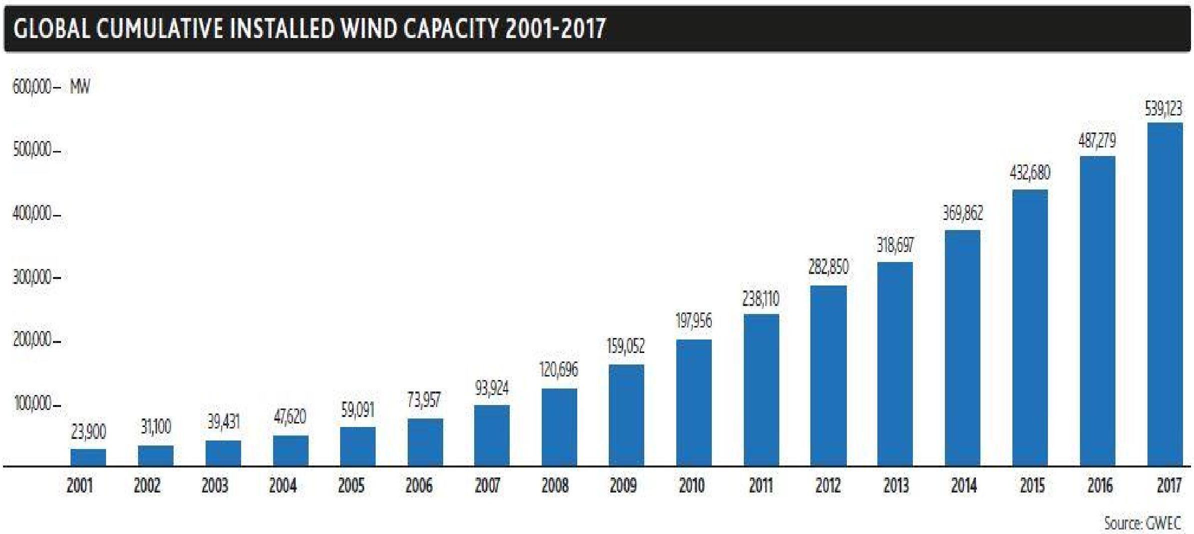

Figure 1.1 The global installed wind capacity [MW] has continuously risen over the last 17 years.

Despite the fact that in the last couple of years the annual installed capacity (new turbines built) has experienced a slight reduction, as reported in the Global Wind Report of 2017 'wind power is in a rapid transition to becoming a fully commercialized, unsubsidized technology, successfully competing in the marketplace against massively subsidized fossil and nuclear incumbents.'[1]. This kind of transition involves going through a period of adjustments, but already today wind is the most competitively priced green technology in most markets, and the rise of more advanced grid management and affordable storage devices is shaping what will be the first commercial fossil-free power sector.

The market forecasts carried out for the near future depict a promising scenario, as shown in the following figure.

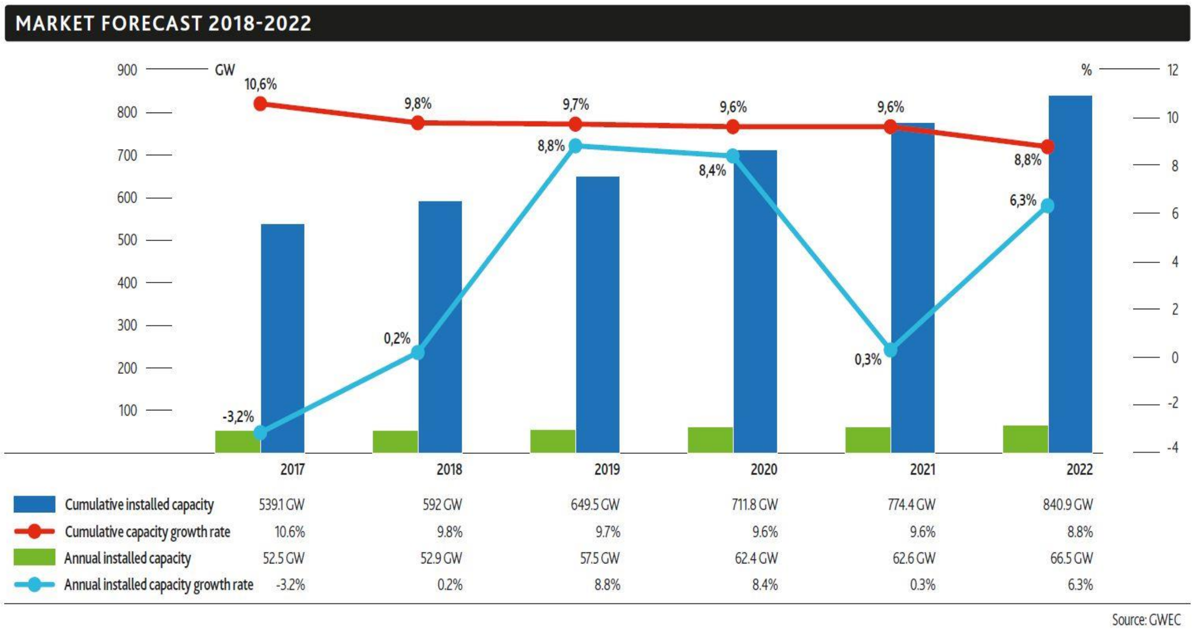

Figure 1.2. The installed capacity should grow in the near future, despite a reduction in new installations.

The main issue for wind power, like for many other renewable energy sources, lies on the discontinuity of the source, as there is no place on earth where the wind blows consistently all year long. Additionally, currently operating turbines can only produce power when the wind speed value lies between certain limits, typically 4 to 25 *m/s*. This is to prevent potential damages or excessive strains on the delicate structure. For the same reason, turbulent winds are also to be avoided.

The dominant trend has pushed towards the construction of increasingly taller towers, larger rotors and consequently more powerful turbines, which now reach stunning dimensions. To give an example, the newest prototype presented by General Electric for offshore applications is the Haliade-X, that will be 260 meters high, with 107-meter long blades and 220-meter rotor diameter, with a rated output of 12 MW [2].

This tendency has both economic and technical reasons. Larger structures allow to reduce costs, a fundamental concept of economy of scale, therefore allowing the produced electricity to be cheaper and hence more competitive on the energy market. From a technical perspective, taller turbines with larger rotors can exploit the strong, constant and steady high-altitude winds, which are not affected by the planetary boundary layer.

This concept, of capital importance in the wind power industry, is visually explained in the following figure.

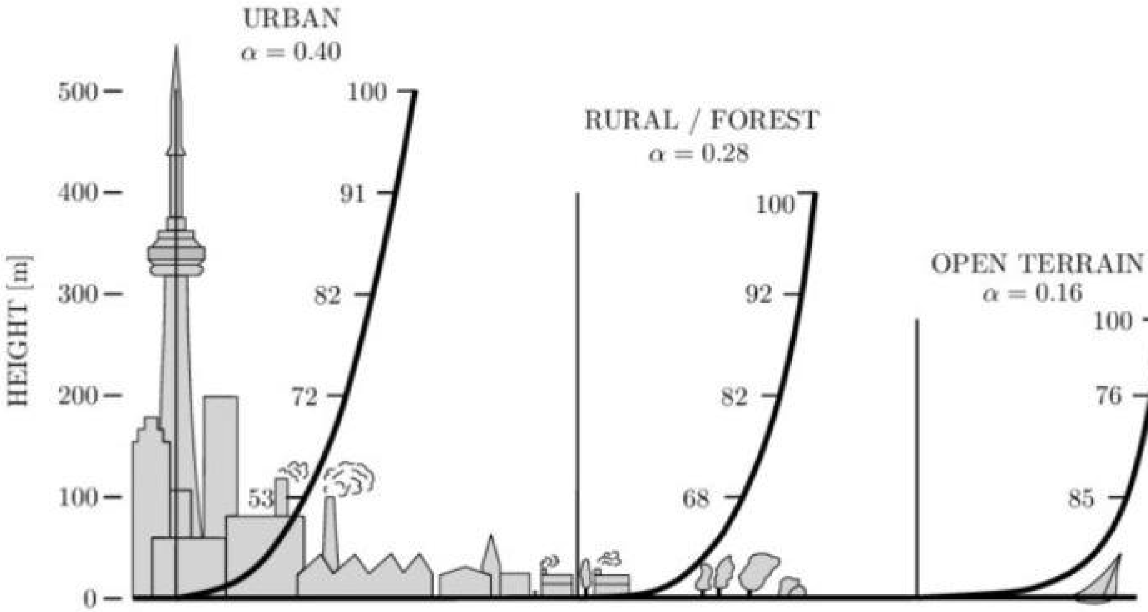

Figure 1.3. Graphical representation of the planetary boundary layer concept.

Morphological roughness, irregularity of the terrain, the presence of tall trees, buildings and mountains are all factors that tend to decrease the wind speed near the earth surface, increasing at the same time the turbulence of the flow with worsening effects both on the performance and the durability of the turbine. These issues make it increasingly challenging to find suitable installation sites for wind farms, which need large surfaces of low and flat terrain which, if not in hardly accessible areas, are often already used for farming or crop production.

All these reasons together lead to the result that despite its enormous potential, wind energy can currently rely on an average capacity factor of around 25 to 40% of the rated power [3]. To make things worse, during the years governments and wind power companies have faced vehement protests by the people living near the planned installation sites, who lamented noise and aesthetic pollution caused by the turbines.

Given all the issues illustrated so far, it is easy to understand why, after just a few years after the construction of the first wind farm, engineers and companies have focused on how to install turbines on the sea instead of on land. The reasons for that are straightforward, as the ocean offers broad, flat surfaces with no obstacles, thus reducing the detrimental effect of the planetary boundary layer. Moreover, winds blowing over the sea and oceans are usually stronger and steadier, allowing turbines to reach higher capacity factor values. Finally, it is estimated that 75% of world energy demands are concentrated in coastal areas [4].

The first operational offshore wind farm started its production in 1991 off the coast of Denmark and, given its good productivity, numerous new projects followed and in the last twenty years the installed European offshore capacity has increased, often helped by government incentives and high industrial investments, as shown in the next graph.

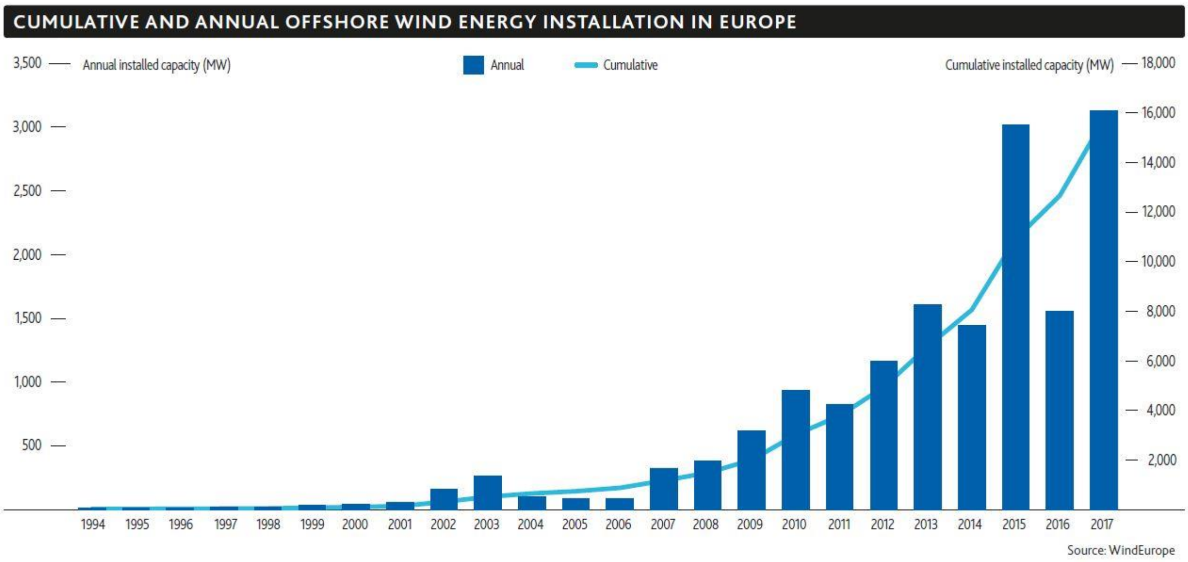

Figure 1.4. Both the cumulative and annual offshore capacity [MW] have grown enormously in the last 17 years.

Nowadays, numerous wind farms are scattered off the coast of Germany and Denmark in the North Sea.

As the technology advanced and the related costs decreased, larger wind farms have been installed at increasing distances from the coast to exploit the highly constant winds. At the same time, turbines got larger and more efficient, with some models specifically engineered for offshore applications. Given the proven potential of offshore wind power, it can seem surprising that only very few areas around the world have been considered suitable for the installation of wind farms, with a strong predominance of northern European countries. Moreover, turbines are installed near the coast, where the winds are notoriously weaker and less constant than in high-sea locations.

The main reason for that lies in the necessity to anchor the base of the structure to the seafloor, thus limiting the available sites to shallow waters, close to the shore. The installation near the coast allows, on the other hand, to contain the costs and the losses for the transmission of electric energy to the users. Another drawback is that being near the coast, the turbines are still visible by the people living there, attracting the already mentioned protests about the visual impact of such installations. Nowadays, only depths up to ca. 50 *m* are suitable with modern techniques, which are all very expensive and require specifically engineered vessels and machinery.

1.2 FLOATING OFFSHORE WIND TURBINES

Being able to exploit the enormous reserves of energy present in deeper waters would probably represent a decisive step towards the transition to a fossil-free energy sector. This urgency has led to the development, in the last few years, of a new concept: the Floating Offshore Wind Turbines (FOWTs). As the name suggests, the turbine in this case is not directly anchored to the seafloor, but instead is installed on a platform that makes it float and at the same time tries to minimize the motion caused by the action of wind and waves on the structure. The whole installation is kept in position by a mooring system anchored to the seafloor. In this way, locations with waters up to several hundred meters deep become suitable for the installation of wind farms.

In the figure, the basic concept of floating wind turbines is clearly illustrated.

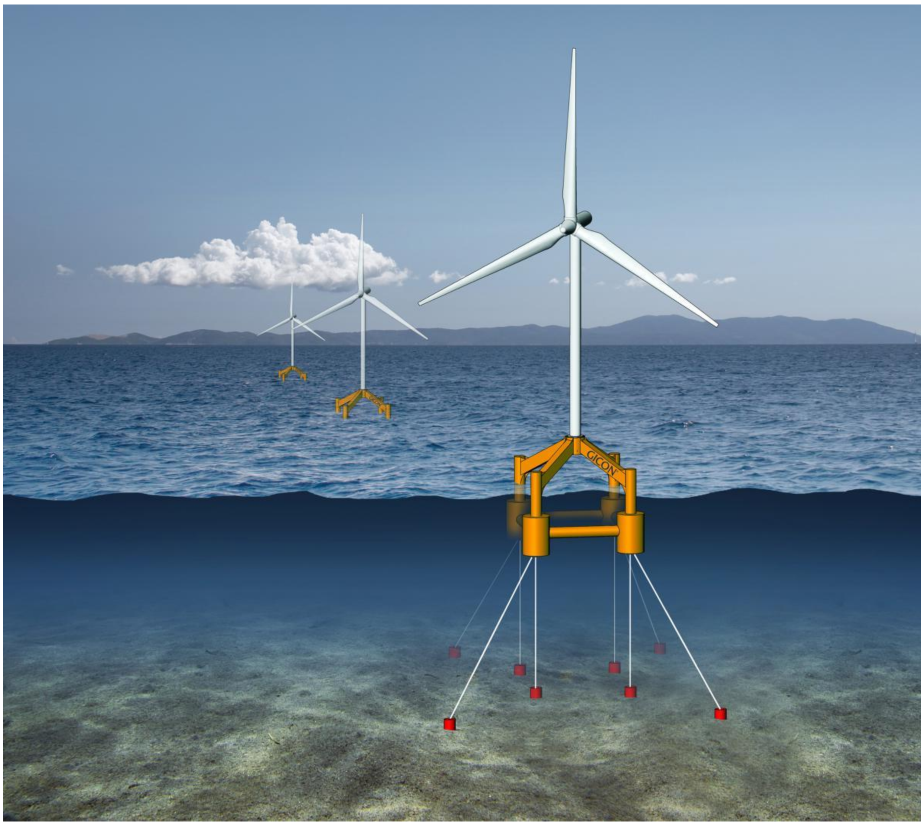

Figure 1.5. FOWTs are just anchored on the seafloor, making them easier to install.

The vision of large-scale FOWTs was first introduced by Professor William E. Heronemus back in 1972, but it was only after the commercial wind industry was well established that the topic was taken up again [5].

1.2.1 Advantages and disadvantages

In 2015 Carbon Trust, an independent company that carries out carbon reduction evaluations for organizations and governments, estimated that the energy produced by wind turbines in deep waters in the North Sea alone could meet the EU's electricity consumption four times over [6]. The table below reports some other staggering conclusions present in the same study.

Country/Region	Share of offshore wind resource in deep water locations (>60m depth)	Potential floating wind capacity
Europe	80%	4,000 GW
USA	60%	2,450 GW
Japan	80%	500 GW

Table 1.1. The potential wind resource exploitable with FOWTs is enormous.

These numbers give an idea of the immense potential of the FOWT concept.

Moreover, the exploitable sea surface wouldn't be difficult to reach: the first of the following two figures shows the sea depth around the coasts of Europe, while the second one the average wind speed 50 meters over the sea surface in the same area. The superposition of regions in the two pictures with shallow waters and strong winds is undoubtedly of great interest and confirms the vast potential for FOWTs.

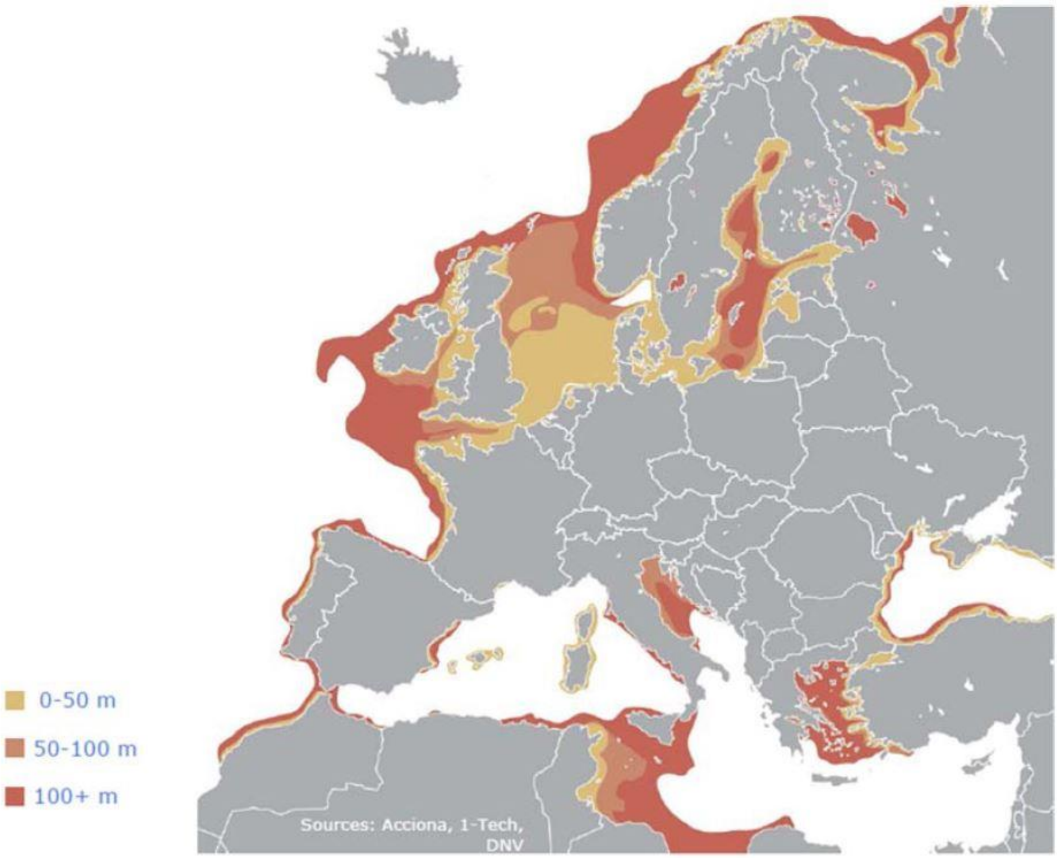

Figure 1.6. Most of Europe, particularly in the north, is surrounded by shallow waters.

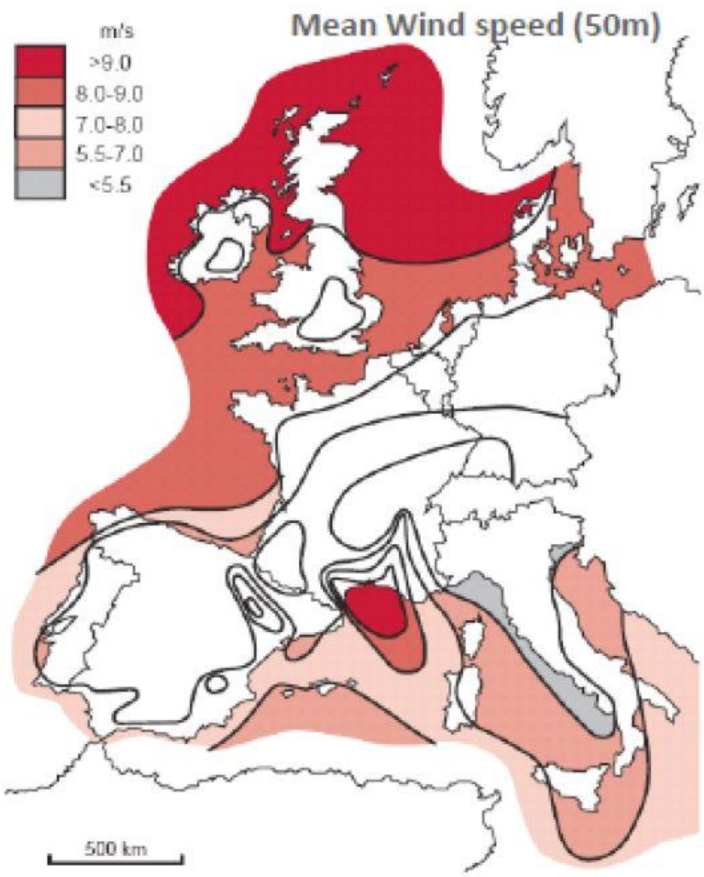

Figure 1.7. The farther away from the coast, the stronger the winds at a 50 m altitude.

It's also worth noting how the increased exploitable sea surface is not FOWTs' only advantage. As previously stated, working far from the coastline and its morphological irregularities reduces the wind turbulence on the turbine, increasing the expected lifespan of the farms up to 30 years [4], with respect to the ca. 20 expected for the currently operating technology.

Additionally, floating platforms allow for simplified and more flexible deployment, as more operations required for their construction and installation can be carried out on land, and then the assembled structure can be easily towed in position without requiring the specialized vessels needed today. Their greater mobility also allows them to be easily swapped or moved to port in case some repairs are necessary. Furthermore, an increased installation depth usually means also an increased distance from the coast. Wind farms will be installed outside the coastal Zone of Visual Influence, being invisible from shore and thus eliminating any protest. The size of this area, also known as ZVI, can be easily calculated through a simple equation, reported by Sclavounos [4]

$$L = \sqrt{2HR} \tag{1.1}$$

Where L is the distance from shore for a turbine to be invisible, H is the maximum height of the turbine's blade tip, and R is Earth's radius. To give a quick example, L = 45 km in case of a 155-meter-high blade tip.

1.2.2 Floater types

The extensive research that is being carried out on FOWTs still hasn't figured out which is the best design for the floating platform to put beneath the turbine. Multiple designs have been proposed by various companies, each having their pros and cons. Without analyzing every model present on the market today, a sufficiently accurate overview can be performed describing the three main types of platforms that are more promising to this day.

- Spar-buoy types: it's the simplest design, characterized by a very long and thin cylinder-like platform, often more than 100 m long. Its center of mass is moved far below the center of buoyancy, which creates a strong restoring moment when the structure is out of its equilibrium point. Due to its simple design, it's easy to build and provides excellent stability, even though the notable draft causes difficulties during the assembly, transportation, and installation phases and requires depths of more than 100 meters. One of the most promising models of this type is the OC3 platform by Hywind.
- Semi-submersible Platform: this kind of platform uses the hydrostatic stiffness of substructures piercing the waterplane area in positions far from the center axis of the tower. In this way, the restoring stiffness needed for stability is provided. This design often requires a large and heavy structure to maintain proper balance, but the reduced draft allows for more flexible applications and an easier installation.
- Tension-Leg Platform: in this case, the mooring is actively involved in the stabilization of the structure. This design is inherently unstable because the center of gravity is situated above the center of buoyancy. Therefore, the mooring provides the righting moment by being connected to off-axis fairleads, and from there transfer the wind turbine loads into the anchors below. The shallow draft and tension stability allow for a smaller and lighter structure, while the stresses on the tendons and anchors system are higher than in the previous designs.

1.2.3 Mooring systems

As for the platform geometry and characteristics, extensive research is currently underway to find the best mooring and anchoring systems and materials for commercial applications. Extra-heavy-duty cables are required, as they need to fix the platforms in place while enduring mechanical loads from both waves and wind, and chemical corrosion from seawater [7].

The choice of the mooring method has such an impact on the overall architecture of the platform that FOWTs can be classified according to the system they use [5]. The most commonly used are the catenary moorings, the taut-leg moorings and vertical tension legs, which are considered a subset of the taut-leg moorings.

The first two systems are shown in the following figure.

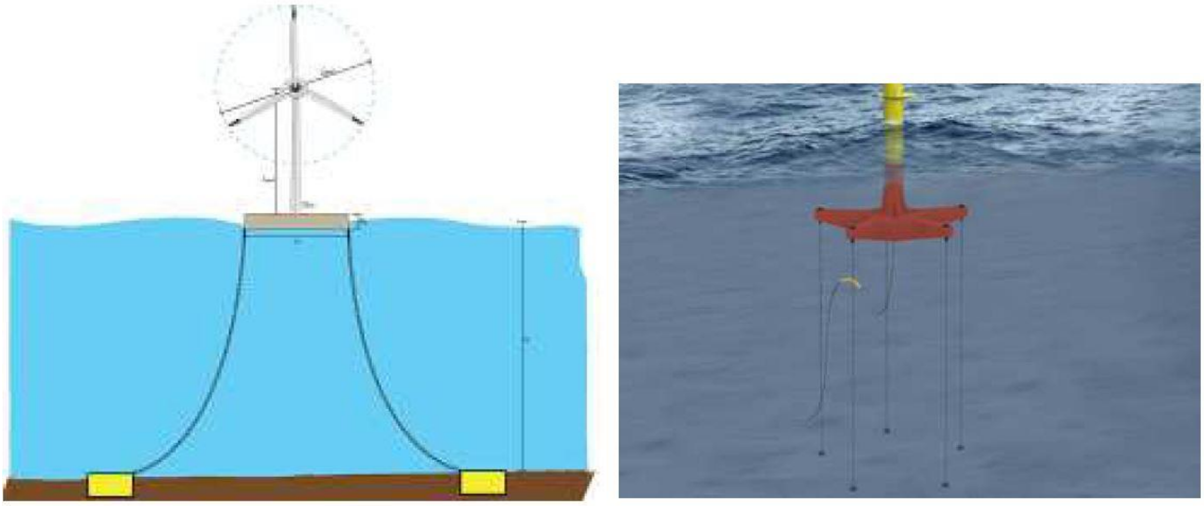

Figure 1.8. A graphical comparison of catenary moorings (left) and taut-leg moorings (right).

The pros and cons of each system are briefly reported. Some of the information is taken from [5].

- Catenary moorings: the most significant advantages of this kind of system are the relatively low cost of the anchors and the possibility to be deployed in shallow waters. On the other hand, the vertical tension of the anchor line is often insufficient to prevent overturning, because of the weight and the strong horizontal forces acting so far above the center of buoyancy. This distribution of weights means that additional ballast must be added below it, or buoyancy must be widely distributed. Catenary moored platforms present a significant portion of the structure above the waterline, which means a higher wave loading acting on it. Therefore, in general, this kind of platform subjects the turbine to a broader base motion in all directions, increasing the complexity of the system integration.
- Taut-leg moorings: the more the water depth increases, the more these systems become advantageous over the previous type. This is because their footprint (the surface of seafloor necessary for anchoring) is smaller, needing shorter mooring lines. If the taut legs are installed in a vertical orientation, the footprint becomes even smaller, but the high vertical forces consequently developed require more complex anchoring systems. Vertical moorings allow a larger portion of the structure to be submerged, minimizing wave action while maintaining the platform very stable.

In deciding which system to use, it’s often a trade-off between the added complexity introduced by platform dynamics and the associated turbine cost, and the added complexity and expenses for the anchoring system.

1.2.4 Anchoring systems

The main factor influencing the choice of a certain kind of anchoring system is the bottom soil, because its shear strength is the primary mechanism for resisting the forces applied. Also the soil weight is a major factor to consider. As expected, the deeper the anchor can be embedded, the higher the quantity of affected soil and, consequently, the greater the holding capacity.

The direction of the applied force also influences the holding capacity of an anchor. If the force is applied parallel to the bottom, as in the case of catenary moorings, there is no need for a deep embedment, and less precision is required in their placement. Thus, installation is less expensive, although platforms using catenary mooring experience more significant motions in every direction compared to other designs.

On the other hand, vertical load anchors depend on deep embedment to affect a large soil surface, increasing the cost of installation. They also need a more accurate placement.

Describing in detail all the types of mooring systems used goes beyond the scope of this thesis. It’s sufficient to say that the factors determining the choice of the anchor vary so widely that, in most cases, the technical solution is specifically designed for the bottom conditions of the site.

Beside the kind of installation required, other factors influencing the final cost of the mooring system are the material cost of the anchor and mooring lines. The challenge regarding the economic aspect of anchors is to find a relatively inexpensive system with a high vertical load capacity which, at the same time, is also easy to install.

1.2.5 Economic considerations

Before digging deep in an economic comparison between fixed-bottom and floating-platform wind turbines, it's essential to keep in mind that while cost data for the former technology are relatively robust and related to a fully commercialized sector, the available data for the latter is much more uncertain and referring prevalently to prototypes and pre-commercial installations. Like for every new technology, in the initial stages of conception and development, costs tend to quickly increase, with a successive decrease in the phases of optimization and industrialization.

This premise is essential, as the cost of early prototypes does not reflect the actual costs that can be expected once designs are optimized, new technologies are introduced, and serial fabrication methods are implemented; in other words, once all the benefits of scale effects and mass production kick in.

One of the most comprehensive economic evaluations of FOWT was carried out in 2014 by four researchers at the Norwegian University of Life Sciences [8] and was used to gather the data reported in this chapter. In their work, several promising prototypes of FOWTs are compared with the two most diffused solutions adopted for bottom-fixed turbines.

First, it’s interesting to compare the Capital Expenditure (CAPEX) for a typical fixed-bottom and floating offshore wind projects.

The figure below not only reports absolute monetary values, expressed in *\$/MW*, but it also breaks down how these costs are divided among the various aspects of the installation. The data referring to bottom-fixed designs are the last two bars to the right.

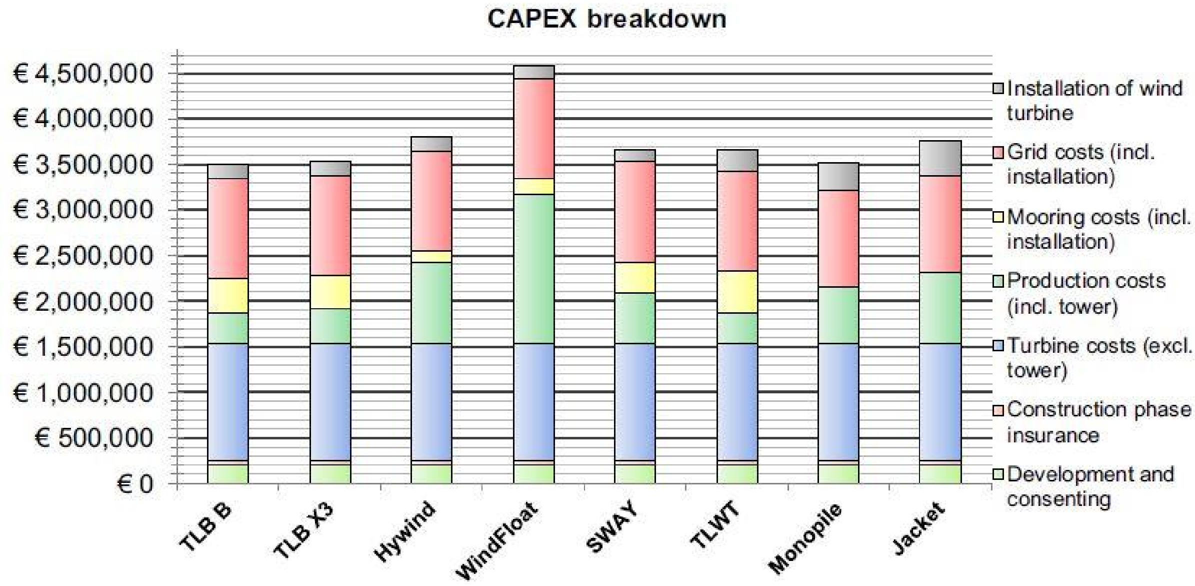

Figure 1.9. FOWTs CAPEX is almost competitive with that of fixed turbines.

As expected, the foundation and installation costs are lower for the FOWT, because the structure can be assembled onshore and then towed to the site even in rough sea conditions, which usually halt the works for traditional offshore projects. Obviously, mooring costs are absent in the case of bottom-fixed turbines. In both cases, most of the CAPEX flows into the turbine itself. The incidence is higher for floating projects because they require a more detailed match-making process to couple a turbine and its base as effectively as possible, while bottom-fixed platforms are said to be ‘turbine agnostic’ [6].

Summarizing, a higher CAPEX is expected for floating solutions, but what could be decisive for the success of FOWTs are the cost savings that could be achieved during the operation of the turbine, named Operational Expenditure (OPEX). There are important reductions expected in this sector, especially for major repairs like the gearbox substitution. This is because carrying out these tasks on fixed platforms requires jack-up or dynamic positioning vessels, which are very expensive. On the other hand, most FOWTs are designed so that they can be disconnected from the moorings and towed to the nearest port, where easier maintenance can be performed.

Combining the CAPEX and OPEX, together with the expected energy output of the project, one can calculate the cost competitiveness of FOTWs expressed by the Levelized Cost of Energy (LCOE, in *\$/MWh*), which at the end of the day is the parameter determining the success or failure of a specific technology. That’s because it shows if a technology can produce energy at a competitive price for the market.

Early studies have shown that floating wind turbines will be able to achieve results comparable to those of bottom-fixed technology real soon, mostly because of higher yields (the ratio between the effective output and the nominal one) thanks to faster, more constant winds on high-sea.

The figure below seems to confirm this prediction; again, bottom-fixed designs are on the far right.

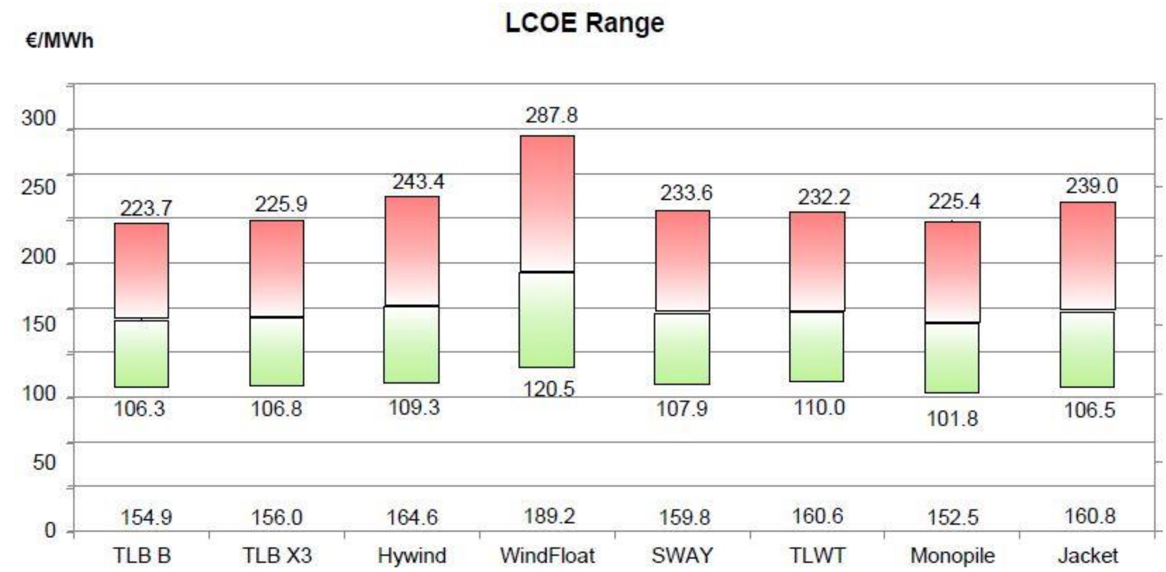

Figure 1.10. LCOE for the reference wind farm for each concept with values for best- and worst-case scenarios.

Taking the average values of this plot and comparing them with the ones available for other energy sources gives additional reasons to be optimistic about the future of the technology. As the figure below shows, LCOE for FOWTs is comparable to the ones calculated both for conventional (like nuclear power) and unconventional (like fuel cells) energy sources, as Lazard categorizes them [9].

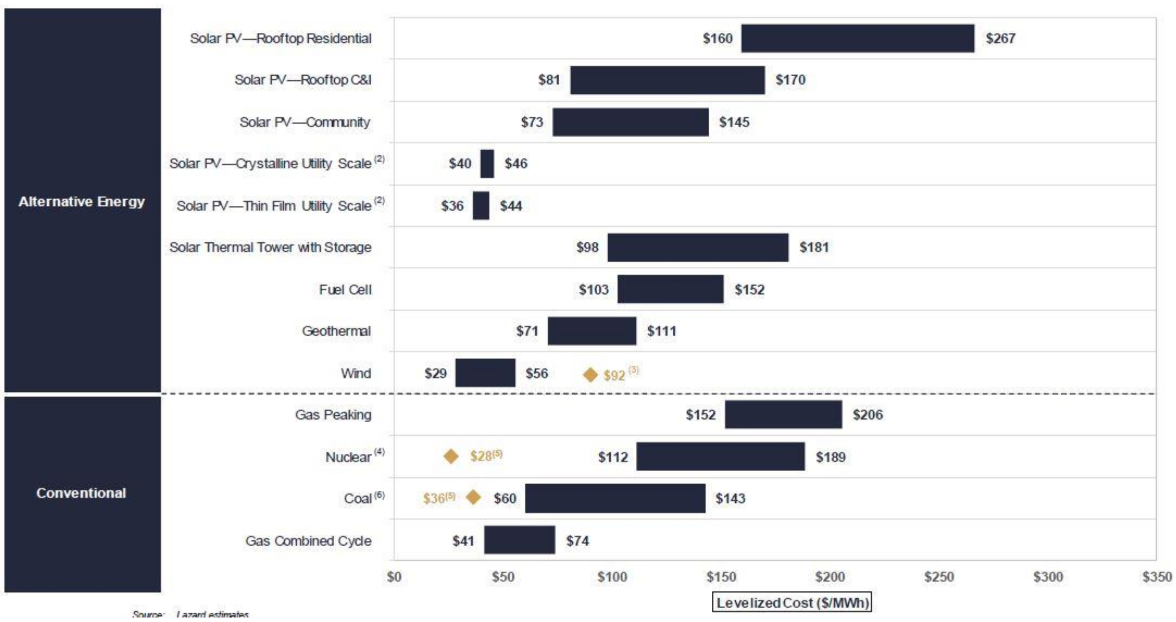

Figure 1.11. Comparing with data of fig. 1.10, soon FOWTs will be competitive on the market.

1.3 THE NEED FOR HYDRODYNAMIC MODELS

Despite their high potential for future development, FOWTs force engineers to face a whole new set of challenges related to the behavior of the floating platform and the overlying turbine, once they are free to move following the motion of the waves and subject to the force of the wind. Having a rotor that oscillates has a detrimental effect on the performances of the turbine since its plane is often not perpendicular to the incoming wind.

Therefore, the hydrodynamic behavior of the platform in the supposed operative conditions requires to be thoroughly analyzed. Since these evaluations cannot be carried out on real-scale models due mainly to high costs, there is the need to use hydrodynamic analysis models and softwares to calculate the forces and moments acting on the platform.

These softwares evaluate how the incoming waves influence the motion of the platform and the intensity of the forces and moments acting on its surface. Most of these softwares use the Boundary Element Method (BEM), or Panel Method, which is a numerical technique that uses systems of partial differential equations formulated into the integral boundary form. BEM codes employ the Green's functions to transform a flow problem into a problem of source distribution on the body surface [10]. When used in the hydrodynamic context, BEM solves separately the scattered and radiated velocity potentials that arise from the interaction of a harmonic linear wavefield with a body located within that field [11].

BEM is the most common method used in hydrodynamic context because, while limited by the linear nature of potential flow theory, the speed of the numerical simulation is much higher than other simulation methods like Computation Fluid Dynamics. This makes BEM a common choice for early-stage device development [10].

Several commercial softwares have been developed to implement BEM in the field of hydrodynamic diffraction simulations. Such systems include the well-established commercial software WAMIT or Ansys AQWA, and some more recently released, open-source solvers like NEMOH.

A new hydrodynamic analysis model has been developed at the Hermann-Föttinger-Institut at the Technische Universität Berlin as part of the QBlade software, which is an open-source wind turbine calculation and modeling software, an easy-to-use and flexible tool that allows the user to simulate the performances of a customized wind turbine accurately. Adding BEMUse's library will allow the precise analysis of a FOWT, as it will let the user evaluate the influence that the motion caused by the sea waves has on the overall performance of the installation.

However, since BEMUse is a recently developed model, its results must be compared to the ones of other older and widely used hydrodynamic analysis softwares, to make sure it works correctly. Only then BEMUse can be included in QBlade. This thesis has the aim to carry out the comparison between BEMUse and both WAMIT and AQWA softwares to check if the results for the most important hydrodynamic coefficients coincide. If they do, BEMUse can be considered validated and, therefore, ready to be implemented in QBlade.

Before proceeding with the comparison, though, an overview of BEMUse's theoretical background is provided in the next chapter.

2. THEORY

This chapter will give a brief overview of BEMUse's theoretical basis, which is, in fact, the same as WAMIT's. WAMIT Theory Manual [12] thoroughly illustrates the theory behind the hydrodynamic model; thus, the majority of what's written in this chapter was taken from that source.

BEMUse is designed to solve the boundary value problem for the interaction of water-waves both in finite- and infinite- water depth, given a prescribed geometry of the body. The model uses quadrilateral panels to carry out this task.

Viscous effects of the fluid are neglected, and therefore the flow field is considered potential without circulation.

Another fundamental assumption is that the body stays at its mean position, and in case it's not fixed, the oscillatory amplitude of the body motion is of the same order as the wave amplitude.

The boundary value problem is reorganized into integral equations using the wave source potential as a Green function. This integral equation is then solved via the panel method for the unknown velocity potential or the source strength on the body surface. The latter is needed to then calculate the fluid velocity on the body surface.

2.1 DESCRIPTION OF THE PROBLEM

As stated before, the flow is assumed to be potential, free of separation or lifting effects and it's governed by the velocity potential ϕ (x, t) which satisfies Laplace's equation in the fluid domain:

$$\nabla^2 \phi = 0 \tag{2.1}$$

Where t is the time, and $x = (x, y, z)$ denotes the Cartesian coordinates of a point in space. In all cases, the undisturbed free surface is the $z = 0$ plane, and the fluid domain is in $z < 0$.

The gradient of the velocity potential gives the fluid's velocity

$$V(x,t) = \nabla\phi = \frac{\partial\phi}{\partial x} i + \frac{\partial\phi}{\partial y} j + \frac{\partial\phi}{\partial z} \tag{2.2}$$

And the pressure is then calculated with Bernoulli's equation

$$p(X,t) = -\rho\left(\frac{\partial\phi}{\partial t} + \frac{1}{2}\nabla\phi\cdot\nabla\phi + gz\right) \tag{2.3}$$

Where ρ is the fluid density, and g is the gravitational acceleration.

The velocity potential satisfies the nonlinear free-surface condition:

$$\frac{\partial^2\phi}{\partial t^2} + g\frac{\partial\phi}{\partial z} + 2\nabla\phi\cdot\nabla\frac{\partial\phi}{\partial t} + \frac{1}{2}\nabla\phi\cdot\nabla(\nabla\phi\cdot\nabla\phi) = 0 \tag{2.4}$$

Applied on the exact free surface

$$\zeta(x,y) = -\frac{1}{g}\left(\frac{\partial\phi}{\partial t} + \frac{1}{2}\nabla\phi\cdot\nabla\phi\right)_{z=\zeta} \tag{2.5}$$

Assuming a perturbation solution in terms of a small wave slope of the incident waves, the velocity potential can be expanded as:

$$\phi(x,t) = \phi^{(1)}(x,t) + \phi^{(2)}(x,t) + \cdots \tag{2.6}$$

And the same happens to the motion amplitude of the body if it is not fixed:

$$\xi = \xi^{(1)} + \xi^{(2)} + \cdots \tag{2.7}$$

Given a wave spectrum, it is usually assumed that it is expressed as a linear superposition of first-order incident waves of different frequencies. Thus, the local first-order potential for the wave-body interaction can be represented by a sum of components having circular frequency $\omega_j > 0$

$$\phi^{(1)}(x,t) = Re\sum_j \phi_j(x)e^{i\omega_j t} \tag{2.8}$$

Where $\phi_j(x)$ is the complex velocity potential, which is independent of time; the real part of the time-harmonic solution is physically relevant.

In Eq. (2.8) $\phi_j(x)$ indicates the first-order solution in the presence of the incident wave with frequency ω_j and wave heading β_j, while the directional spreading of the incident waves is not shown explicitly.

2.2 First order problem

In this chapter, the first-order boundary value problem and its solution procedure are illustrated.

From now on, the subscript j indicating the frequency component will be omitted, as only one particular value of ω is considered.

The velocity potential for the first-order incident wave is defined by

$$\phi_I = \frac{igA}{\omega}Z(\kappa z)e^{-i\kappa(x\cos\beta + y\sin\beta)} \tag{2.9}$$

It represents a plane-progressive wave of circular frequency ω and wave heading angle β (calculated starting from the positive x-axis). A is the complex wave amplitude.

The function Z identifies the depth-dependence of the flow and has different forms in the case of infinite or finite water depth. In the former case, it's given by

$$Z(\kappa z) = e^{\kappa z} \tag{2.10}$$

And $\kappa = \frac{\omega^2}{g}$. In the latter, instead

$$Z(\kappa z) = \frac{\cosh(\kappa(z+h))}{\cosh(\kappa z)} \tag{2.11}$$

And this time κ is the real root of the dispersion relation

$$\kappa \tanh \kappa h = \frac{\omega^2}{g} \tag{2.12}$$

The scattering velocity potential ϕ_S denotes the disturbance to the incident wave due to the presence of the body in its fixed position. The linearity of the problem allows it to be distinguished from the interference due to the motion of the body, which is represented by the radiation potential ϕ_R. The total velocity potential is given by

$$\phi = \phi_I + \phi_S + \phi_R = \phi_D + \phi_R \tag{2.13}$$

Where the diffraction potential ϕ_D is defined as the sum of ϕ_I and ϕ_S.

The radiation potential is a linear combination of the components corresponding to the modes of motion such that

$$\phi_R = i\omega \sum_{k=1}^{6} \xi_k \phi_k \tag{2.14}$$

Where ξ_k is the complex amplitude of the oscillatory motion in mode k of the six degrees of freedom, and ϕ_k the corresponding unit-amplitude radiation potential.

These modes are referred to as surge, sway, heave, roll, pitch and yaw in the increasing order of j.

2.3 Boundary value problem

The first-order velocity potential ϕ, together with each of its components, satisfies the Laplace equation in the fluid domain

$$\nabla^2 \phi = 0 \tag{2.15}$$

The linear free-surface condition

$$\phi_z - \nu\phi = 0 \tag{2.16}$$

On $z = 0$, and a condition on the sea bottom

$$\nabla \phi \to 0 \tag{2.17a}$$

As $z \to -\infty$, or

$$\phi_z = 0 \tag{2.17b}$$

On $z \to -h$, for infinite- and finite-water depth, respectively.

Moreover, the scattering and the radiation potentials are subject to a radiation condition stating that the wave energy associated with the disturbance due to the body is carried away from the body in all directions in the far field.

Finally, the conditions on the body surface complete the description of the boundary value problem.

They take the form

$$\frac{\partial \phi_k}{\partial n} = n_k \tag{2.18}$$

And

$$\frac{\partial \phi_S}{\partial n} = -\frac{\partial \phi_I}{\partial n} \tag{2.19}$$

Where (n_1, n_2, n_3) = n and (n_4, n_5, n_6) = x **x** n. The vector of unitary value n is normal to the body boundary, and it's assumed it points out of the fluid domain. X is the position of a point on the body boundary. From (2.13), it follows that

$$\frac{\partial \phi_D}{\partial n} = 0 \tag{2.20}$$

2.4 INTEGRAL EQUATIONS

The boundary value problem is then solved by the integral equation method. Therefore, the velocity potential ϕ_k on the body boundary is obtained from the equation

$$2\pi\phi_k(x) + \iint_{S_B} d\xi \phi_k(\xi) \frac{\partial G(\xi; x)}{\partial n_\xi} = \iint_{S_B} d\xi n_k G(\xi; x) \tag{2.21}$$

Where S_B denotes the body boundary.

The corresponding equation for the diffraction velocity potential ϕ_D is

$$2\pi\phi_D(x) + \iint_{S_B} d\xi \phi_D(\xi) \frac{\partial G(\xi; x)}{\partial n_\xi} = 4\pi\phi_I(x) \tag{2.22}$$

Instead, the scattering potential can be obtained from

$$2\pi\phi_S(x) + \iint_{S_B} d\xi \phi_S(\xi) \frac{\partial G(\xi; x)}{\partial n_\xi} = \iint_{S_B} d\xi \left(-\frac{\partial \phi_I}{\partial n}\right) G(\xi; x) \tag{2.23}$$

And the diffraction potential follows from (2.13). From a computational point of view, (2.22) is more efficient than (2.23) due to the simpler form of the right-hand side.

The velocity may be computed from the particular derivatives of Green's integral equations, (2.21) to (2.23). However, when these equations are solved using a low-order panel method like in BEMUse, they cannot predict the velocity accurately on or close to the body boundary.

Therefore, the fluid velocity is computed based on source formulation. The integral equation for the source strength σ_k corresponding to the radial potential ϕ_k takes the form

$$2\pi\sigma_k(x) + \iint_{S_B} d\xi \sigma_k(\xi) \frac{\partial G(\xi; x)}{\partial n_x} = n_k \tag{2.24}$$

And that of σ_S corresponding to the scattering potential ϕ_S

$$2\pi\sigma_S(x) + \iint_{S_B} d\xi \sigma_k(\xi) \frac{\partial G(\xi; x)}{\partial n_x} = -\frac{\partial \phi_I}{\partial n} \tag{2.25}$$

The velocity of the fluid on the body boundary or in the fluid domain due to ϕ_k or ϕ_S is then obtained from

$$\nabla\phi(x) = \nabla \iint_{S_B} d\xi\sigma(\xi)G(\xi;x) \tag{2.26}$$

The fluid velocity due to the incident wave is evaluated directly from (2.9).

Integral equations (2.21) to (2.25) are solved by the panel method, where a high number of quadrilateral panels represent the wetted body surface. The unknowns are assumed to be constant on each panel, and the integral equation is enforced at the centroid of each of them.

As an example, the discrete form of the equation (2.23) takes the form

$$2\pi\phi_S(x_k) + \sum_{n=1}^{NEQN} \phi_S(x_n) \int_{S_n} d\xi \frac{\partial G(\xi;x_k)}{\partial n_\xi} = \sum_{n=1}^{NEQN} -\frac{\partial \phi_I(x_n)}{\partial n} \int_{S_n} d\xi G(\xi;x_k) \tag{2.27}$$

Where NEQN is the total number of panels (unknowns), and x_k are the coordinates of the centroid of the *k-th* panel.

2.5 GREEN'S THEOREM AND DISTRIBUTION OF SINGULARITIES

Given the basilar importance of the Green function in the solution of hydrodynamic diffraction and radiation problems, a more in-depth overview of the topic is necessary. For this scope, Newman's book Marine Hydrodynamics [13] provides sufficient information.

Certain immersed bodies could be represented by a point dipole. Given the effect of these singularities on the surrounding fluid, it seems plausible that a larger number of them could be used to represent more complicated body shapes. For the cases analyzed here, a distribution on the body surface only is usually enough.

Let's consider two solutions of Laplace's equation in a volume V of fluid bounded by a closed surface S. Denoting these two potentials by φ and ϕ and applying the divergence theorem we get

$$\iint\limits_S \left[\phi\frac{\partial\varphi}{\partial n} - \varphi\frac{\partial\phi}{\partial n}\right] dS = \iiint\limits_V \nabla\cdot(\phi\nabla\varphi - \varphi\nabla\phi)dV =$$

$$= \iiint\limits_V (\phi\nabla^2\varphi + \nabla\phi\cdot\nabla\varphi - \varphi\nabla^2\phi - \nabla\varphi\cdot\nabla\phi)dV = 0 \tag{2.28}$$

This significant result is a form of Green's theorem that will be utilized later. Now let's consider the consequence of replacing ϕ by the potential of a source.

For this analysis, the source strength is $m = 1$. Of more significance is the position of this unit source, which must be carefully specified. The source point is therefore defined as $\xi = (\xi, \eta, \zeta)$ as the position of the source in the coordinates $x = (x, y, z)$. For a unit source, the potential at the field point x is given by

$$\phi = \frac{1}{4\pi r} = \left(\frac{1}{4\pi}\right)[(x-\xi)^2 + (y-\eta)^2 + (z-\zeta)^2]^{-\frac{1}{2}} \tag{2.29}$$

As easily predictable, the value of (2.29) is unchanged if the source point and the field point are interchanged. At the same time, (2.29) is a solution of Laplace's equation with respect to ξ as well as x. Thus, in utilizing this source potential in Green's theorem (2.28), it's possible to integrate with respect to either coordinate system.

In the subsequent derivation, the integration of (2.28) is performed for the coordinates of the source point ξ. This requires the potential ϕ and the normal derivative $\partial\phi/\partial n$ to be defined with respect to (ξ, η, ζ) by a simple change of the dummy variable of integration. Physically, what's being performed is the integration over a continuous distribution of sources and normal dipoles that are located on the surface S, with a fixed value of the field point x.

Substituting (2.29) in (2.28) requires caution, for the source potential does not satisfy the Laplace equation at the singular point $r = 0$, and thus (2.28) is not valid when the source point is situated within V. This difficulty can be avoided by surrounding the source point by a small sphere of radius $r = \varepsilon$ with surface S_ε as shown in the figure below.

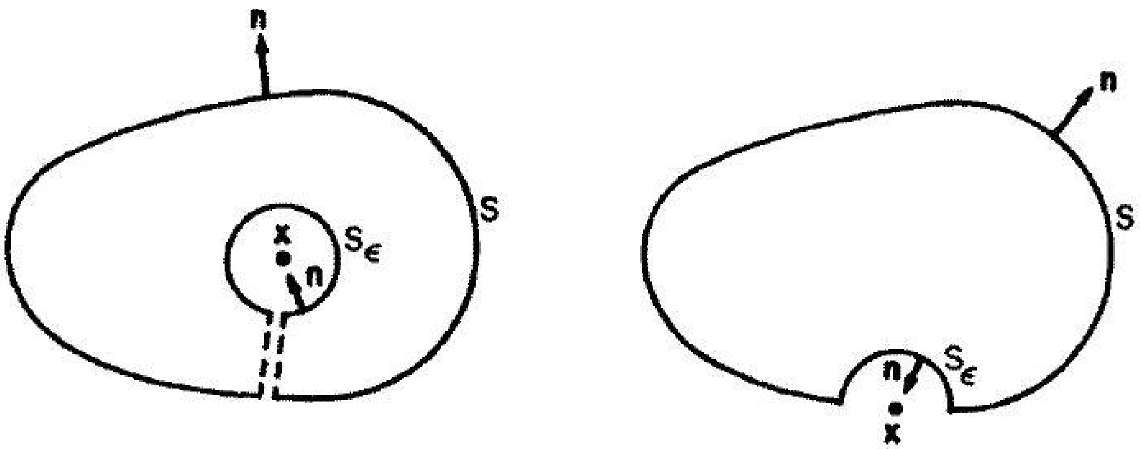

Figure 2.1. In (a), the field point is interior to S; in (b), it's on the boundary surface and S_ε is a hemisphere.

Then $S + S_\varepsilon$ is a closed surface surrounding the volume of the fluid interior to S, but exterior to S_ε; within the volume, (2.29) is regular. Thus, (2.28) can be replaced

$$\frac{1}{4\pi}\iint\limits_{S+S_\varepsilon}\left[\phi\frac{\partial}{\partial n}\frac{1}{r}-\frac{1}{r}\frac{\partial\phi}{\partial n}\right]dS = 0 \tag{2.30}$$

Or

$$\frac{1}{4\pi}\iint\limits_{S}\left[\phi\frac{\partial}{\partial n}\frac{1}{r}-\frac{1}{r}\frac{\partial\phi}{\partial n}\right]dS = -\frac{1}{4\pi}\iint\limits_{S_\varepsilon}\left[\phi\frac{\partial}{\partial n}\frac{1}{r}-\frac{1}{r}\frac{\partial\phi}{\partial n}\right]dS \tag{2.31}$$

In the limit $r \rightarrow \varepsilon$, the contribution from the integral over S_ε in (2.31) can be evaluated under the assumption that the velocity potential and its normal derivative on S_ε are both regular. The area of S_ε is $4\pi r^2$, while the normal derivative of $1/r$ is $-\partial/\partial r(1/r) = 1/r^2$. Thus, the first term in the integrand on the right-hand side of (2.31) is singular in proportion to $1/r^2$, and when it is multiplied by the area $4\pi r^2$, a finite limit will result as $\varepsilon \rightarrow 0$, whereas the weaker singularity of the second term will give no contribution.

For sufficiently small ε, the potential ϕ may be assumed constant and taken outside of the integral sign, so that the final limiting value of the right-hand side of (2.31) becomes

$$-\frac{1}{4\pi}\phi(x,y,z)\iint_{S_\varepsilon}\frac{\partial}{\partial n}\frac{1}{r}\,dS=-\phi(x,y,z) \tag{2.32}$$

Thus, if (x, y, z) is inside S,

$$\phi(x,y,z)=-\frac{1}{4\pi}\iint_{S}\left[\phi\frac{\partial}{\partial n}\frac{1}{r}-\frac{1}{r}\frac{\partial\phi}{\partial n}\right]dS \tag{2.33}$$

Equation (2.33) can be regarded as a representation of the velocity potential in terms of a standard dipole distribution of moment ϕ and a source distribution of strength $-\partial\phi/\partial n$ distributed over the boundary surface S. Thus, in general, the flow can be represented by a suitable distribution of dipoles and sources on S.

If the point (x, y, z) is located on the surface S, the surface S_ε is chosen to be a small hemisphere that indents the original surface S inside the source point, as in the figure above. The contribution form of this hemisphere is just half that given by (2.32), so (2.33) is replaced by

$$\phi(x,y,z)=-\frac{1}{2\pi}\iint_{S}\left[\phi\frac{\partial}{\partial n}\frac{1}{r}-\frac{1}{r}\frac{\partial\phi}{\partial n}\right]dS \tag{2.34}$$

Here, the surface integral must be defined to exclude the immediate vicinity of the singular point, i.e. the locally-plane infinitesimal surface bounded by the intersection of S and the hemisphere S_ε. This situation is analogous to a principal value integral, except that in (2.34) the precise shape of the excluded infinitesimal area is not essential.

Equation (2.34) is frequently used for constructing the velocity potential due to the motion of a ship hull or other moving bodies. Generally, the normal derivative $\partial\phi/\partial n$ is known on the body, so that (2.34) is an integral equation for the determination of the unknown potential, and it may be solved by numerical techniques like the one used by BEMUse.

In many situations, however, the body may move in a fluid bounded by other boundaries such as the free surface, the fluid bottom, or possibly lateral boundaries such as canal walls. In each of these cases, additional boundary conditions are imposed, and there is often a computational advantage in solving (2.34) if the source potential is modified to satisfy the same boundary conditions as ϕ. In this context the Green function

$$G(x,y,z;\ \xi,\eta,\zeta)=\frac{1}{r}+H(x,y,z;\ \xi,\eta,\zeta) \tag{2.35}$$

can be substituted for the source potential in (2.33-2.34) since (2.28) is valid for the contribution from the regular and generic function H, which satisfies the Laplace equation. Thus, with the Green function defined by (2.35), we can state that

$$\iint_{S}\left(\phi\frac{\partial G}{\partial n}-G\frac{\partial\phi}{\partial n}\right)dS=\begin{Bmatrix}0\\-2\pi\phi(x,y,z)\\-4\pi\phi(x,y,z)\end{Bmatrix} \tag{2.36}$$

For (x, y, z) outside, on, or inside the closed surface S. The regular function H can be chosen to suit any additional boundary conditions that may be imposed. If H can be found with the property that

$$\frac{\partial G}{\partial n} = 0 \tag{2.37}$$

on the boundary surfaces of the fluid, the unknown term in the integrand of (2.36) vanishes. With this choice of the Green function, (2.36) provides an explicit solution for the potential in terms of the prescribed normal velocity on the boundaries. In the next chapter, a more detailed analysis of the Green function used by BEMUse is given.

2.5.1 The Green function

The Green function $G\ (x; \xi)$, also known as the wave source potential, is the velocity potential at the point x due to a point source of strength -4π located at the point ξ. It satisfies the free-surface and radiation conditions, and in infinite water depth it is defined by Wehausen and Laitone [14]

$$G(x;\xi) = \frac{1}{r} + \frac{1}{r'} + \frac{2\nu}{\pi}\int_0^{\infty} dk\, \frac{e^{k(z+\zeta)}}{k-\nu} J_0(kR) \tag{2.38}$$

$$r^2 = (x-\xi)^2 + (y-\eta)^2 + (z-\zeta)^2 \tag{2.39}$$

$$r'^2 = (x-\xi)^2 + (y-\eta)^2 + (z+\zeta)^2 \tag{2.40}$$

Where $J_0(x)$ is the Bessel function of zero order, while r and r' are the geometrical distances between the source and dipole (the former), and between the reflection of the source above sea level and the dipole (the latter). In finite depth, it's defined by

$$G(x;\xi) = \frac{1}{r} + \frac{1}{r''} + 2\int_0^{\infty} dk\, \frac{(k+\nu)\ \cosh k(z+h)\cosh k(\zeta+h)}{k\sinh kh - \nu\cosh kh} e^{-kh} J_0(kR) \tag{2.41}$$

$$(r'')^2 = (x-\xi)^2 + (y-\eta)^2 + (z+\zeta+2h)^2 \tag{2.42}$$

In both expressions (2.37) and (2.40), the Fourier k-integration is indented above the pole on the real axis to enforce the radiation condition.

In the equation (2.27), the influence due to the continuous distribution of the Rankine part of the wave source potential on a quadrilateral panel is evaluated with the algorithms described by Newman (1985)[15]. The remaining wave part of the Green function is assessed based on the algorithms contained in Newman (1992) [16]. The integration of the last part over a panel is performed using the single-point Gaussian quadrature. When the field and source points are close together, and in the vicinity of the free surface, G takes a form

$$G(x;\xi) = \frac{1}{r} + \frac{1}{r'} - 2\nu e^{\nu(z+\zeta)}\big(\log(r' + |z+\zeta|) + (\gamma - log2) + r' + O(r' log\, r')\big) \tag{2.43}$$

Where γ is the Euler constant. The logarithmic singularity in (2.43) cannot be evaluated accurately using Gauss's quadrature in this situation. The algorithm to assess the influence of the logarithmic singularity distributed over a panel can be found in Newman and Sclavounos (1988) [17]. When the panel is on the free surface, special attention is required for the evaluation of Green function, as is discussed in Newman (1993) [18] and Zhu (1994) [19].

2.6 First order force

The expression for the first-order force is derived from direct integration of the fluid pressure over a body boundary. By making use of Green's theorem, part of the forces can be obtained without solving the scattering potential.

2.7 Hydro-static and -dynamic force and moment

2.7.1 Coordinate system

Three coordinate systems are considered: $X = (X, Y, Z)$ is a global coordinate system with $Z = 0$ being the undisturbed free surface, and the positive Z-axis points upward; $x = (x, y, z)$ is a body-fixed coordinate system, z also is positive upwards when the body is at rest; the third coordinate system is fixed in space and coincides with "x at rest". It is denoted by $x' = (x', y', z')$. It's important to note that X and x' are inertial reference frames, while x is not. The origin of x' may be displaced from the free-surface and Z_0 denotes the Z-coordinate of the origin of x'.

2.7.2 Coordinate transform

The position vectors in the x'- and x- coordinate systems are related to each other by a linear transformation

$$x' = \xi + T^t \tag{2.44}$$

And the normal vector by

$$n' = T^t \tag{2.45}$$

T_t is the transpose of $T = T_3T_2T_1$ and T_1, T_2 and T_3 take forms

$$\begin{aligned} T_1 &= \begin{pmatrix} 1 & 0 & 0 \\ 0 & \cos\alpha_1 & \sin\alpha_1 \\ 0 & -\sin\alpha_1 & \cos\alpha_1 \end{pmatrix} \\ T_2 &= \begin{pmatrix} \cos\alpha_2 & 0 & -\sin\alpha_2 \\ 0 & 1 & 0 \\ \sin\alpha_2 & 0 & \cos\alpha_2 \end{pmatrix} \\ T_2 &= \begin{pmatrix} \cos\alpha_3 & \sin\alpha_3 & 0 \\ -\sin\alpha_3 & \cos\alpha_3 & 0 \\ 0 & 0 & 1 \end{pmatrix} \end{aligned} \tag{2.46}$$

$\xi = (\xi_1, \xi_2, \xi_3)$ and $\alpha = (\alpha_1, \alpha_2, \alpha_3)$ are, respectively, the translational and rotational displacements of the x-coordinate system with respect to x'. They also represent the motion amplitudes of the body for surge-sway-heave and roll-pitch-yaw.

2.7.3 Pressure integration

All BEMUse's derivations (pressure, velocity potential, and body motion amplitudes) are a function of time, even though the time *t* does not appear explicitly.

The pressure at *x'* is given by Bernoulli's equation

$$P(x') = -\rho\left[\phi_t(x') + \frac{1}{2}\nabla\phi(x')\cdot\nabla\phi(x') + g(z' + Z_0)\right] \tag{2.47}$$

The hydrostatic and hydrodynamic force and moment are obtained from the integration of the pressure over the instantaneous wetted surface

$$F = \iint_{S'_B} P(x')n'dS \tag{2.48}$$

And

$$M = \iint_{S'_B} P(x')(x' \times n')dS \tag{2.49}$$

Where S_B' denotes the instantaneous wetted body boundary.

The pressure on the exact body surface ($x' \in S_B'$) may be approximated by Taylor expansion with respect to the mean body surface ($x \in S_B'$)

$$P(x') = P(x) + [\xi + (T^t - I)x]\cdot\nabla P(x) + \cdots \tag{2.50}$$

Substituting (2.50) into (2.44-2.45) we have

$$x' = x + \xi^{(1)} + \alpha^{(1)} \times x + Hx + \xi^{(2)} + \alpha^{(2)} \times x + O(A^3) \tag{2.51}$$

$$n' = n + \alpha^{(1)} \times n + Hn + \alpha^{(2)} \times n + O(A^3) \tag{2.52}$$

The cross product of (2.51) and (2.52) then takes a form

$$\begin{aligned} x' \times n' = x \times n + \xi^{(1)} \times n + \alpha^{(1)} \times (x \times n) + \xi^{(1)} \times \left(\alpha^{(1)} \times n\right) + \\ + H(x \times n) + \xi^{(2)} \times n + \alpha^{(2)} \times (x \times n) + O(A^3) \end{aligned} \tag{2.53}$$

From (2.47), (2.50) and (2.53), the pressure is expressed by the values on the mean body position

$$\begin{aligned} P(x') = -\rho\{g(z + Z_0) + \left[\phi_t^{(1)}(x) + g\left(\xi_3^{(1)} + \alpha_1^{(1)}y - \alpha_2^{(1)}x\right)\right] + \\ + \left[\frac{1}{2}\nabla\phi^{(1)}(x)\cdot\nabla\phi^{(1)}(x) + \left(\xi^{(1)} + \alpha^{(1)} \times x\right)\cdot\phi_t^{(1)}(x) + gHx\cdot\nabla z\right] + \\ + \left[\phi_t^{(2)}(x) + g\left(\xi_3^{(2)} + \alpha_1^{(2)}y - \alpha_2^{(2)}x\right)\right]\} + O(A^3) \end{aligned} \tag{2.54}$$

H here is the second-order component of T', and it takes a form

$$H = \begin{pmatrix} -\frac{1}{2}\left(\left(\alpha_2^{(1)}\right)^2 + \left(\alpha_3^{(1)}\right)^2\right) & 0 & 0 \\ \alpha_1^{(1)}\alpha_2^{(1)} & -\frac{1}{2}\left(\left(\alpha_1^{(1)}\right)^2 + \left(\alpha_3^{(1)}\right)^2\right) & 0 \\ \alpha_1^{(1)}\alpha_3^{(1)} & \alpha_2^{(1)}\alpha_3^{(1)} & -\frac{1}{2}\left(\left(\alpha_1^{(1)}\right)^2 + \left(\alpha_2^{(1)}\right)^2\right) \end{pmatrix} \quad (2.55)$$

Substituting the expansions (2.50-2.54) into (2.48-2.49), we have the series expansion of the integrals (2.48-2.49).

2.7.4 Hydrostatic force and moment of O (1)

These are the buoyancy forces and moments when the body is at rest and are expressed by

$$F = -\rho g \iint_{S_B} (z + Z_0) n dS \quad (2.56a)$$

$$M = -\rho g \iint_{S_B} (z + Z_0)(x \times n) dS = -\rho g \iint_{S_B} [(z + Z_0)x] \times n dS \quad (2.56b)$$

The following relations are invoked frequently

$$-\iint_S \psi n dS = \iiint_V \nabla \psi dV$$

$$-\iint_S n \times \psi dS = \iiint_V \nabla \times \psi dV \quad (2.57)$$

$$\nabla \times (z + Z_0)x = k \times x$$

Here S is a closed surface consisting of S_B and the waterplane area A_{wp}. V denotes the volume of the body.

Using the relations (2.57), the force and moment are expressed in familiar forms

$$F = \rho g V k \quad (2.58a)$$

$$M = \rho g V (y_b i - x_b j) \quad (2.58b)$$

Where x_b and y_b are the coordinates of the center of buoyancy.

In (2.58a-2.58b), i, j, and k are the unit vectors in x' coordinate system.

2.8 LINEAR FORCE AND MOMENT

The linear force and moment are found from

$$F = -\rho \iint_{S_B} n\phi_t^{(1)} dS - \rho g \iint_{S_B} \left(\alpha^{(1)} \times n\right)(z + Z_0) dS + \\ -\rho g \iint_{S_B} n\left(\xi_3^{(1)} + \alpha_1^{(1)} y - \alpha_2^{(1)} x\right) dS \tag{2.59a}$$

$$M = -\rho \iint_{S_B} (x \times n)\, \phi_t^{(1)} dS - \rho g \iint_{S_B} (x \times n)\left(\xi_3^{(1)} + \alpha_1^{(1)} y - \alpha_2^{(1)} x\right) dS + \\ -\rho g \iint_{S_B} \left(\xi^{(1)} \times n\right)(z + Z_0) dS - \rho g \iint_{S_B} \left[\alpha^{(1)} \times (x \times n)\right](z + Z_0) dS \tag{2.59b}$$

Where the first terms are the hydrodynamic force and moment, and the others are the hydrostatic ones. Following the decomposition (2.13), we consider component potentials such that $\phi^{(1)} = \phi_I^{(1)} + \phi_S^{(1)} + \phi_R^{(1)} = \phi_D^{(1)} + \phi_R^{(1)}$. The hydrodynamic forces and moments are divided into two components: the “wave exciting force” due to $\phi_D^{(1)}$ and the force due to $\phi_R^{(1)}$ expressed as the added mass and damping coefficients.
The integrals to evaluate the hydrostatic pressure can be simplified by applying (2.57) and their variations with the results

$$F = -\rho \iint_{S_B} \phi_t^{(1)} n dS - \rho g A_{wp}\left(\xi_3^{(1)} + \alpha_1^{(1)} y_f - \alpha_2^{(1)} x_f\right) k \tag{2.60a}$$

$$M = -\rho \iint_{S_B} (x \times n)\phi_t^{(1)} dS + \\ -\rho g\left[-V\xi_2^{(1)} + A_{wp} y_f \xi_3^{(1)} + (V z_b + L_{22})\alpha_1^{(1)} - L_{12}\alpha_2^{(1)} - V x_b \alpha_3^{(1)}\right] i \\ -\rho g\left[-V\xi_1^{(1)} + A_{wp} x_f \xi_3^{(1)} - L_{12}\alpha_1^{(1)} + (V z_b + L_{11})\alpha_2^{(1)} - V y_b \alpha_3^{(1)}\right] j \tag{2.60b}$$

Where L_{ij} is the second moment over the waterplane area. For example, $L_{12} = \iint_{A_{wp}} xy dS$.
x_f and y_f are the coordinates of the center of floatation.

Following (2.8), the force can be represented by a discrete spectrum (the moment takes an identical form and is omitted here)

$$F = Re \sum_j F_j e^{i\omega_j t} \tag{2.61}$$

2.9 IRREGULAR FREQUENCIES

The Green function satisfies the free surface condition everywhere on the plane of the free surface, both outside and inside the body. Consequently, for bodies that intersect that surface, a discrete spectrum of irregular frequencies exists, where the solutions of the boundary integral equations either do not exist or are non-unique. The problem of irregular frequencies and its solution was thoroughly examined in Lee, Newman, and Zhu (1996) [20].

These irregular frequencies coincide with the eigenfrequencies of non-physical wave motions inside the body, where the same free surface condition is imposed on the interior free surface, and a homogeneous Dirichlet boundary condition is imposed on the body surface.

The connection between the irregular frequencies and the interior Dirichlet problem follows by noting that this problem can be solved in general by either the potential or source formulation, the one BEMUse uses.

However, the corresponding fluid motion inside the body, subject to a Dirichlet condition, would have a set of resonance frequencies at which non-trivial homogeneous solutions exist. The potential and source formulations for the exterior boundary value problem break down at the same frequencies owing to the relation of their kernels, so that of the integral equation for the interior Dirichlet problem. At the irregular frequencies, the Fredholm determinants of the two formulations vanish, and thus the solutions must be either non-unique or non-existent. The same set of irregular frequencies applies to the potential and source formulations and the second-order solution, since each of the corresponding integral equations has the same kernel or its transpose.

In the discrete problem (a consequence of the panel method), the condition number of the linear system increases near the irregular frequencies, indicating that the system is ill-conditioned in the vicinity of these frequencies, where the numerical solutions are wrong. The width of the wrong solution in terms of frequency interval may be reduced increasing the number of panels on the body, although this has a worsening effect on the computational cost of the calculations; moreover, it's often impossible to predict which frequencies generate these irregularities. Therefore, it's necessary to develop modified integral equations which avoid the effects of the irregular frequencies in practical applications.

Since the occurrence of the irregular frequencies is associated with the interior Dirichlet problem, their effects in waters of infinite or finite depth are similar.

Green's theorem yields a Fredholm integral equation for the unknown $\phi(x)$ over the domain S_b

$$2\pi\phi(x) + \iint_{S_b} \phi(\xi)\frac{\partial G(x;\,\xi)}{\partial n_\xi}d\xi = \iint_{S_b} q_b(\xi)G(x;\,\xi)d\xi + F(x) \tag{2.62}$$

Where

$$F(x) = \frac{1}{g}\iint_{S_f} q_f(\xi)G(x;\,\xi)d\xi \tag{2.63}$$

The normal vector n points out of the fluid domain, and S_f denotes the free surface exterior to the body.

While it's generally assumed that solutions of the boundary value problem for the potential ϕ are unique, in the unbounded fluid domain exterior to the body, it can be shown that non-trivial homogeneous solutions of (2.62) exist at the irregular frequencies. The existence of these solutions is associated with the non-physical portion of the free surface domain interior to the body in the definition of the Green function.

There are two methods to solve the problem of irregular frequencies, the Modified Green Function method, and the Extended Boundary Condition method. Since BEMUse uses the latter, the next paragraph will solely focus on that one.

2.9.1 Removal of irregular frequencies

The Extended Boundary method is used by WAMIT as well, and the procedure is explained well in its Theory Manual [12].

The extended boundary integral equations for ϕ_k are

$$2\pi\phi_k(x) + \iint_{S_b} \phi_k(\xi)\frac{\partial G(x;\ \xi)}{\partial n_\xi}d\xi + \int_{S_f} \phi'_k(\xi)\frac{\partial G(x;\ \xi)}{\partial n_\xi}d\xi = \iint_{S_b} n_k G(x;\ \xi)d\xi \quad (2.64a)$$

$$-4\pi\phi'_k(x) + \iint_{S_b} \phi_k(\xi)\frac{\partial G(x;\ \xi)}{\partial n_\xi}d\xi + \int_{S_f} \phi'_k(\xi)\frac{\partial G(x;\ \xi)}{\partial n_\xi}d\xi = \iint_{S_b} n_k G(x;\ \xi)d\xi \quad (2.64b)$$

Where ϕ'_k is an artificial velocity potential defined in the interior domain. Equations (2.64a) and (2.64b) are for x on S_b and S_i, respectively. These equations are solved simultaneously for ϕ_k on S_b and ϕ'_k on S_i. ϕ'_k is discarded after their solution since only ϕ_k on S_b is physically relevant.

The equations for the total diffraction potential ϕ_D are

$$2\pi\phi_D(x) + \iint_{S_b} \phi_D(\xi)\frac{\partial G(x;\ \xi)}{\partial n_\xi}d\xi + \int_{S_f} \phi'_D(\xi)\frac{\partial G(x;\ \xi)}{\partial n_\xi}d\xi = 4\pi\phi_I(x) \quad (2.65a)$$

$$-4\pi\phi'_D(x) + \iint_{S_b} \phi_D(\xi)\frac{\partial G(x;\ \xi)}{\partial n_\xi}d\xi + \int_{S_f} \phi'_D(\xi)\frac{\partial G(x;\ \xi)}{\partial n_\xi}d\xi = 4\pi\phi_I(x) \quad (2.65b)$$

The scattering potential has the same form as the radiation potential but $-\partial\phi_I/\partial n$ replaces n_k on the right-hand side of the equations (2.64a) and (2.64b).

The extended boundary integral equation for the source formulation of the radiation or scattering problem takes a form

$$2\pi\sigma(x) + \iint_{S_b} \sigma(\xi)\frac{\partial G(x;\ \xi)}{\partial n_\xi}d\xi + \int_{S_f} \sigma'_D(\xi)\frac{\partial G(x;\ \xi)}{\partial n_\xi}d\xi = g(x) \quad (2.66a)$$

$$-4\pi\sigma'_D(x) + \iint_{S_b} \sigma(\xi)\frac{\partial G(x;\ \xi)}{\partial n_\xi}d\xi + \int_{S_f} \sigma^{'(\xi)\frac{\partial G(x;\ \xi)}{\partial n_\xi}}d\xi = -V(x) \quad (2.66b)$$

Where $g(x) = n_k$ or $g(x) = -\partial\phi_I/\partial n$ for the radiation (scattering) problem.

A detailed analysis of the derivation of these equations is described, among others, by Zhu (1994) [19]. There, the author explains that because the kernel of the modified source integral equations is the transpose of those in the modified potential integral equations, the homogeneous solutions of the source integral equations should be trivial. Therefore, the extended boundary condition method in source formulation can also remove the irregular frequencies.

The solution of the integrals implies that the potential and velocity inside the body is zero. When we apply the extensions to the original boundary integral equations, the inside potential property is enforced in the new boundary integral equations, thus the potential inside the body is homogeneous for the integral equation of Extended Boundary Condition method. Therefore, the left-hand side of the equations (2.66a) and (2.66b) must be set equal to zero.

3. DESCRIPTION OF BEMUse

As previously stated, BEMUse is a hydrodynamic analysis model created at the Hermann-Föttinger Institut at the Technische Universität Berlin and developed inside QBlade software.

While the previous chapter illustrated the theory on which the model lays on, in this chapter an overview of how BEMUse operates is given.

3.1 METHOD OF SOLUTION

To achieve the complete hydrodynamic analysis of a wind turbine platform, BEMUse uses the Boundary Element Method (BEM). This, often referred to as a low-order panel method, allows us to discretize the solving partial differential equations using the definitions for the perturbation potentials for surface dipoles distributions and source distributions, and numerically solve for a finite number of degrees of freedom, i.e. panels. From the solution, the velocity vector field and the pressure distribution can be obtained. From the surface pressure distribution, the forces and moments acting on the submerged body are then calculated [21].

The critical property of the panel method is that the solution of the flow equations (obviously in 3D space) is wholly determined by the solution on the surface of the body only. This makes the geometric modeling of the problem a relatively simple task, as the geometry is described in terms of a body consisting of structured patches of surface grid, the so-called panels in the method. The figure below shows an example of paneling for a hemispherical platform, as generated by BEMUse.

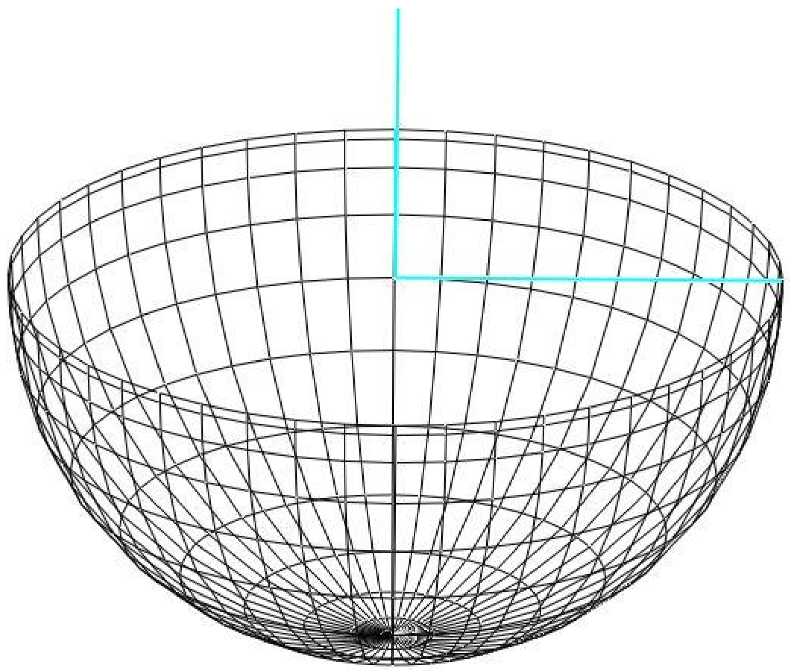

Figure 3.1. A hemisphere discretized with quadrilateral flat panels by BEMUse

In a low order panel method, the error in the solution is of *O(h)* and thus linearly dependent on a characteristic panel size h.

Dirichlet boundary conditions are enforced at a finite number of discrete points, so-called collocation points that are located right below the surface of the body panel centroids. Some characteristics of the approach followed are:

- Structured grids of quadrilateral panels represent body surface geometries, and the arbitrary translational and rotational motions of the geometry are specified in a hierarchical setup, which will be described afterward.
- Each panel on the body surface is assigned a constant strength dipole distribution and a constant strength source distribution.
- The perturbation velocity vectors at the panel corner points are determined by a 2D version of the Gradient Theorem.
- The hydrodynamic force and moment on each panel are determined through the integration of the surface pressure distribution, obtained by a bi-linear interpolation of all contributions in the Bernoulli equation that define the pressure. A summation then yields the force and moment acting on the whole body.

3.2 GEOMETRY

The surface of the body is discretized in a structured surface grid. The grid cells on the surface of the platform, called panels, are in the boundary integral discretization.

The cross-product of the vectors determines the direction of the vector normal to the surface and based on the centroid of each panel through diagonally opposite panel corner points.

$$\vec{n} = \left(\vec{x}_{i+1,j} - \vec{x}_{i,j+1}\right) \times \left(\vec{x}_{i+1,j+1} - \vec{x}_{i,j}\right) \tag{3.1}$$

Where i, j are the indices of each grid node, as BEMUse generates them in a structured order.

The value of $\vec{n}$ is then normalized to give the unit vector $\bar{n}_{mid} = \vec{n}/|\vec{n}|$. The panel area is approximated by a flat, non-curved panel surface representation and equal to $|\overrightarrow{n}|/2$.

3.3 SOLID BODY TRANSFORMATION

For the arbitrary motion of the geometry, the technique described in van Garrel (2003) [22] is used. At each time step, the new constellation of the geometry is determined. Solid body rotations and translations are performed using 4 x 4 transformation matrices expressed in a homogeneous coordinate system.

These matrices, which operate on homogeneous coordinates, are composed of the three components of a Cartesian vector supplemented with a 4th component equal to 1. A position vector $(x, y, z)^T$ is thus extended in the homogeneous form to $(x, y, z, 1)^T$.

The rotation matrix R for rotation of a position vector $\vec{x}$ about a general axis through the origin with direction $\bar{v} = (v_1, v_2, v_3)^T$ through an angle θ, interpreted in a right-hand rule sense, reads

$$R = \begin{pmatrix} v_1v_1d + c & v_1v_2d - v_3s & v_1v_3d + v_2s & 0 \\ v_2v_1d + v_3s & v_2v_2d + c & v_2v_3d - v_1s & 0 \\ v_3v_1d - v_2s & v_3v_2d + v_1s & v_3v_3d + c & 0 \\ 0 & 0 & 0 & 1 \end{pmatrix} \tag{3.2}$$

Where

$$\begin{gathered} c = cos\theta \\ s = sin\theta \\ \mathrm{d} = 1 - cos\theta \end{gathered} \tag{3.3}$$

And

$$\bar{v} \cdot \bar{v} = 1 \tag{3.4}$$

The rotation of a position vector $\vec{x}$ is now accomplished by a matrix multiplication that gives a new position vector $\vec{x}_{new} = R\vec{x}$.

Similarly, the translation of a position vector $\vec{x}$ can be performed through multiplication with the translation matrix T such that $\vec{x}_{new} = T\vec{x}$. The translation matrix is formed by

$$T = \begin{pmatrix} 1 & 0 & 0 & t_1 \\ 0 & 1 & 0 & t_2 \\ 0 & 0 & 1 & t_3 \\ 0 & 0 & 0 & 1 \end{pmatrix} \tag{3.5}$$

Where $(t_1, t_2, t_3)^T$ is the Cartesian translation vector.

The transformation matrix for a translation in the reverse direction $-(t_1, t_2, t_3)^T$ is the inverse T^{-1} of matrix T. Rotation about a general axis not through the origin can be performed by a compound transformation matrix A, which is composed of a translation of the axis to the origin by T, a rotation R, and a translation T^{-1} back to the original position:

$$\vec{x}_{new} = T^{-1}\big(R(T\vec{x})\big) = A\vec{x} \tag{3.6}$$

For a set of position vectors $\vec{x}$, it is more efficient to compute the compound transformation matrix A first and perform the matrix multiplication with all position vectors next.

3.4 Dipole potential and velocity

The velocity potential induced at point $\vec{x}$ by a panel with surface S_j and dipole distribution $\mu(\vec{y})$ is given by

$$\phi_\mu(\vec{x}) = -\frac{1}{4\pi}\iint\limits_{S_j} \mu \frac{\bar{n} \cdot \vec{r}}{r^3} dS \tag{3.7}$$

Where

$$\vec{r} = \vec{x} - \vec{y}, \quad r = |\vec{r}|, \quad and\ \vec{y} \in S_j \tag{3.8}$$

The usual approach taken in low-order panel methods is to use a flat surface approximation for the panel geometry, for which analytical results exist for the integral in equation (3.7) [23]. In general, however, flat panels lead to gaps between the panels in the surface approximation of a curved surface, that grow larger with increasing surface curvature and twist.

Panel method is very useful in the case of very large domains, like a floating platform, where a Finite Element approximation would not be practical [24]. This is because only the boundary of the domain needs to be discretized.

Another advantage is that in some applications like the one of interest for this study, the physically relevant data are given not by the solution in the interior of the domain, but rather by the boundary values of the solution or its derivatives. These data can be obtained directly from the solution of boundary integral equations, whereas boundary values obtained from FEM solutions are, in general, not very accurate [25].

To conclude this chapter, a brief overview of the steps followed by a Panel Method software in case of hydrodynamic diffraction problems is reported [26]:

1) Use Green's theorem to derive integral equations for velocity potentials on the body boundary
2) Discretize the body surface by a large number N of panels
3) The sources and dipole moments are assumed constant on each panel $\rightarrow$ total of N unknowns
4) The potential is evaluated at the centroid of each panel and set equal to the normal incident potential
5) Solve the system of equations
6) Compute required forces and moments

3.5 Influence coefficients

The source potential, or Green function, is the fundamental analysis of wave-induced motions and forces acting on floating vessels. It satisfies the linearized boundary condition at the free surface and the radiation condition. BEMUse's numerical model is based on the distribution of sources and dipoles, located on the submerged portion of the body surface. This procedure can be justified by Green's theorem and requires the solution of an integral equation in the domain of the body surface for the velocity potential.

The Green function can be expressed as the sum of the free-space singularity (Rankine source) and a component that accounts for the free surface. The latter part can be further decomposed into a non-oscillatory local flow component and a wave component, which is dominant in the far-field. This one, in its basic decomposition, is defined in terms of special real functions: Bessel functions J_0 and J_1 of a single variable.

The non-oscillatory local flow components in the expressions for the Green function and its gradient are real functions of two variables and are defined by single integrals. The two variables are the field point (identified by the Cartesian coordinate system (x, y, z)) and the source point marked by (ξ, η, ζ).

Near-field and far-field approximations to these components are used to remove the near-field singularities and to reduce the unbounded region to a finite one, making it possible to use polynomial approximations. These are very well-suited for highly efficient computation.

In its conventional form, taken from Wehausen and Laitone (1960) [14], the source potential is defined by the expression

$$G = [R^2 + (z-\zeta)^2]^{-\frac{1}{2}} + \int_0^\infty \frac{k+K}{k-K} e^{k(z+\zeta)} J_0(kR)dk \tag{3.9}$$

Where J_0 denotes the Bessel function of the first kind, order zero, and the contour of integration passes above the pole k to satisfy the radiation condition of outgoing waves at infinity. K is defined by gravity and frequency as $K = \omega^2/g$, which corresponds to the wavenumber in the infinite-depth case. R is instead the radius expressing the horizontal coordinate defined by the magnitude of the horizontal vectors with components $(x-\xi, y-\eta)$

In Liang, Wu, and Noblesse (2018) [27] it is expressed in a more compact way as

$$4\pi G = -\frac{1}{r} - \frac{1}{d} + L + \mathrm{W} \tag{3.10}$$

Where L represents a non-oscillatory local flow component, and W is a wave component. This basic decomposition is not unique.

The gradient of the Green function is given by

$$4\pi G_z = \frac{z-\zeta}{r^3} + \frac{\nu}{d^3} + L_z + W \; where \; L_z = -\frac{1}{d} + L \tag{3.11a}$$

$$4\pi G_h = \frac{h}{r^3} + \frac{h}{d^3} + L_h + W_h \tag{3.11b}$$

$$4\pi G_x = \frac{x-\xi}{h} G_h \; and \; 4\pi G_y = \frac{x-\eta}{h} G_h \tag{3.11c}$$

Where the subscript z, h and x identify the direction of derivation. To calculate the linear and mean drift wave loads on the platform's surface, a constant panel boundary element method based on combined source and dipole distributions is used. Irregular frequencies are removed via the extension of the flow region to the waterplane area. Specifically, these two integral equations are solved:

$$\frac{1}{2}\phi(x) + \iint_{\Sigma^H} \phi(\xi) \frac{\partial G(x,\xi)}{\partial n_\xi} dS + \iint_{\Sigma^I} \mu(\xi) \frac{\partial G(x,\xi)}{\partial n_\xi} dS = \iint_{\Sigma^H} G(x,\xi) \frac{\partial \phi(\xi)}{\partial n_\xi} dS \tag{3.12}$$

$$\mu(x) + \iint_{\Sigma^H} \phi(\xi) \frac{\partial G(x,\xi)}{\partial n_\xi} dS + \iint_{\Sigma^I} \mu(\xi) \frac{\partial G(x,\xi)}{\partial n_\xi} dS = \iint_{\Sigma^H} G(x,\xi) \frac{\partial \phi(\xi)}{\partial n_\xi} dS \tag{3.13}$$

On Σ^H and $\Sigma^{I,}$ respectively.

They are needed to determine the flow potential ϕ on the hull surface Σ_H of the floating body and the density μ of the dipole distribution over the interior free surface Σ_I. The singular Rankine source component $1/r + 1/d$ in (3.10) and its gradient in (3.11a-3.11c) are analytically integrated over a flat panel, and the weakly-singular local flow component L and its gradient in (3.10) or (3.11a-3.11c) are numerically integrated via a Gaussian quadrature rule with four Gaussian points in the nearfield and one point in the far-field [27].

These two integral equations are imposed on each panel of the body surface, generating a linear system of N equations, where N is the number of panels. This linear system can be expressed in matrix form:

$$\phi = A^{-1}B\phi' \tag{3.14}$$

Where A is an N by N matrix whose coefficients are the Green's function derivative as expressed in the first integral of equation (3.12), ϕ is the vector of unknowns - the values of the velocity potential at the centroid of each panel – and B is another N by N matrix containing the values of the Green function at each centroid. Finally, ϕ' is another vector, containing the Green's function derivative for the direction normal to the panel.

3.6 Boundary conditions

To solve the linear system, another fundamental element is the imposition of appropriate boundary conditions to the problem. As Newman (1999) [13] states, two different types of conditions must be discussed: a kinematic one corresponding to a statement regarding the velocity of the fluid on the boundary, and a dynamic boundary condition corresponding to an account of the forces on the boundary.

A kinematic condition is appropriate on any boundary surface with a specified geometry and position. Whether the boundary is a fixed and rigid body (most straightforward case, corresponding to the cases studied in this thesis), or one moving with prescribed velocity U through the fluid, the physically relevant condition for the flow at the boundary is that the normal component $V \cdot n$ of the velocity must be equal to the normal velocity $U \cdot n$ of the boundary surface itself. In other words, no fluid can flow through the boundary surface. This condition, also known as zero penetration condition, can be expressed in terms of the velocity potential as

$$\frac{\partial \phi}{\partial n} = U \cdot n = 0 \tag{3.15}$$

Where $\partial/\partial n$ denotes the derivative in the direction of the unitary normal n directed out of the fluid.

In the absence of viscous shear stresses (inviscid flow), only the normal component of the fluid velocity is prescribed on the boundary.

As the derivative of the velocity potential is the fluid velocity, this condition can also be written as

$$\phi \cdot \vec{n} = \frac{\partial \phi}{\partial n} \tag{3.16}$$

This means that the fluid's velocity component normal to the surface of the body must be equal to 0 for each panel. This condition assures that the flow does not penetrate the surface of the body.

The kinematic boundary condition (3.15) contains precisely the right amount of information regarding the fluid motion. On the other hand, there will be problems where the position and velocity of the boundary are unknown; in particular, on the free surface where waves occur and the form of the wave motion and free surface elevation is not known a priori. In this instance, the kinematic boundary condition (3.15) remains valid, but the velocity *U* of the boundary is unknown. Therefore, additional information must be provided, in the form of the free surface boundary condition, expressed as

$$\frac{\partial^2 \phi}{\partial t^2} + g\frac{\partial \phi}{\partial z} + 2\nabla\phi \cdot \nabla\frac{\partial \phi}{\partial t} + \frac{1}{2}\nabla\phi \cdot \nabla(\nabla\phi \cdot \nabla\phi) = 0 \tag{3.17}$$

And applied on the exact free surface:

$$\zeta(x,y) = -\frac{1}{g}\left(\frac{\partial \phi}{\partial t} + \frac{1}{2}\nabla\phi \cdot \nabla\phi\right)_{z=\zeta} \tag{3.18}$$

This formula can be significantly simplified under the assumptions of small wave slope and harmonic solution as follows:

$$\frac{\partial \phi}{\partial z} - \nu\phi = 0 \tag{3.19}$$

Here, *ν* represents the non-dimensional wave number of the problem ($\nu = \omega^2/g$ in the infinite-depth case, where *ω* is the wave frequency).

The definition of the boundary conditions wouldn't be complete without a statement of what happens far from the body, i.e. the asymptotic behavior when $r \to \infty$, with *r* the distance from the evaluation point. Thus, the radiation condition is imposed, stating that the disturbance potential vanishes for *r* going to infinity.

Apart from these fundamental boundary conditions required by BEMUse to carry out its calculations, there are other more general conditions which need to be respected when working with hydrodynamic modeling softwares.

The pressure is constant across the free surface interface: $p = p_{atm}$ on $z = \eta$.

$$p = -\rho\left\{\frac{\partial \phi}{\partial t} - \frac{1}{2}V^2 - gz\right\} + c(t) = p_{atm} \tag{3.20}$$

With the choice a suitable integration constant, $c(t) = p_{atm}$, the boundary condition on $z = \eta$ becomes

$$\rho\left\{\frac{\partial \phi}{\partial t} + \frac{1}{2}V^2 + g\eta\right\} = 0 \tag{3.21}$$

Once a particle is on the free surface, it always remains there. Similarly, the normal velocity of a particle on the surface is equal to the normal velocity of the surface itself.

$$z_p = \eta(x_p, t) \tag{3.22}$$

$$z_p + \delta z_p = \eta(x_p + \delta x_p, t + \delta t) = \eta(x_p, t) + \frac{\partial \eta}{\partial x}\delta x_p + \frac{\partial \eta}{\partial t}\delta t$$

On the free surface, where $z_p = \eta$, we can reduce the above equation to

$$\delta z_p = \frac{\partial \eta}{\partial x}u\delta t + \frac{\partial \eta}{\partial t}\delta t \tag{3.23}$$

And substitute $\delta z_p = w\delta t$ and $\delta xp = u\delta t$ to demonstrate that the normal velocity follows the particle:

$$w = u\frac{\partial \eta}{\partial x} + \frac{\partial \eta}{\partial t} \tag{3.24}$$

on $z = \eta$.

On an impermeable body boundary $B\ (x, y, z, t) = 0$, the velocity of the fluid normal to the body must be the same as the body velocity in that direction:

$$\vec{v} \cdot \hat{n} = \phi \cdot \hat{n} = \frac{\partial \phi}{\partial t} = \vec{U}(\vec{x}, t) \cdot \hat{n}(\vec{x}, t) = U_n \tag{3.25}$$

On $B = 0$.

Alternatively, a particle P on B remains always on B; i.e. B is a material surface.

As an example, if P is on B at some time $t = t_0$ such that

$$B(\vec{x}, t_0) = 0, then\ B(\vec{x}, t_0) = 0\ for\ all\ t, \tag{3.26}$$

So that if we were to follow P, then $B = 0$ always. Therefore:

$$\frac{DB}{Dt} = \frac{\partial B}{\partial t} + (\nabla\phi \cdot \nabla)\mathrm{B} = 0\ on\ \mathrm{B} = 0 \tag{3.27}$$

As an example, a flat bottom at $z = -H$ is considered:

$$\frac{\partial \phi}{\partial z} = 0\ on\ z = -H \tag{3.28}$$

3.7 LINEAR SYSTEM

For numerical evaluations, the integral equation should be avoided due to its high computational cost for every panel created on the body surface.

It's important to note that the body surface, to be accurately reproduced with panels, requires a high number of them. This means that as an average, each surface is divided into approximately 10^2 to 10^4 panels, each one of them requiring a solving equation.

The corresponding linear system of equations is characterized by a square matrix of complex coefficients with the same dimension, which must be solved using linear algebra.

A brief overview of how the matrix and vectors are generated has been previously given. Now, a more in-depth analysis of the single values composing the matrix follows.

Matrix A in equation (3.14) contains the derivative of the Green's function to the direction normal to the panel, each row comprising the value of this derivative for the panel currently under inspection, while each column refers to a different panel on the surface. This is the basis of the dipole concept.

$$A = \begin{bmatrix} G_{11} & \cdots & G_{1N} \\ \vdots & \ddots & \vdots \\ G_{N1} & \cdots & G_{NN} \end{bmatrix} \tag{3.29}$$

The vector ϕ is the unknown, and after the solution of the linear system will contain the value of the potential on the centroid of each panel.

The matrix B instead contains the value of the Green function evaluated with the same procedure followed for A; therefore, each row refers to a certain centroid, and each column measures the effect of the other panels on it. Like A, matrix B has the form:

$$B = \begin{bmatrix} G_{11} & \cdots & G_{1N} \\ \vdots & \ddots & \vdots \\ G_{N1} & \cdots & G_{NN} \end{bmatrix} \tag{3.30}$$

Finally, the vector ϕ' contains the values of the normal derivative of the velocity potential, again calculated at each centroid. This vector is known because the velocity field around the body is defined. It thus has the form:

$$\phi' = \begin{bmatrix} \frac{\partial \phi_1}{\partial n} \\ \cdots \\ \frac{\partial \phi_N}{\partial n} \end{bmatrix} \tag{3.31}$$

Among these four components, only the vector ϕ is unknown, while the rest is known. Therefore, the linear system can be solved calculating the inverse of matrix A, using equation (3.14).

The solution obtained is thus the vector containing the values of the velocity potential on the centroid of each panel. This procedure, which is the most computationally expensive step in the solution of the problem, allows BEMUse to obtain the value of the potential, which is then needed to calculate the forces and the pressure acting on the body surface.

The linear system generated implementing the solution procedure described in Chapter 2 is solved by an iterative method (or block iterative method, or Gauss elimination method).

In most cases, the iterative method converges in 10-15 iterations and is the most efficient way to solve the linear system. On the other hand, using this method all or part of the matrix may be stored on the hard disk and then recovered at each iteration.

There are, though, a few problems for which the iterative method is slowly convergent or non-convergent due to bad conditioning of the linear system, like in the case of barges with a shallow draft or multiple bodies separated by small gaps. The iterative method may also be slowly convergent in the case of the linear system for the extended boundary integral equation. In this circumstance, other methods are more efficient.

3.8 DISCRETIZATION

Boundary Element Method is often referred to as the Panel Method because it requires the surface of the body under examination to be discretized in a finite number of diffraction panels to carry out the analysis. As previously stated, to get accurate simulations hundreds or even thousands of panels are needed, and they need to be constructed consistently to solve the linear system subsequently.

BEMUse, like many other hydrodynamic analysis softwares, uses quadrilateral panels.

They are created starting from the discrete grid points whose coordinates are determined by the parametric equations that define the geometry of the body. The level of refinement of the grid can be freely set by the user, although it must always be kept in mind that a higher number of panels increases the precision of the results, but on the other hand quickly increases the computational cost of the analysis.

Once all the points have been defined, the adjacent ones need to be grouped to form the panels. BEMUse does so in a consistent way, i.e. following the same counterclockwise order. This is required because the order in which the points are accounted for determines the direction of the normal vector coming out from the centroid of the panel. All the vectors have to indeed point away from the fluid, i.e. inside the body. In the following figure, a clear example of the result obtained through this procedure can be seen.

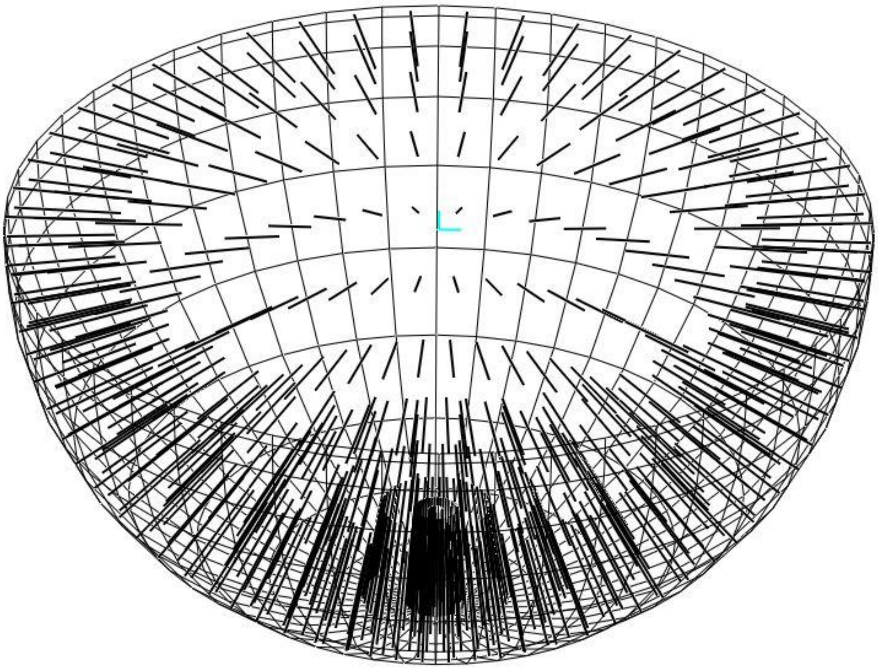

Figure 3.2. All the vectors normal to the panel surface point away from the fluid, i.e. inside the body.

Often, to increase the mesh's refinement near borders or changes in geometry, where the velocity potential is expected to undergo the most significant variations, cosine spacing is used. This allows achieving the objective without increasing the total number of grid points and, consequently, panels.

When generating the grid points, it's essential to be careful not to create a point twice in the same spot because that could create some problems in the handling of irregular frequencies. This risk is particularly present in the case of symmetrical geometry, where the points on the axis separating the quadrants need to be taken care of with particular attention.

It's important to note that the panels created by BEMUse are linear panels, which means that they are flat, with their vertices on the same geometric plane. This is the main reason why such a high number of panels is needed. Curved surfaces would be poorly approximated with a less refined discretization.

As already stated, BEMUse evaluates the velocity potential on the centroid of each panel, while other softwares do that on the grid points of the body.

3.9 From potential to forces

Calculating the velocity potential is necessary for then being able to calculate the forces and pressures acting on the body. To get there, BEMUse uses the equations written in Chapter 2. In particular, the total pressure working on the surface of the body is calculated through the Bernoulli equation

$$p(\vec{x}, t) = -\rho \left(\frac{\partial \phi}{\partial t} + \frac{1}{2} \nabla \phi \cdot \nabla \phi + gz \right) \tag{3.32}$$

There are although numerous other parameters of great interest when dealing with floating platforms and hydrodynamics in general.

3.9.1 Added mass and damping

First there is added mass, which is defined as the inertia added to a system because a body moves or deflects some volume of the fluid surrounding it when subjected to forces, thus accelerating and decelerating. Since it identifies inertia, it's expressed in kg in the case of translational motions and $kg \cdot m^2$ for rotational ones. In alternative added mass can also be expressed in dimensionless form, becoming the added mass coefficient. To obtain it, it's sufficient to divide the added mass times the displaced fluid mass.

Then there is damping, which in physics is generally described as the influence on an oscillatory system which reduces, restricts or prevents its oscillation. Damping is directly proportional to the relative velocity between the two bodies (platform and water, in this case). In the case of fluids, we refer to radiation damping which is mostly due to the viscosity of the water. It is expressed in kg/s for translational motions and in $kg \cdot m^2/s$ for rotational ones. Also in this case, a dimensionless damping coefficient can be expressed as the ratio of the calculated damping and the mass of displaced water.

The added mass and damping are obtained integrating the value of the radiation potential over the body:

$$A_{ij} - \frac{i}{\omega} B_{ij} = \iint_S n_i \phi_{r,j} dS \tag{3.33}$$

Where the subscript i indicates the particular direction of the force and j the coordinate in which the surface oscillation occurs. A_{11}, therefore, designates the x-forces caused by an oscillation in the x-direction. This kind of motion is commonly referred to as surge motion. In the y-direction it's called sway, and in z-direction it's heave. For rotational motions, rotation around the x-, y- and z-axis are called roll, pitch and yaw, respectively.

In WAMIT the non-dimensional added mass and damping coefficients are obtained as follows

$$\bar{A}_{ij} = \frac{A_{ij}}{\rho L^k} \qquad \bar{B}_{ij} = \frac{B_{ij}}{\rho L^k \omega} \tag{3.34 a and b}$$

Where $k = 3$ for both i, j being equal to 1, 2 or 3; $k = 4$ for $i = 1, 2, 3$ and $j = 4, 5, 6$ or $i = 4, 5, 6$ and $j = 1, 2, 3$; $k = 5$ for both $i, j = 4, 5, 6$.

3.9.2 Exciting forces

The periodic forces on the body which arise due to the diffraction of the incoming harmonic wave are called exciting forces. To calculate them, the potential of the incoming wave is needed. In the infinite-depth case, it's expressed as

$$\phi_I = \frac{igA}{\omega} e^{\nu z} e^{i\nu(x\, cos\beta + xy\, sin\beta)} \tag{3.35}$$

Where A is the wave's amplitude, and β is its heading. Making use of Haskind relations for the diffraction potential, the forces can be expressed as a function of the radiation potential defined previously for the oscillating body:

$$X_I = -i\omega\rho \iint_S \left(n_i \phi_i - \frac{\partial \phi_i}{\partial n} \phi_j \right) dS \tag{3.36}$$

This allows to avoid the calculation of the diffraction potential on the surface, but simply to manipulate the results of the radiation potential. The exciting forces differ according to the direction of the incoming waves. Therefore, the results obtained must always be expressed indicating the angle which they refer to. This angle is usually measured starting from the positive *x*-axis. In this text, an angle of 45° was always used.

Exciting forces are expressed in N/m for translational motions and in Nm/m for rotational ones, but they are also found in their non-dimensional form

$$\bar{X}_i = \frac{X_i}{\rho g A L^m} \tag{3.37}$$

Where $m = 2$ for $i = 1, 2, 3$ and $m = 3$ for $i = 4, 5, 6$.

3.9.3 Response Amplitude Operators

The Response Amplitude Operator, or RAO, is an indication of the degree of movement induced in a floating body due to a passing hydrodynamic wave. RAOs can be calculated for each degree of freedom of the body, both translational and rotational. Like the exciting force, the direction of the incoming wave must be defined. As before, 45° was always the choice. The formula used to calculate each RAO is taken from Baghfalaki, Das, and Das (2012) [28]:

$$Z_i(\omega) = \frac{X_i(\omega)}{D_i} = \frac{F_i(\omega)}{-\omega^2(A_{ii}(\omega) + M_{ii}) + i\omega B_{ii}(\omega) + C_{ii}} \tag{3.38}$$

Where $X_k\ (\omega)$ is the motion in the frequency domain, and D_k is the corresponding wave amplitude. F_k is the exciting force, A_{kk} is the value of added mass, M_{kk} the mass and inertia matrix, B_{kk} is the damping coefficient, C_{kk} is the value of the hydrostatic restoring matrix and ω is the frequency of the waves.

The mass and inertia matrix contains the value of mass and rotational inertia of the body under inspection and is defined as

$$M_{ii} = \begin{bmatrix} m & 0 & 0 & 0 & mz_g & -my_g \\ 0 & m & 0 & -mz_g & 0 & mx_g \\ 0 & 0 & m & my_g & -mx_g & 0 \\ 0 & -mz_g & my_g & I_x & -I_{xy} & -I_{xz} \\ -mz_g & 0 & -mx_g & -I_{yx} & I_y & -I_{yz} \\ -my_g & mx_g & 0 & -I_{zx} & -I_{zy} & I_z \end{bmatrix} \tag{3.39}$$

On the other hand, the hydrostatic restoring matrix is defined as follows in the WAMIT User Manual [29]

$$C_{ii} = \begin{bmatrix} 0 & 0 & 0 & 0 & 0 & 0 \\ 0 & 0 & 0 & 0 & 0 & 0 \\ 0 & 0 & C_{3,3} & C_{3,4} & C_{3,5} & 0 \\ 0 & 0 & 0 & C_{4,4} & C_{4,5} & C_{4,6} \\ 0 & 0 & 0 & 0 & C_{5,5} & C_{5,6} \\ 0 & 0 & 0 & 0 & 0 & 0 \end{bmatrix} \tag{3.40}$$

Where

$$C(3,3) = \rho g \iint_{S_b} n_3 dS \tag{3.41a}$$

$$C(3,4) = \rho g \iint_{S_b} y n_3 dS \tag{3.41b}$$

$$C(3,5) = -\rho g \iint_{S_b} x n_3 dS \tag{3.41c}$$

$$C(4,4) = \rho g \iint_{S_b} y^2 n_3 dS + \rho g V z_b - mgz_g \tag{3.41d}$$

$$C(4,5) = -\rho g \iint_{S_b} xy n_3 dS \tag{3.41e}$$

$$C(4,6) = -\rho g V x_b + mgx_g \tag{3.41f}$$

$$C(5,5) = \rho g \iint_{S_b} x^2 n_3 dS + \rho g V z_b - mgz_g \tag{3.41g}$$

$$C(5,6) = -\rho g V y_b + mgy_g \tag{3.41h}$$

V is the volume of the body, ρ is the density of the water, and m is the mass of the body. The coordinates with subscript b refer to the center of buoyancy of the body, the ones with subscript g to its center of mass.

To improve the computational performance of the software, the surface integrals are calculated as the discrete sum of the values on each panel. x and y are thus the coordinates of each centroid, and n is the vector normal to the surface, with its three components.

These values are then normalized as follows:

$$\bar{C}(3,3) = C(3,3)/\rho g L^2 \tag{3.42a}$$

$$\bar{C}(3,4) = C(3,4)/\rho g L^3 \tag{3.42b}$$

$$\bar{C}(3,5) = C(3,5)/\rho g L^3 \tag{3.42c}$$

$$\bar{C}(4,4) = C(4,4)/\rho g L^4 \tag{3.42d}$$

$$\bar{C}(4,5) = C(4,5)/\rho g L^4 \tag{3.42e}$$

$$\bar{C}(4,6) = C(4,6)/\rho g L^4 \tag{3.42f}$$

$$\bar{C}(5,5) = C(5,5)/\rho g L^4 \tag{3.42g}$$

$$\bar{C}(5,6) = C(5,6)/\rho g L^4 \tag{3.42h}$$

Where L is the characteristic length of the body.

RAOs have the dimension of m/m for translational motions because they measure the ratio between the motion of the body and the amplitude of the wave, while rotational ones are expressed in $°/m$, as they evaluate the ratio between the angular motion of the body and, again, the amplitude of the wave. As for the other parameters calculated, also RAOs have their non-dimensional form

$$\bar{Z}_i = \frac{Z_i}{\frac{A}{L^n}} \tag{3.43}$$

Where $n = 0$ for $i = 1, 2, 3$ and $n = 1$ for $i = 4, 5, 6$.

4. WAMIT COMPARISON

In the process of validating BEMUse, the result obtained with it must be very similar or, at best, equal to the ones given by already well-established hydrodynamic softwares. For this comparison to be as thorough and accurate as possible, the values of the four hydrodynamic coefficients given by BEMUse are compared to the ones of two other well-known softwares like WAMIT and AQWA. The comparison with WAMIT is essential because BEMUse's theoretical basis is the same. The comparison with AQWA is also of great interest, as it is the hydrodynamic analysis tool inside the ANSYS Workbench, one of the most widely used engineering softwares in the world. Only the close accordance with results between all the outputs can confirm the accuracy of BEMUse.

The first comparison was carried out against the 'WAMIT-MOSES Hydrodynamic Analysis Comparison Study' (2000) by the Hull Engineering Department [30]. In their study, the researchers compared the results obtained with the diffraction and radiation simulation software WAMIT to the ones given by MOSES, a software that was originally developed for installation simulation, fatigue, and global motion analysis. Since the latter has the same 3-D diffraction and radiation module as the former, they thought it could be used for the same kind of platform studies with excellent results.

As the interest in the use of MOSES is modest for the scope of this thesis, only the results given by WAMIT were considered.

The analysis was performed on three simple geometries: a cylinder, a parallelepipedal box, and the ISSC Tension Leg Platform.

For all of them, precise indications of dimensions, mass, and number of panels used for the discretization were given, making it easy to replicate the analysis with BEMUse. All the data are reported in the table below. The column 'CoG' sets the depth at which the Center of Gravity is set for each geometry. It's expressed in meters in the z-direction.

Type	Length (m)	Beam/ Diameter (m)	Draft (m)	Displacement (Metric-Tons)	CoG (m)	N of panels
Cylinder	200.0	40.0	200.0	256,011.0	200.0	1120
Box	200.0	40.0	28.0	229,645.0	28.0	1264
TLP	51.6	51.6	35.0	52,761.0	35.0	512

Table 4.1. Geometrical and physical data of the three geometries.

The geometry and the mesh used are shown in the following figures, taken from BEMUse's GUI.

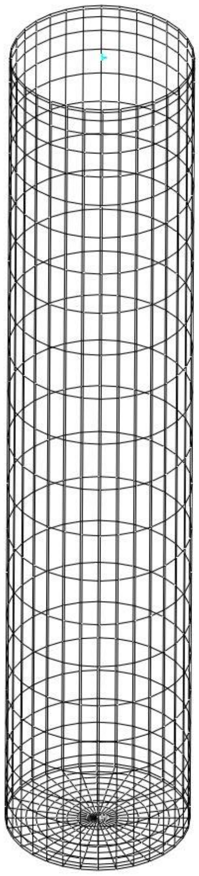

Figure 4.1. The cylinder generated by BEMUse. The cosine spacing is visible on the lateral surface.

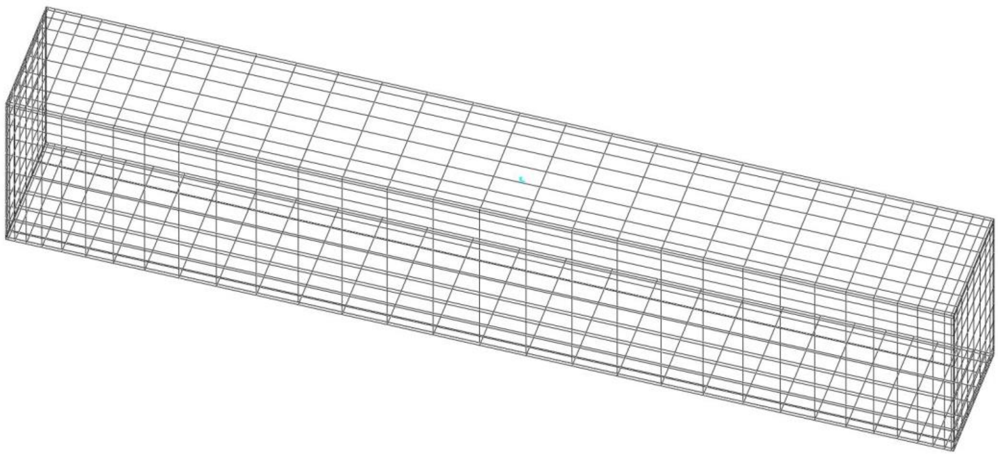

Figure 4.2. The box, a parallelepipedal barge. Again, cosine spacing is evident on all sides.

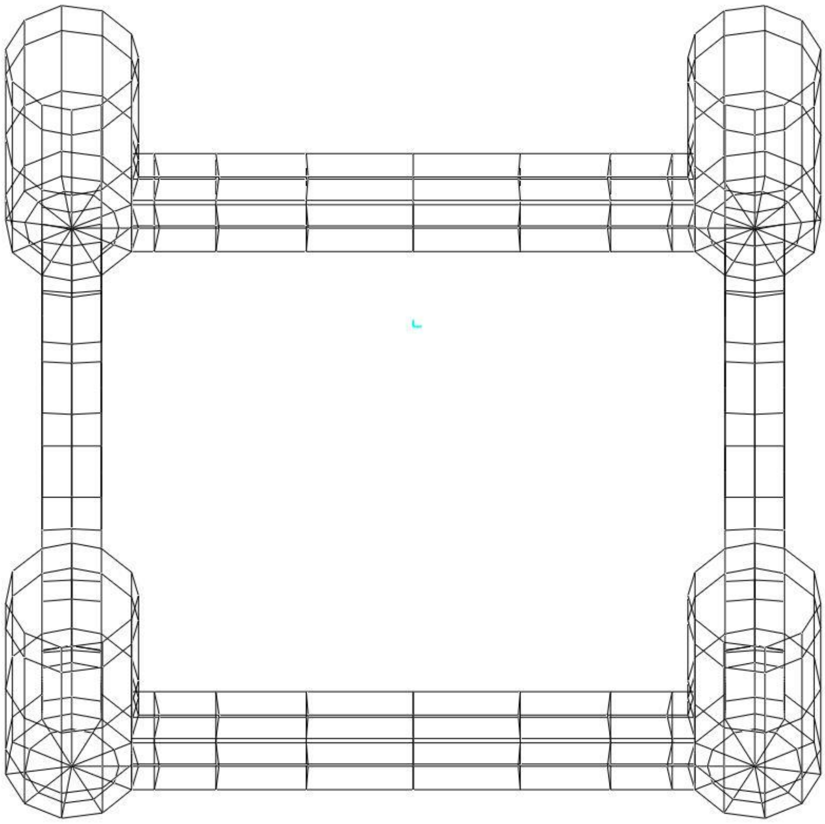

Figure 4.3. The Tension Leg Platform. Only the section below the water is generated.

The wave periods used in the numerical calculation were selected from 4 seconds to 42 seconds for a total of 20 steps separated by an increment of two seconds. This interval covers a wide range of waves.

The hydrodynamic coefficients (added mass and damping), the wave exciting forces, and the response amplitude operators were extracted from BEMUse and compared with WAMIT results. To do so, as these had undergone a normalization with respect to mass and wave amplitude, so had to do BEMUse's.

The normalization for each parameter is reported in the following table. *A* is the amplitude of the incoming wave, which is set equal to 1 for all the simulations.

Resulting Components	Units	Normalized variable
Added mass coefficient	Mass	A_{ij}/Mass
Damping coefficient	Mass/Time	SQRT(B_{ij}/Mass)
Wave exciting forces	Tons	Tons/A
Wave exciting moments	Tons*Meter	Tons*Meter/A
Linear motion RAO	Meter	Meter/A
Angular motion RAO	Degree	Degree/A

Table 4.2. Normalization factors for the four parameters evaluated.

For all the values, a wave heading of 45° starting from the *x*-axis was considered.

4.1 CYLINDER

The number of panels for the cylinder is the same as for the WAMIT experiment, 1120. This means that its base was discretized in 32 azimuthal sections and 9 radial ones. The lateral surface is divided into 32 sections. To achieve a more refined grid near the free surface and on edges, a cosine spacing scheme was used, like the researchers in Hull seem to have done.

The mass of the cylinder is calculated multiplying its displacement times the density of seawater, which is equal to $\rho = 1025 \text{ kg/m}^3$. The result is m = 2.55958e+08 kg. The center of mass, which also corresponds to the center of buoyancy, is placed at half of the cylinder's draft, on its central axis.

For the definition of the moments of inertia I_{xx}, I_{yy} and I_{zz}, as no precise information was given in the paper, the parallel axis theorem was used to translate the values referring to rotations around the axis of symmetry to rotations around the free water surface. These are the values obtained.

$$I_{xx} = I_{yy} = \frac{1}{12} m(3R^2 + L^2) + m\left(\frac{L}{2}\right)^2 = 3.43837e + 12\ kg \cdot m^2 \tag{4.1}$$

$$I_{zz} = \frac{1}{2} mR^2 = 5.11917e + 10\ kg \cdot m^2 \tag{4.2}$$

Where R and L are the radius and the height of the cylinder, respectively.

In the figure below, the different colors of the panels illustrate the different values of the velocity potential on the surface of the cylinder for a given wave period. The red color identifies higher values, blue lower ones. In the next few pages, instead, the results for this geometry are reported.

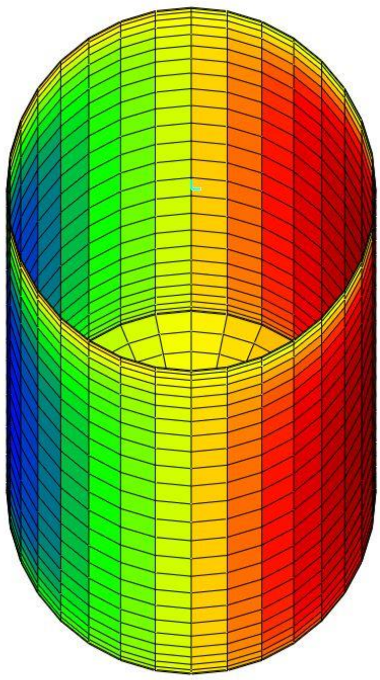

Figure 4.4. The colorized panels give an immediate idea of the potential distribution.

4.1.1 Added mass

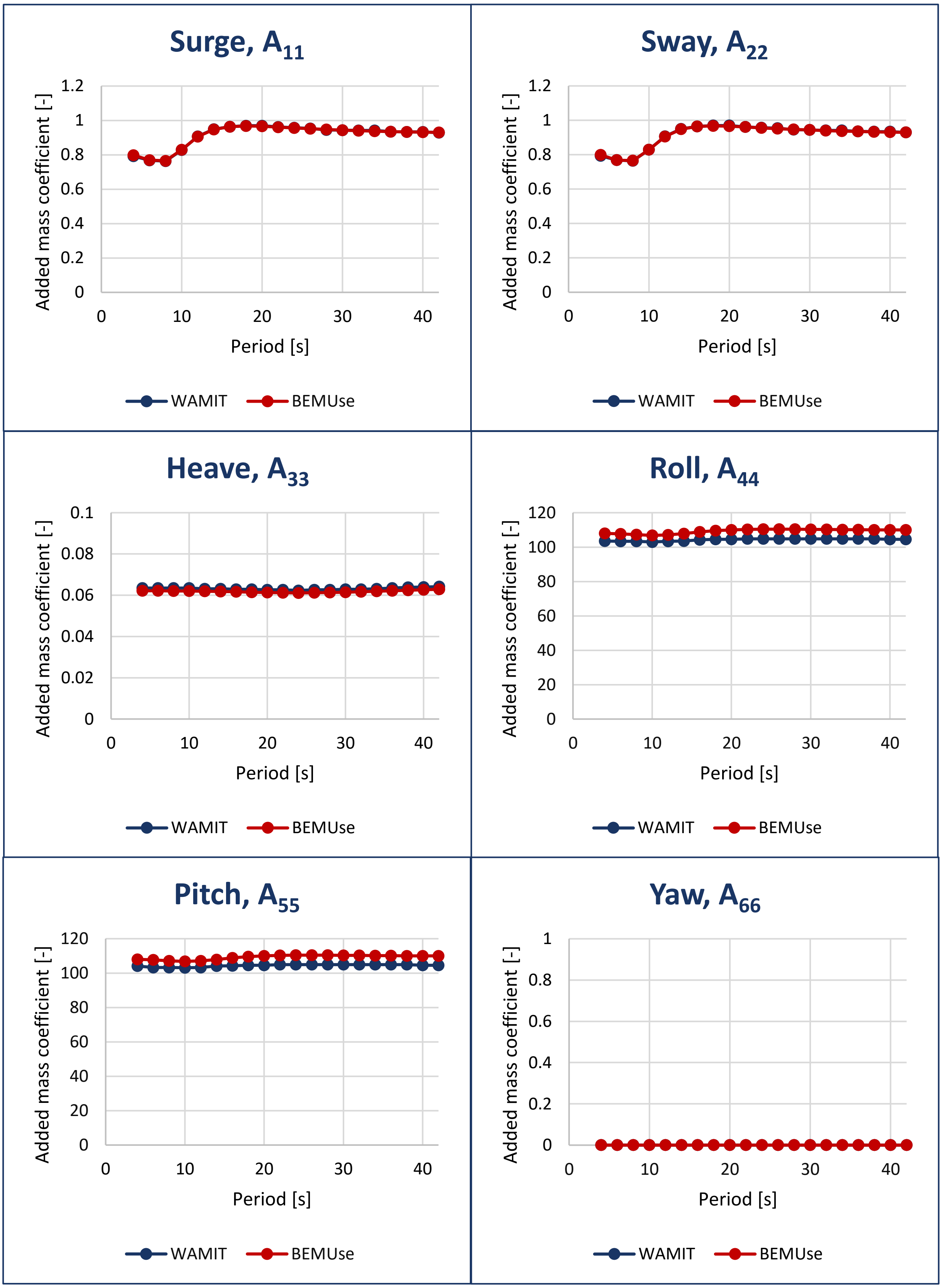

Figure 4.5. Added mass coefficient comparison, cylinder.

4.1.2 Damping

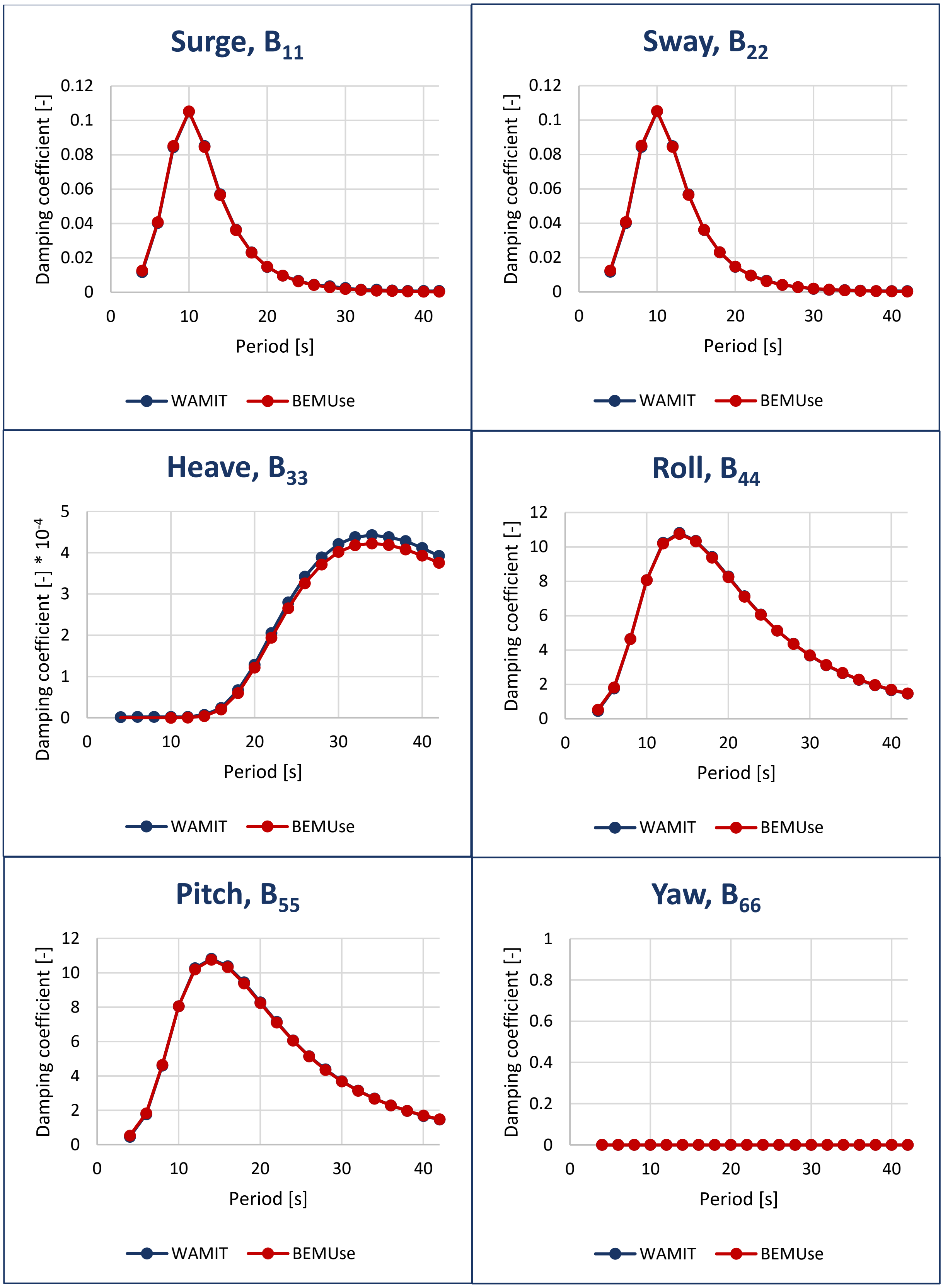

Figure 4.6. Damping coefficient comparison, cylinder.

4.1.3 Exciting forces and moments

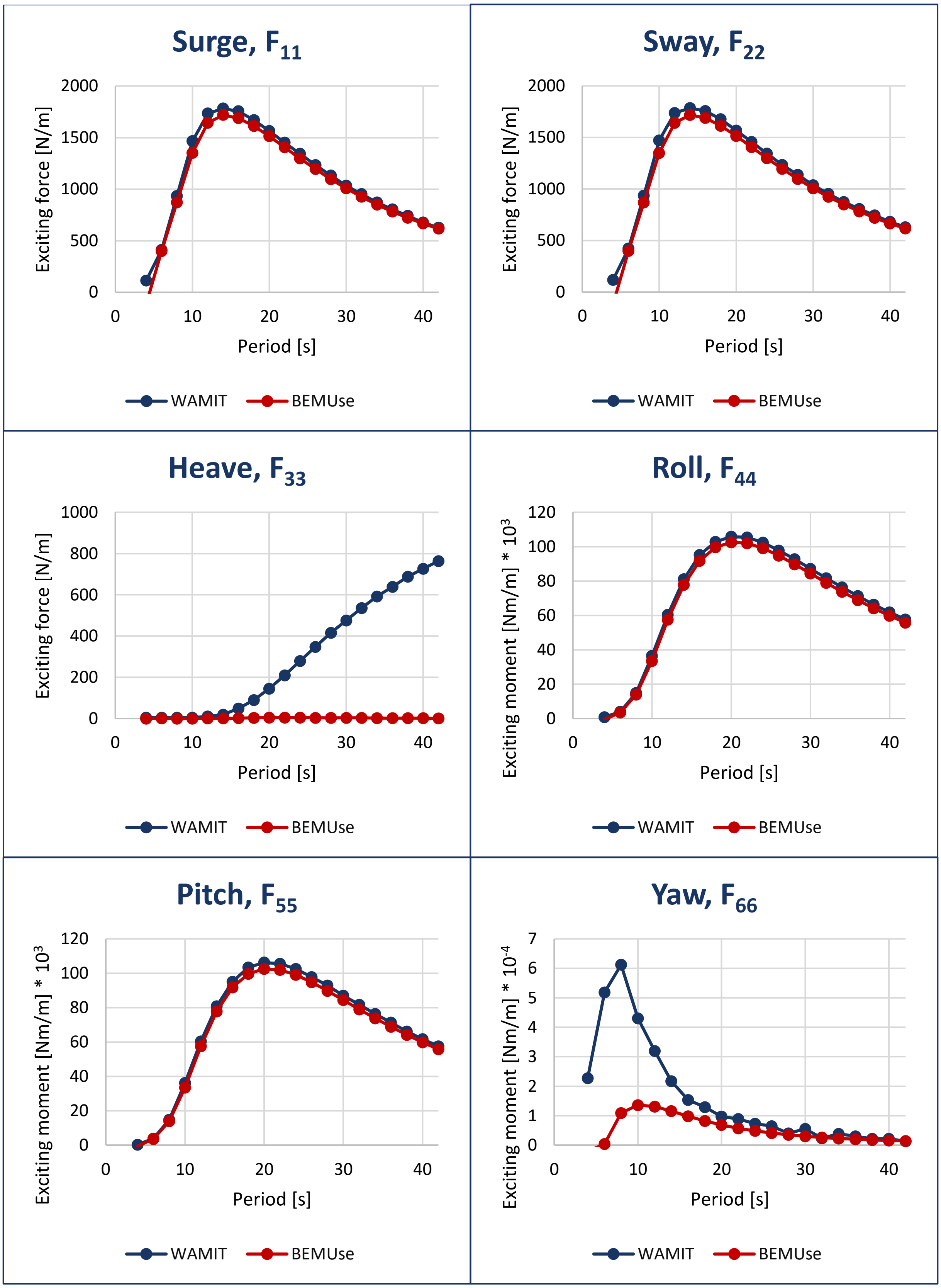

Figure 4.7. Exciting forces and moments comparison, cylinder.

4.1.4 Response Amplitude Operators

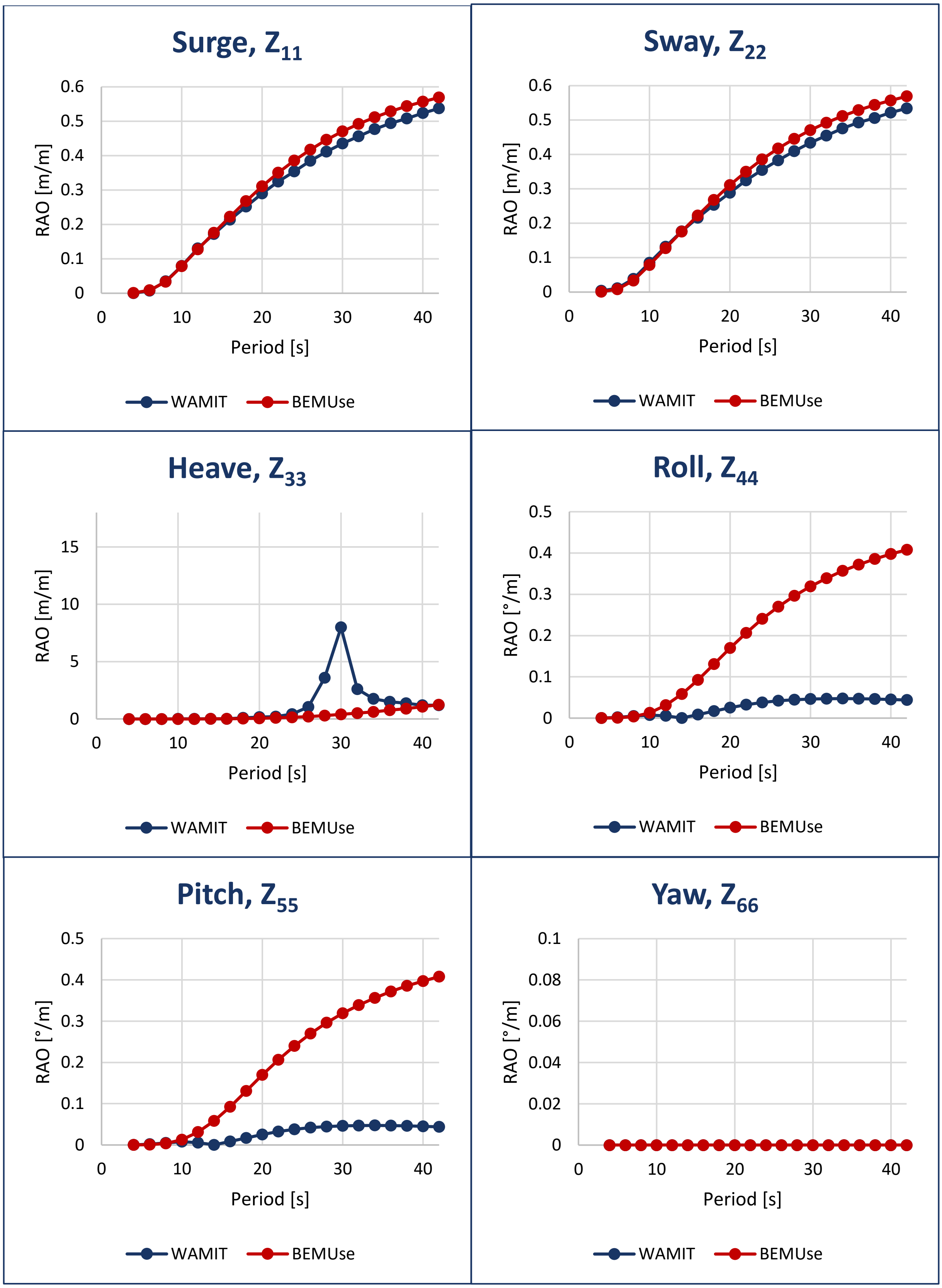

Figure 4.8. RAOs comparison, cylinder.

As shown, the values of almost all the hydrodynamic coefficients are in close accordance with WAMIT results. To get these excellent correspondence, though, the simple normalization according to table (4.2) was often not enough. Thus, a case-by-case summary of the operations performed on the coefficients is considered necessary:

- For added mass, the translational motions were already according excellently after the prescribed normalization, so no further action was needed.
- The rotational motions' added mass coefficient needed to be still divided by a factor 10^2 to agree with WAMIT. This additional normalization can be explained according to formula (3.34a), where for roll, pitch and yaw L's exponent is 5 instead of 3. This also means that for the cylinder $L = 10$.
- For the damping coefficient, the reference paper prescribed the square root of the damping divided by the mass. For surge, heave and sway, though, the square root was not necessary as the results agreed nicely without it.
- The exciting forces in all six motions needed to be divided by an additional factor 10.
- The corrections needed by the RAOs were even more critical, as the translational motions needed to be multiplied by a factor 10^3 and the rotational ones by a factor 10^4. This is probably due to the fact that the reference paper expresses the mass of the cylinder in tons and not in kilograms. Anyways, this only explains the factor 10^3, not the $10^{4.}$

Apart from these additional corrections, there still are some criticalities in the comparison. The exciting force for the heave motion doesn't agree at all with WAMIT and, consequently, neither does the heave's RAO. There are then further problems concerning the RAOs. For roll, pitch, and yaw, no agreement has been found between BEMUse and WAMIT. Another small issue concerns the exciting forces in surge and sway, where the value at $T = 4$ s is negative, which is physically impossible.

Regardless of these flaws, the results for the cylinder and, as reported in the next chapters, for the other geometries, were all more than satisfactory, especially considering the early stage of BEMUse's development.

4.2 BOX

The surface of the parallelepipedal box is discretized with 1264 panels, again using a cosine spacing scheme. To reach that number, the length (in the x-direction) required 32 discrete points, the beam (y-direction) 12, and the draft 10.

Again, the mass of the barge is equal to the displaced volume of water, m = 2.296e+08 kg. The center of mass and buoyancy are again overlapping and in the center of the geometry.

The moments of inertia were calculated using the parallel axis theorem once more to move the axis of rotation from the center of gravity to the center of the surface at the water surface. Therefore

$$I_{xx} = \frac{1}{12}m(B^2 + D^2) + m\left(\frac{D}{2}\right)^2 = 7.35332e + 11\ kg \cdot m^2 \tag{4.3}$$

$$I_{yy} = \frac{1}{12}m(L^2 + D^2) + m\left(\frac{D}{2}\right)^2 = 6.12267e + 08\ kg \cdot m^2 \tag{4.4}$$

$$I_{zz} = \frac{1}{12}m(L^2 + B^2) = 7.95947e + 11\ kg \cdot m^2 \tag{4.5}$$

Where L, B, and D are the length, beam and draft of the barge, respectively.

After the colorized figure below, the four coefficients calculated for the six motions are reported.

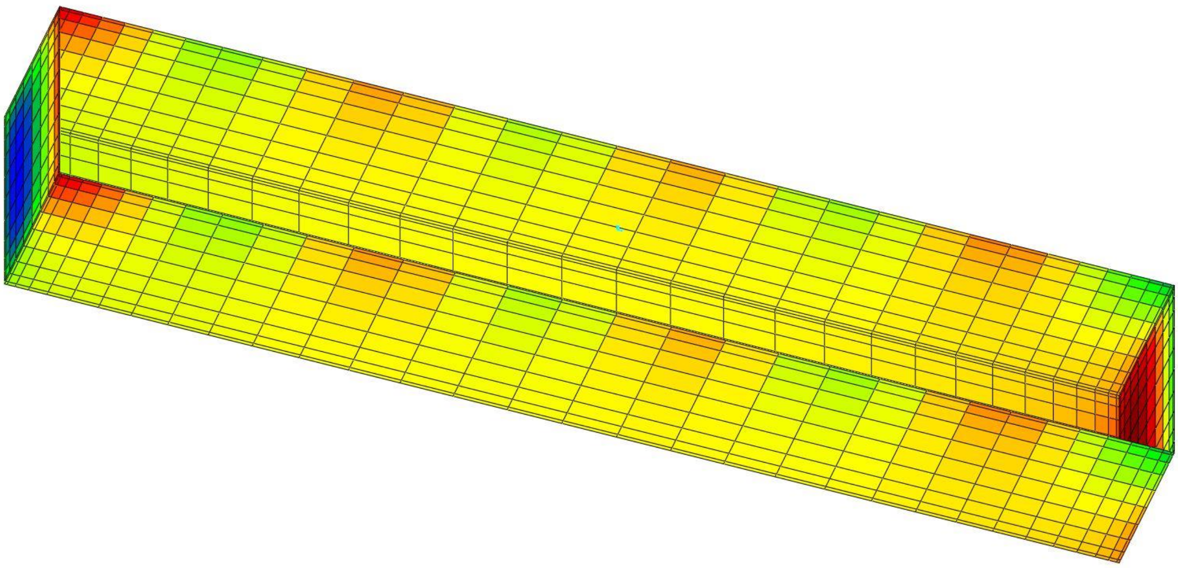

Figure 4.9. Box with colorized panels, generated by BEMUse.

4.2.1 Added mass

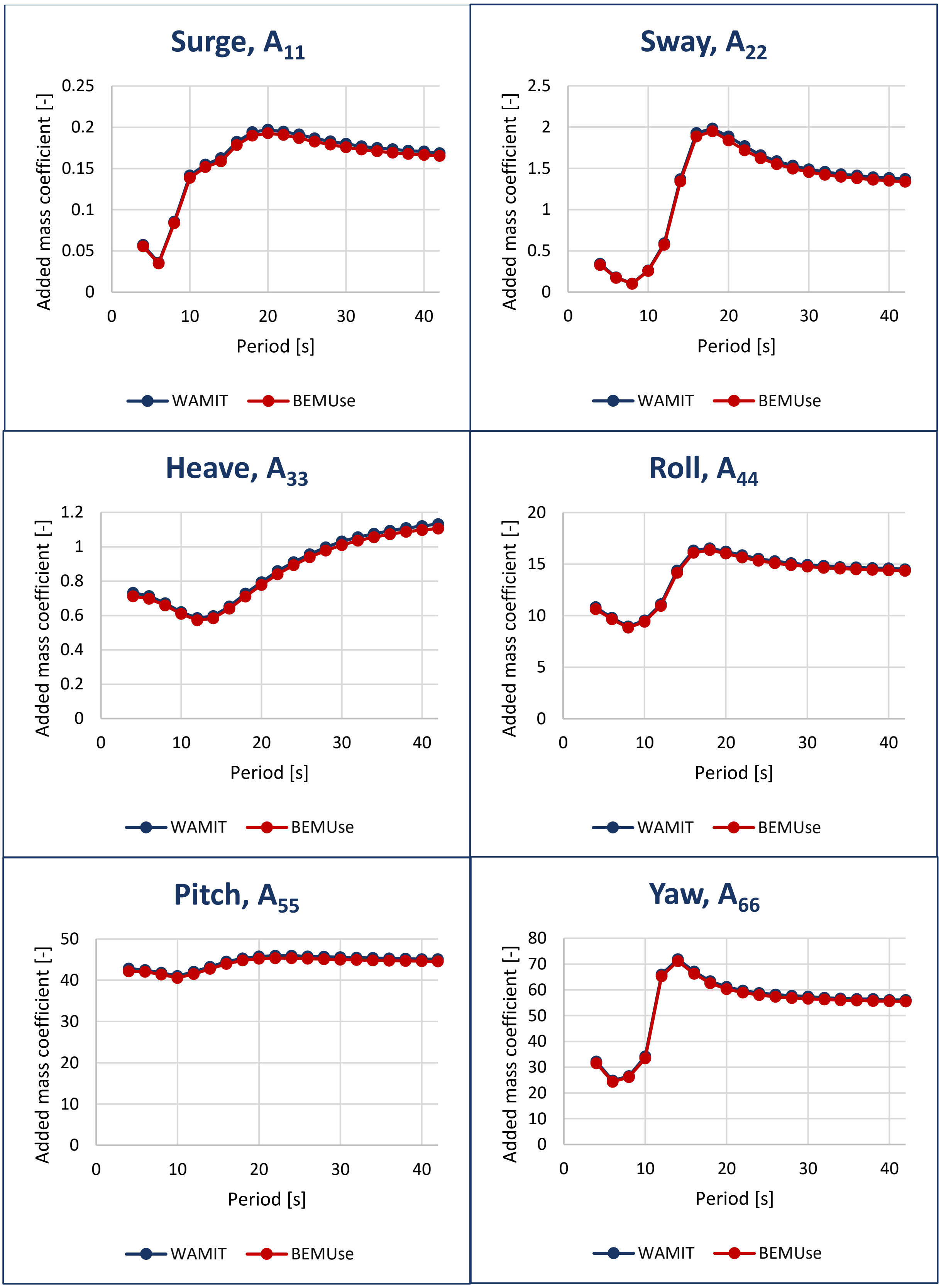

Figure 4.10. Added mass coefficient comparison, box.

4.2.2 Damping

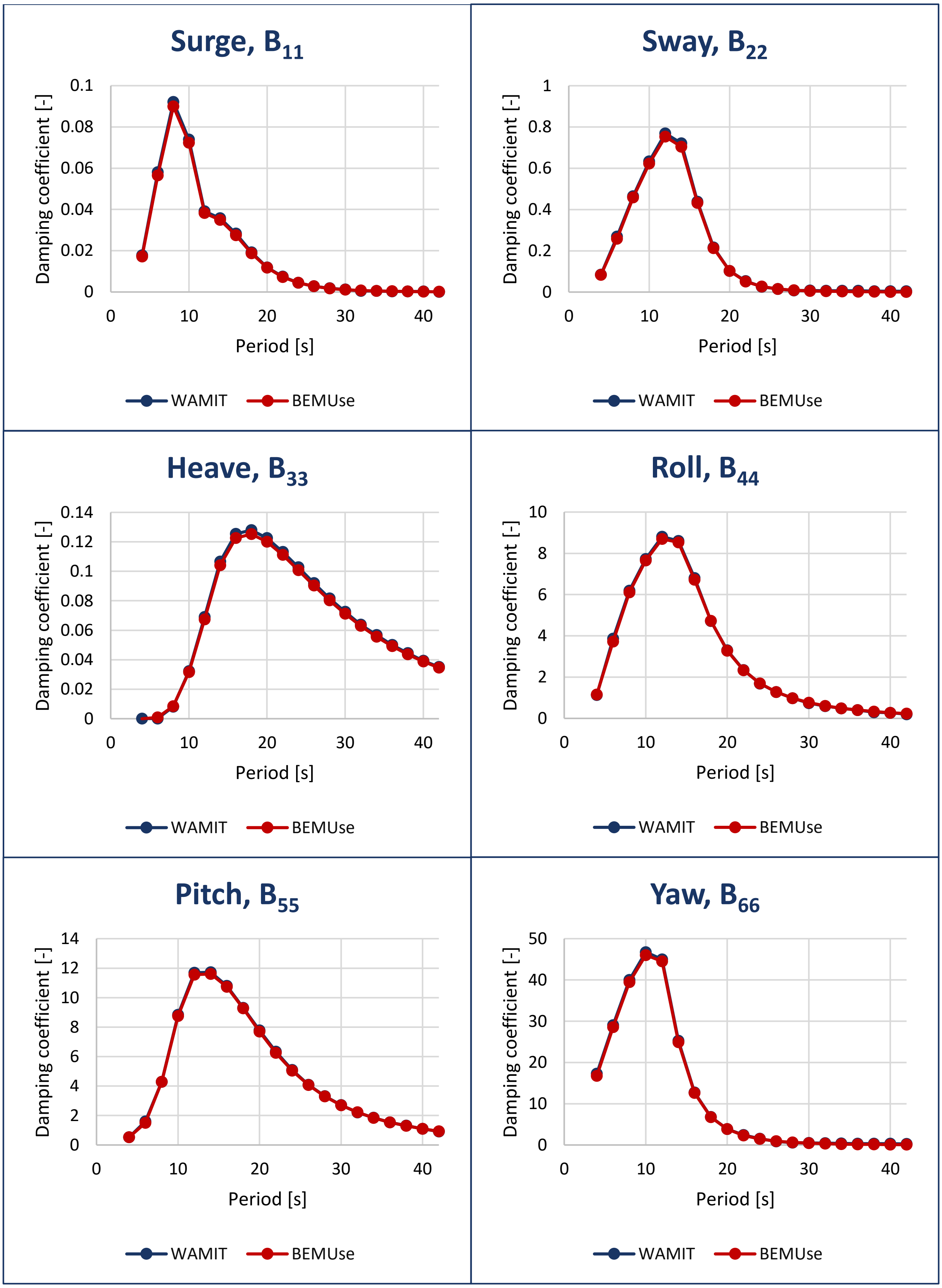

Figure 4.11. Damping coefficient comparison, box.

4.2.3 Exciting forces and moments

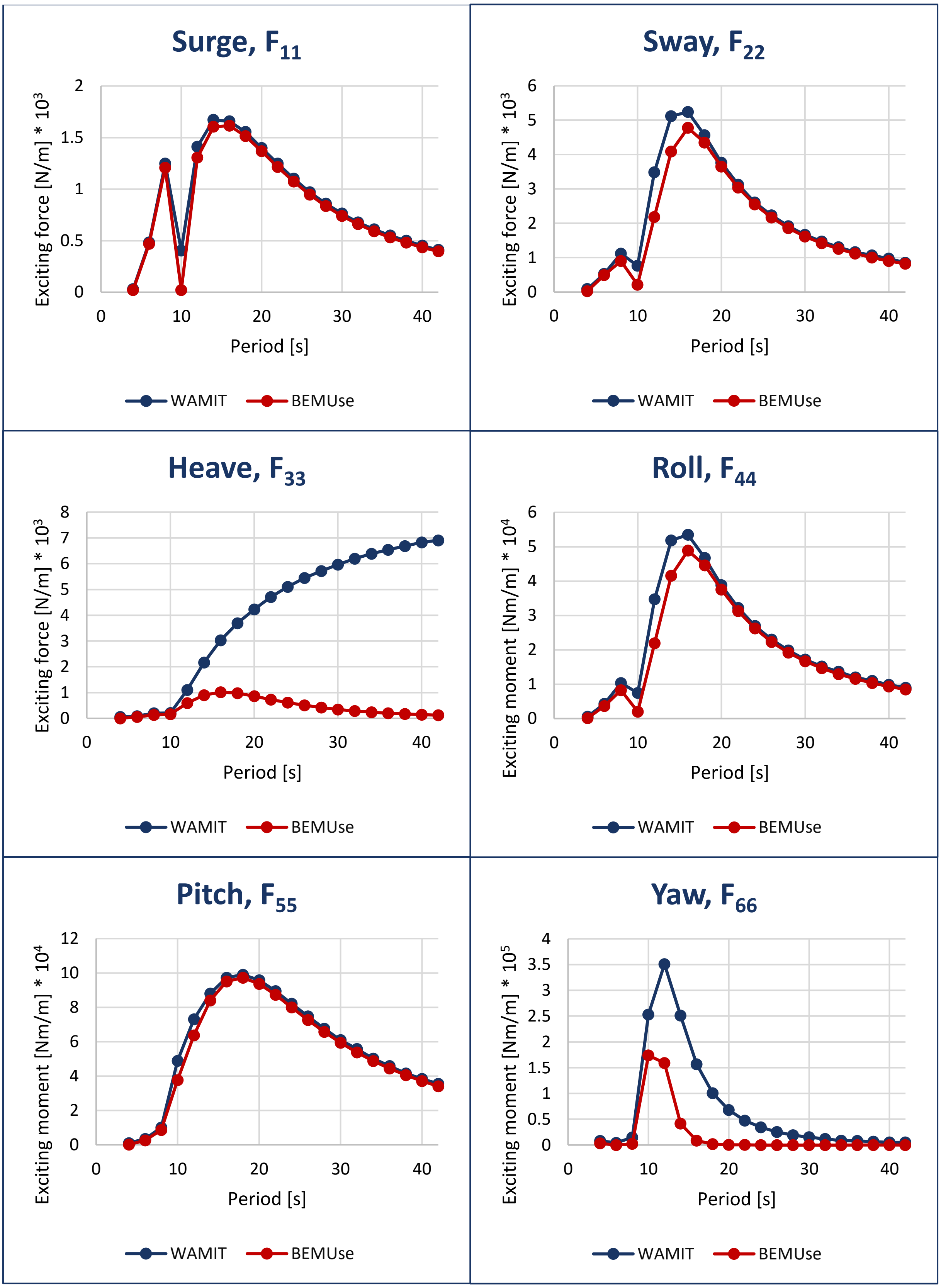

Figure 4.12. Exciting forces and moments comparison, box.

4.2.4 Response Amplitude Operators

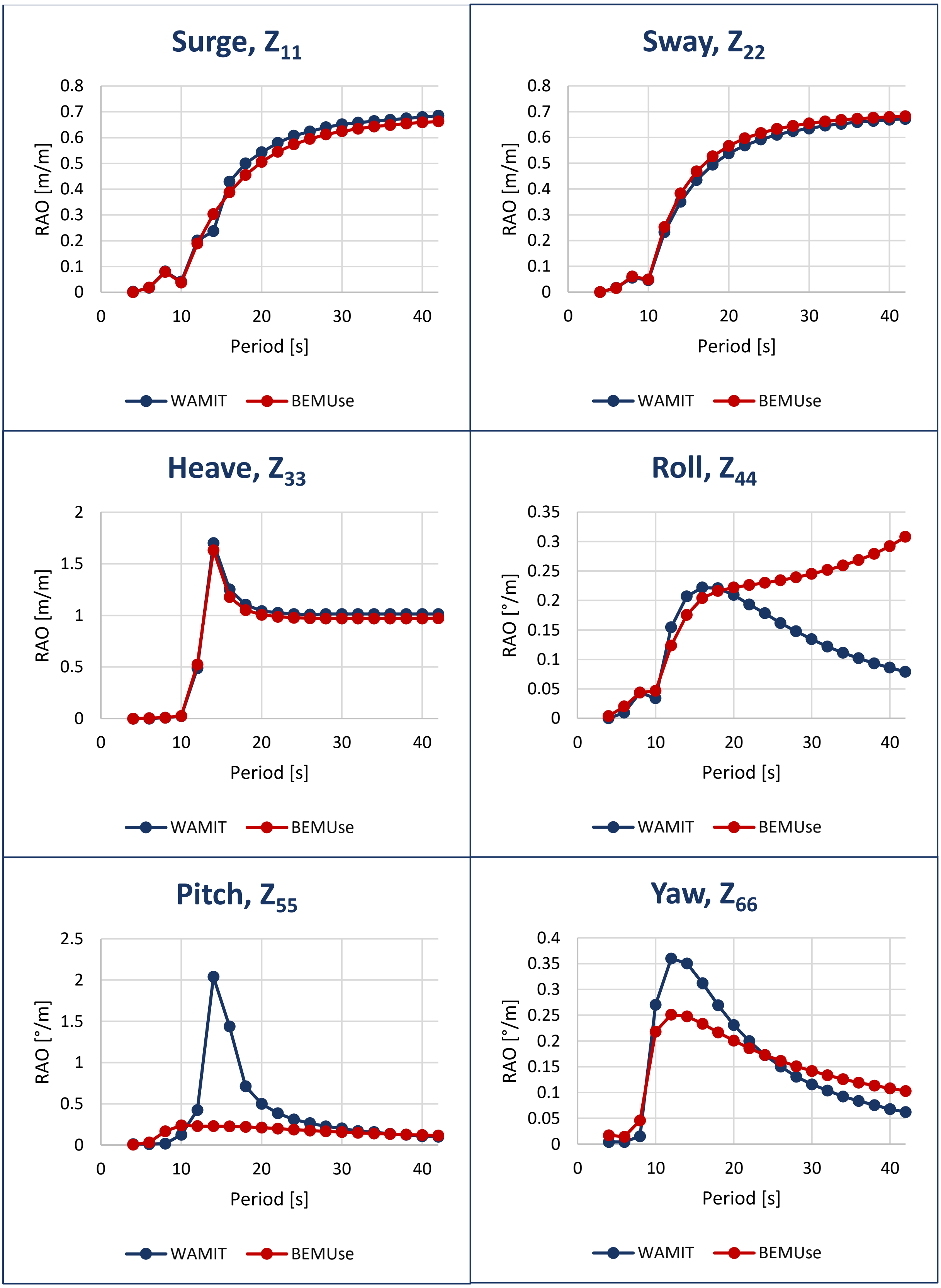

Figure 4.13. RAOs comparison, box.

As for the cylinder, some additional corrections had to be done on the normalization prescribed by the paper of reference. To make things worse, these other operations were, in some cases, different from the ones done in the cylinder test case. Here's what has been done:

- Added mass coefficients agree for surge, sway and heave. Meanwhile, to make roll, pitch and yaw agree, the square root of the expected normalization needs to be used.
- On the contrary, for damping the rotational motions were agreeing as expected, while the translational modes didn't need the square root, which was therefore removed.
- To make the exciting forces agree, not only had the result to be yet again divided by a factor 10, but due to some problems with the sign, the absolute value was needed. These corrections were common to all the degrees of motion.
- For the RAOs, like in the case of the cylinder surge, sway and heave needed to be multiplied by a factor 10^3, while roll, pitch and yaw by 10^4. The explanation for that is the same as for the cylinder.

Again, not all the coefficients agree with WAMIT. Like in the previous test case, the most significant issues concern exciting forces and RAOs, but it's worth noting how the RAO for heave agrees much better for the box than for the cylinder. This is a direct consequence of a closer agreement between the exciting forces. The biggest issues remain the RAOs for the rotational motions, which don't agree at all.

4.3 TENSION LEG PLATFORM

Of particular interest for the industry of FOWTs is the third test case, the ISSC tension leg platform, as it is one of the most promising designs for floating platforms in wind power applications. The complete geometry of the ISSC is shown in the figure below, taken from Eatock Taylor and Jefferys (1986) [31].

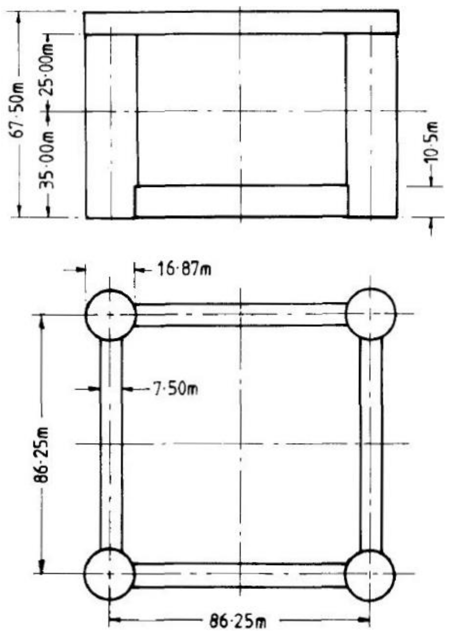

Figure 4.14. The geometry of the Tension Leg Platform.

The graphical representation on BEMUse, shown in figure (4.3), is different because only the section below the water surface is considered. In the same publication, there is also a table reporting all the physical and geometrical parameters of the TLP.

Parameter	Value
Spacing between column centers	86.25 m
Column radius	8.44 m
Pontoon width	7.50 m
Pontoon height	10.50 m
Draft	35.00 m
Displacement	54.5 x 10^6 kg
Weight	40.5 x 10^6 kg
Roll moment of inertia	82.37 x 10^9 $kg \cdot m^2$
Pitch moment of inertia	82.37 x 10^9 $kg \cdot m^2$
Yaw moment of inertia	98.07 x 10^9 $kg \cdot m^2$
Vertical position of CoG above keel	38.00 m

Table 4.3. Geometrical and physical properties of the TLP.

Interestingly, for these simulations the center of mass, which coincides again with the center of buoyancy, is located in the center of the geometry 38 m above the bottom of the keel, which means above the water level. The platform weights $40.5e + 6\ kg$, with a displacement of $54.5e + 6\ kg$. The moments of inertia are, respectively, $I_{xx} = I_{yy} = 82.37e + 9\ kg \cdot m^2$ and $I_{zz} = 98.07e + 9\ kg \cdot m^2$.

Because of slight differences in the method for creating the panels, their exact number couldn't be replied. However, 520 instead of 512 were used, which assures a close similarity between the simulations. In the figure below, the colorized geometry as generated by BEMUse is reported, followed once again by the complete comparison of coefficients.

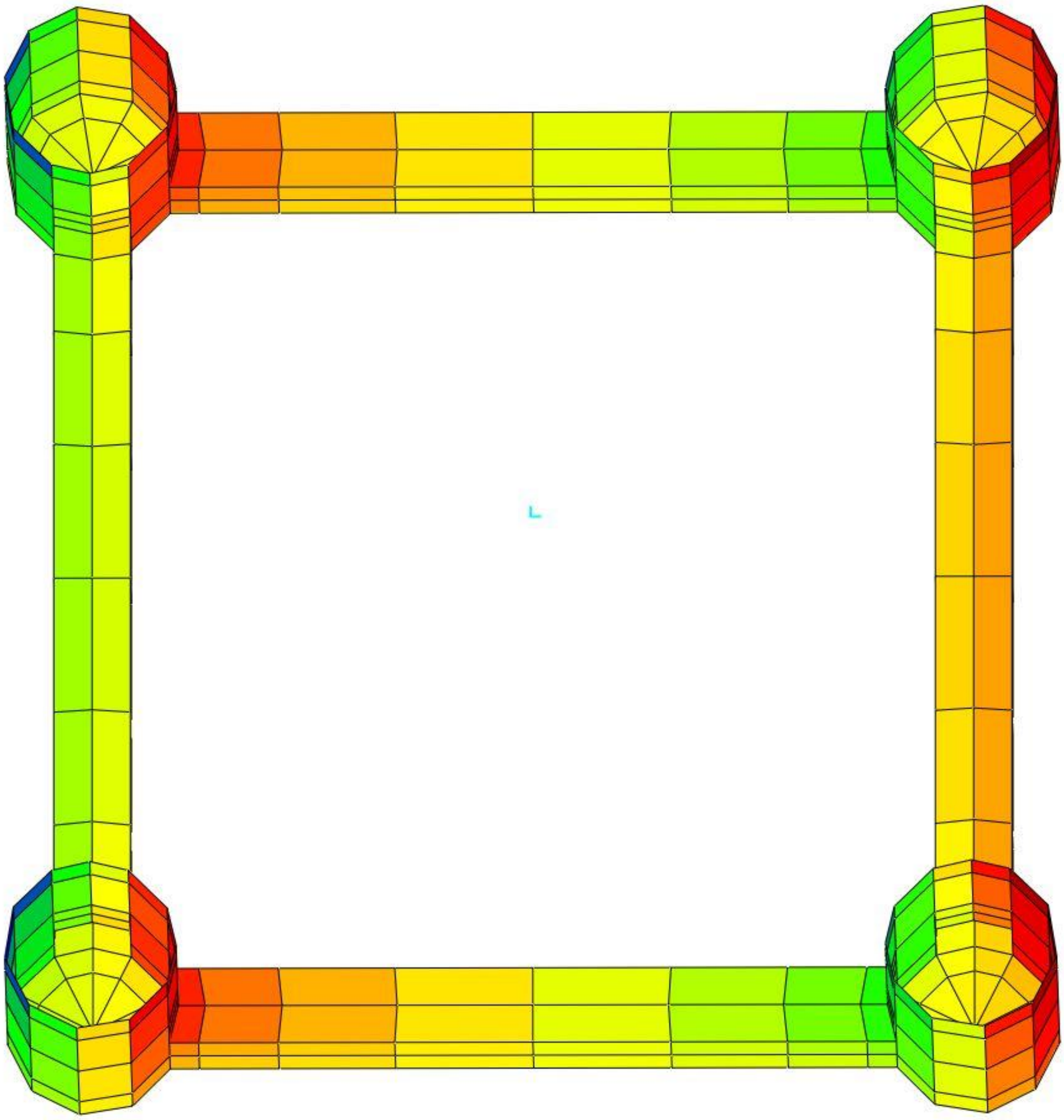

Figure 4.15 TLP with colorized panels, generated by BEMUse.

4.3.1 Added mass

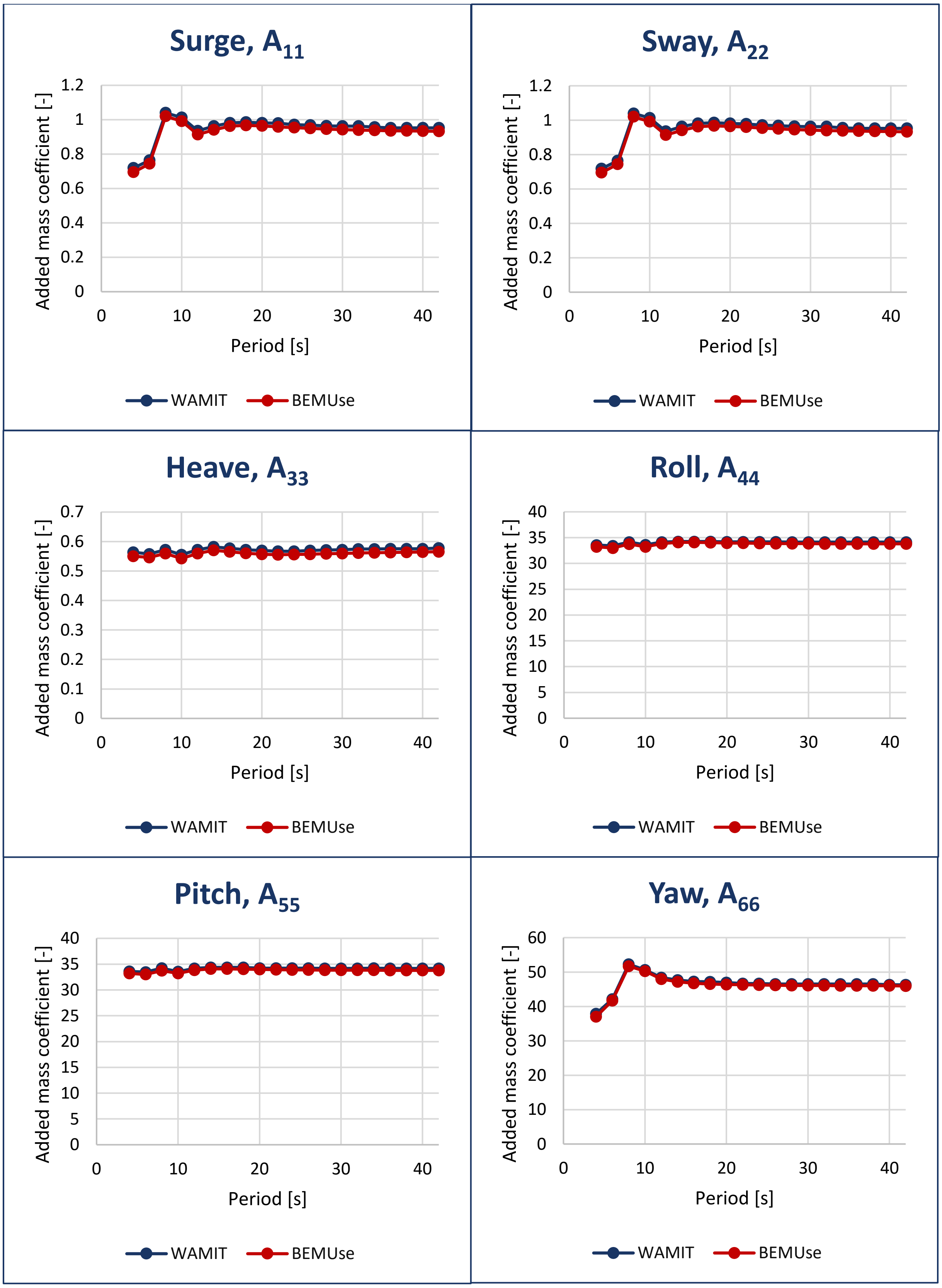

Figure 4.16. Added mass coefficient comparison, TLP.

4.3.2 Damping

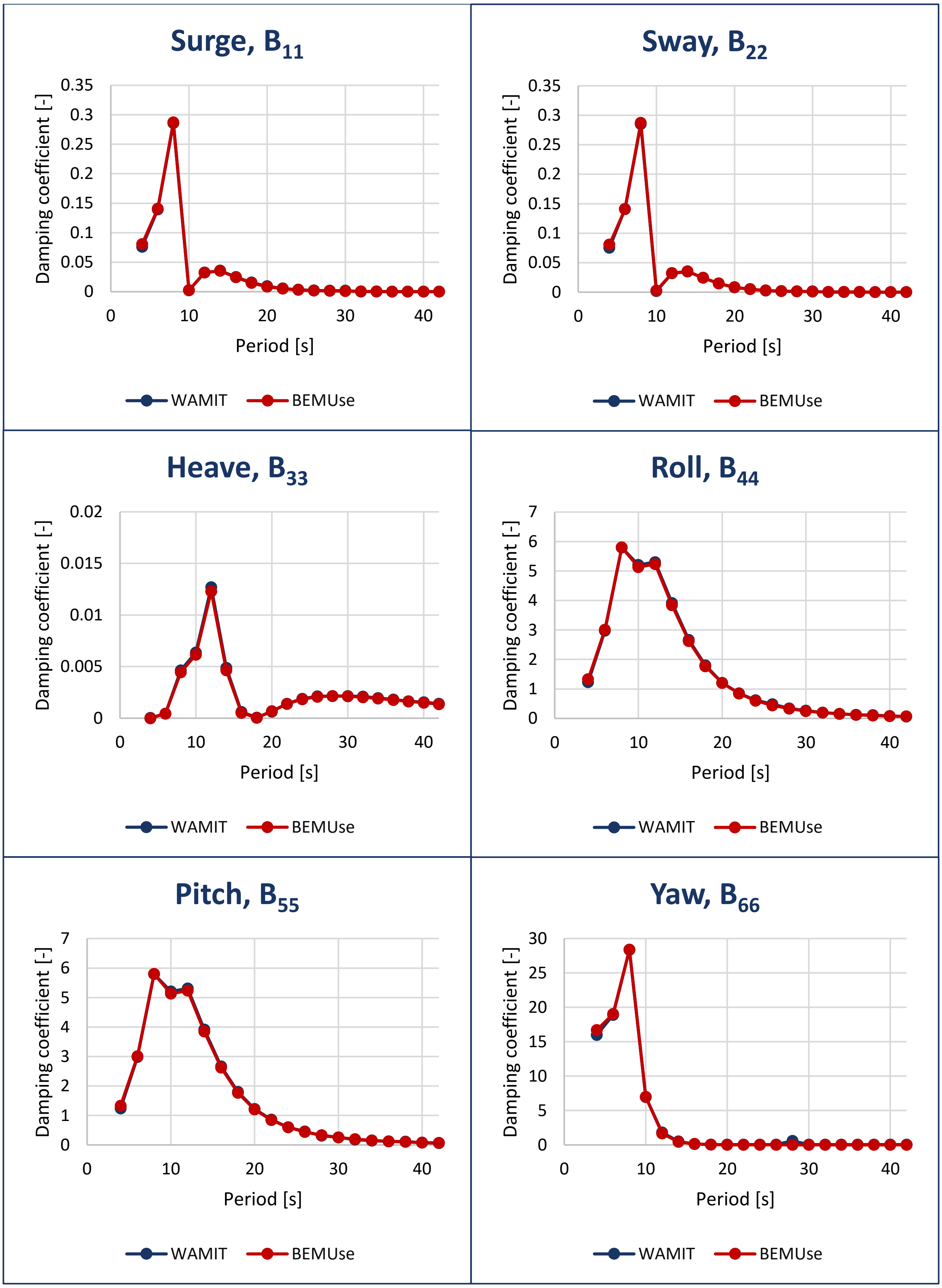

Figure 4.17. Damping coefficient comparison, TLP.

4.3.3 Exciting forces and moments

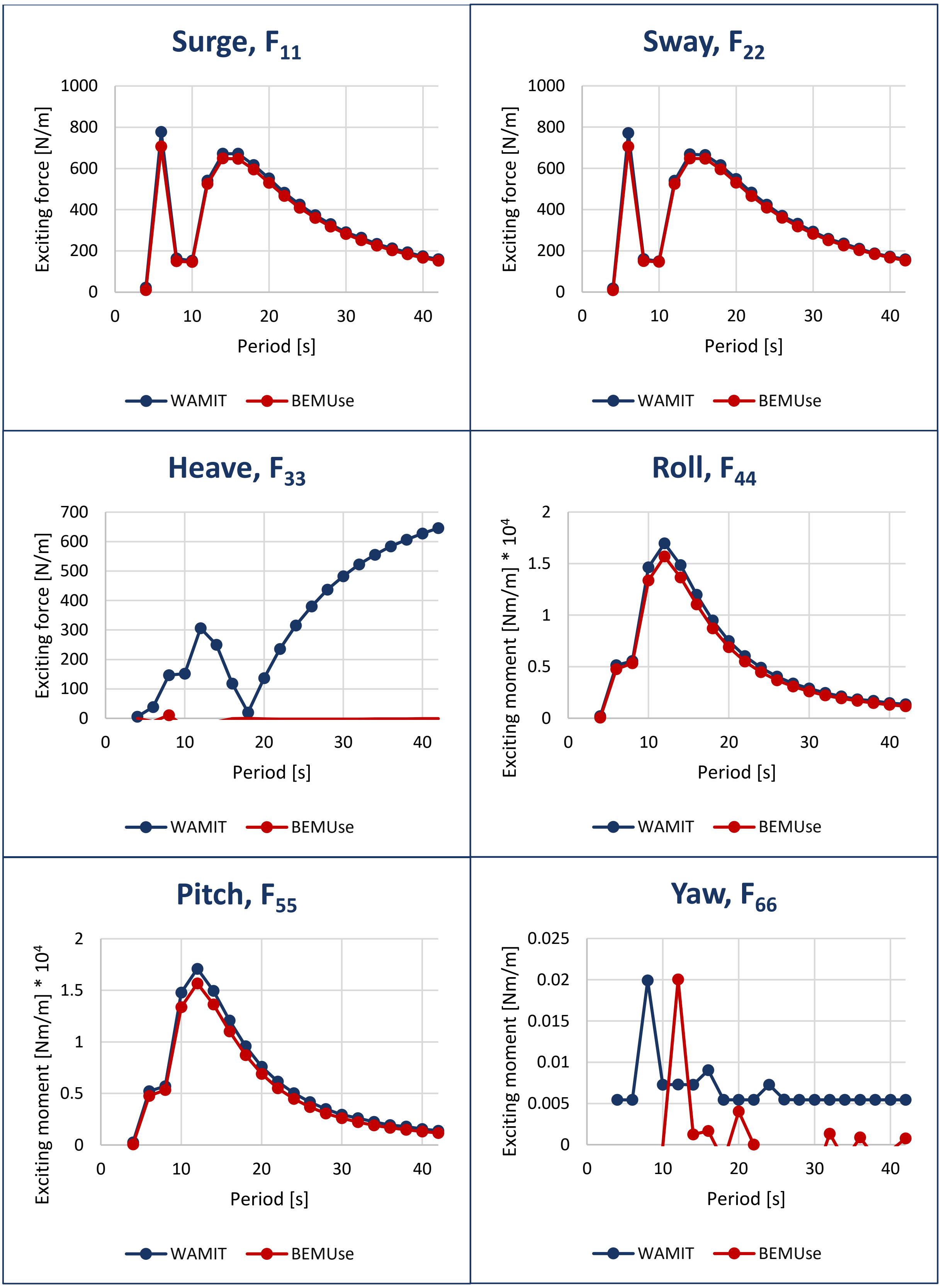

Figure 4.18. Exciting forces and moments comparison, TLP.

4.3.4 Response Amplitude Operators

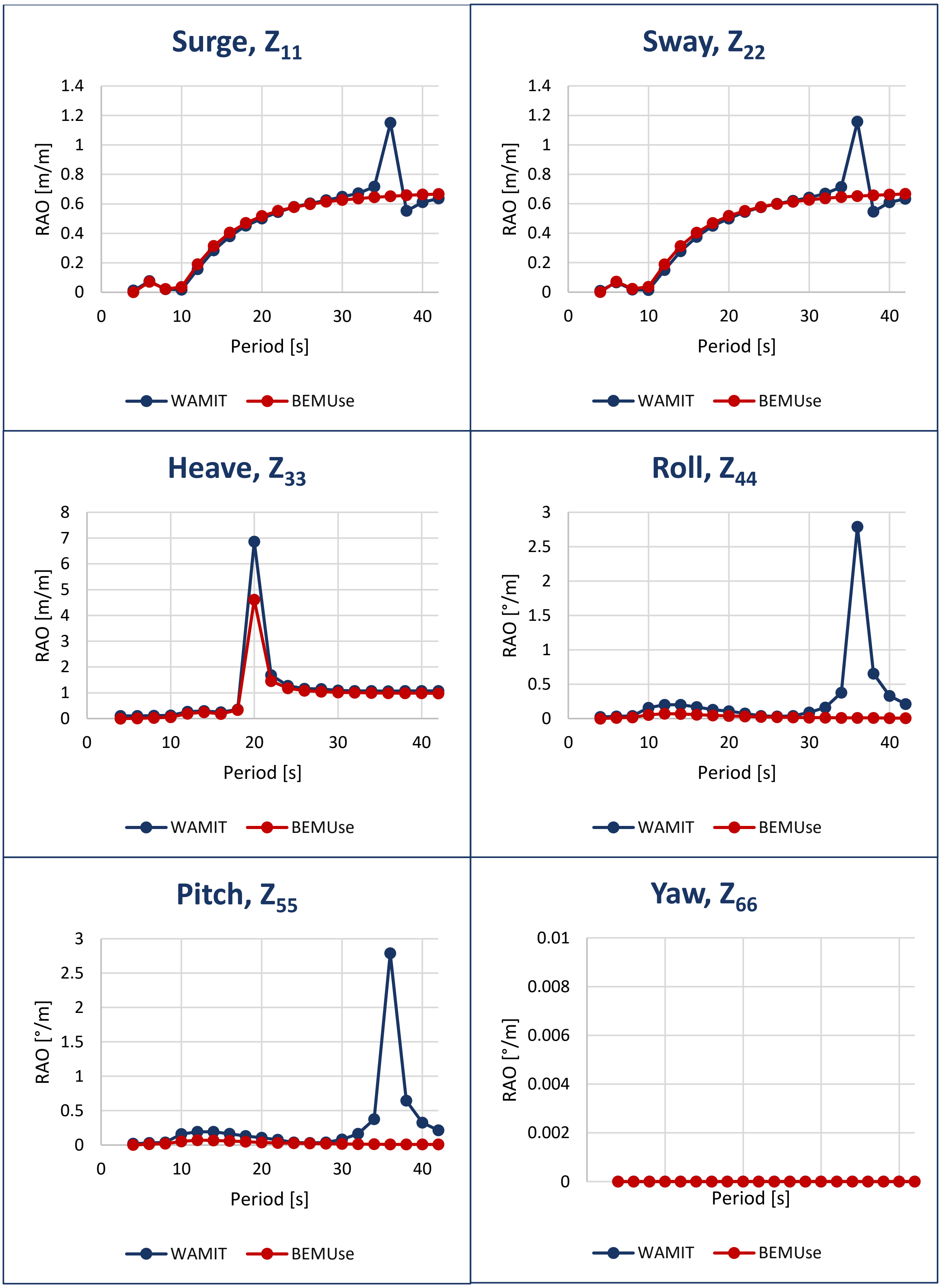

Figure 4.19. RAOs comparison, TLP.

Again, some modifications with respect to the original normalization were needed:

- As for the box, the added mass coefficient for the rotational motions agrees only if the square root is calculated on the ratio of added mass and the mass of the body
- Again, for the damping coefficient the translational motions do not need the square root, while roll, pitch and yaw do.
- The values of the exciting force need to be divided by ten for all 6 degrees of motion.
- As for the other two test cases, the translational RAOs need to be further multiplied by 10^3, 10^4 for the rotational ones.

Similarly to the other two geometries, the added mass and damping coefficients agree almost perfectly between BEMUse and WAMIT, and so do the exciting forces except for the heave motion. Some issues arise with the RAOs, as the peaks seen for surge and sway at period $T = 36\ s$ in the WAMIT simulation cannot be found in BEMUse. Like for the box, there is good accordance for the heave, while no similarity can be seen for roll, pitch and yaw.

Summarizing, for all three geometries the added mass and damping coefficients calculated by BEMUse coincide almost perfectly with the results given by WAMIT. There were indeed some additional operations to do on the values to make them agree, but since the authors of the paper used as reference do not clearly explain all the steps followed for their study, it is difficult to know why these operations are needed. The agreement between the two softwares is excellent also for the exciting forces, with the notable exception of the heave motion. The RAO for surge and sway also agree beautifully, while the other motions are flawed with errors that was not possible identify.

Overall, also given that BEMUse is a relatively new software and this validation is the first test of such kind carried on the model, the results obtained are considered more than satisfying.

After the comparison with WAMIT, another range of case-studies was considered useful to increase BEMUse's trustworthiness further. Therefore, using another well-affirmed hydrodynamic analysis software like Ansys AQWA, a new set of experiments was carried out. The results are contained in the next chapter.

5. AQWA COMPARISON

Considering how extensively Ansys is used in engineering, having BEMUse's result to agree with AQWA's would be of great importance. Therefore, various test cases were studied.

This software has its 3D-CAD with an excellent GUI, with which it's relatively easy to generate the desired geometry. After creating the body surface, physical parameters need to be added. After that, the program automatically generates the quadrilateral panels; the user cannot control this process, and therefore the number of panels on the body will be different from the one in BEMUse. Besides, the meshing is generated with a different process, as shown in the figure below. Unlike what happened with WAMIT, the results calculated by AQWA are not normalized.

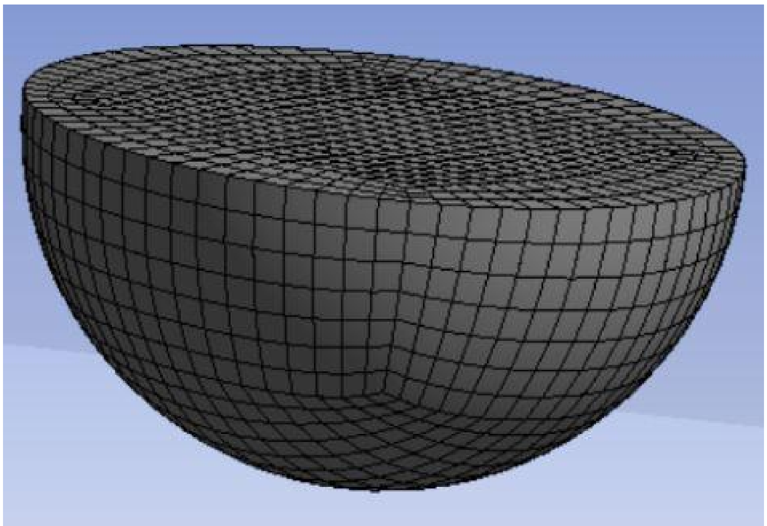

Figure 5.1. The mesh generated by AQWA is completely different with respect to BEMUse's.

These differences cannot be avoided and could be the cause of slight differences in the results.

5.1 HEMISPHERE

The first case-study analyzed is a simple hemisphere with a 1 m radius. This geometry is not of practical interest, but it has the great advantage of also having an analytical solution that can be used to check the accuracy of the analysis. For the hemisphere, a new set of angular frequencies ω has been chosen, going from 0 to $10 \cdot g\ rad/s$, where g is gravity. This is because, for such a small geometry, these values of ω are the most meaningful to study.

The results of the two softwares for the hemispherical body shown in figure (3.1) agree nicely once again.

5.1.1 Added mass

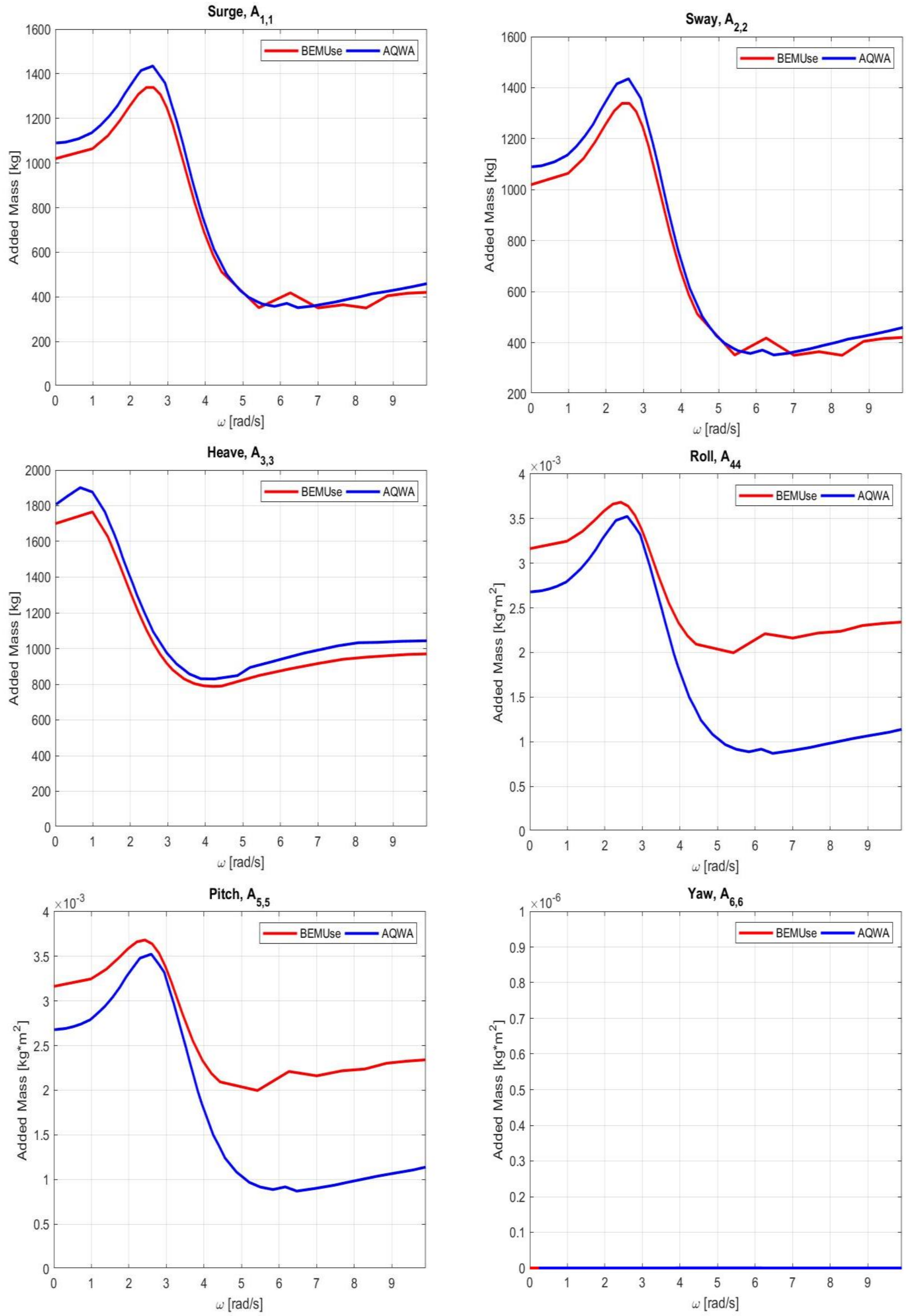

Figure 5.2. Added mass comparison, hemisphere.

5.1.2 Damping

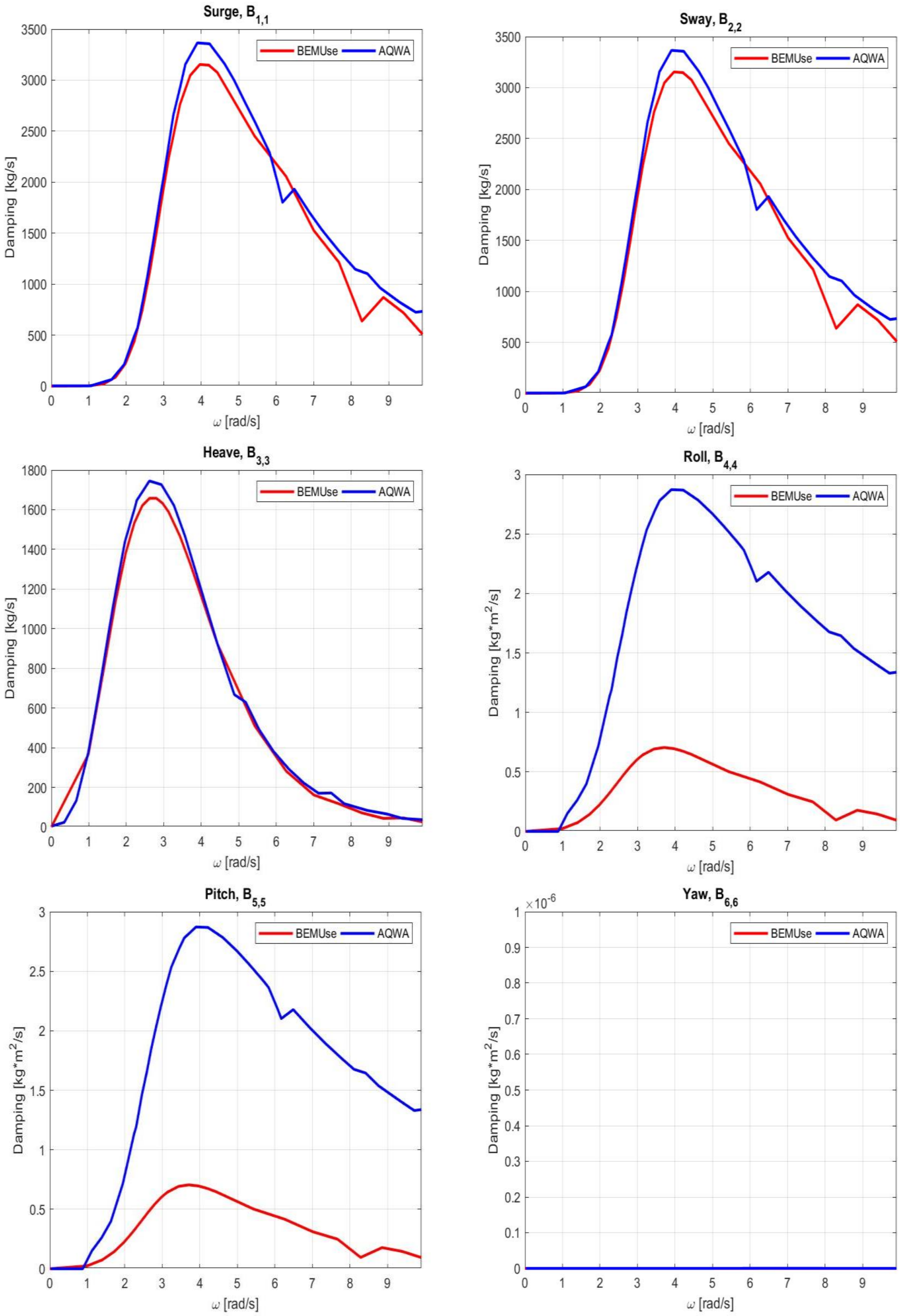

Figure 5.3. Damping comparison, hemisphere.

5.1.3 Exciting forces and moments

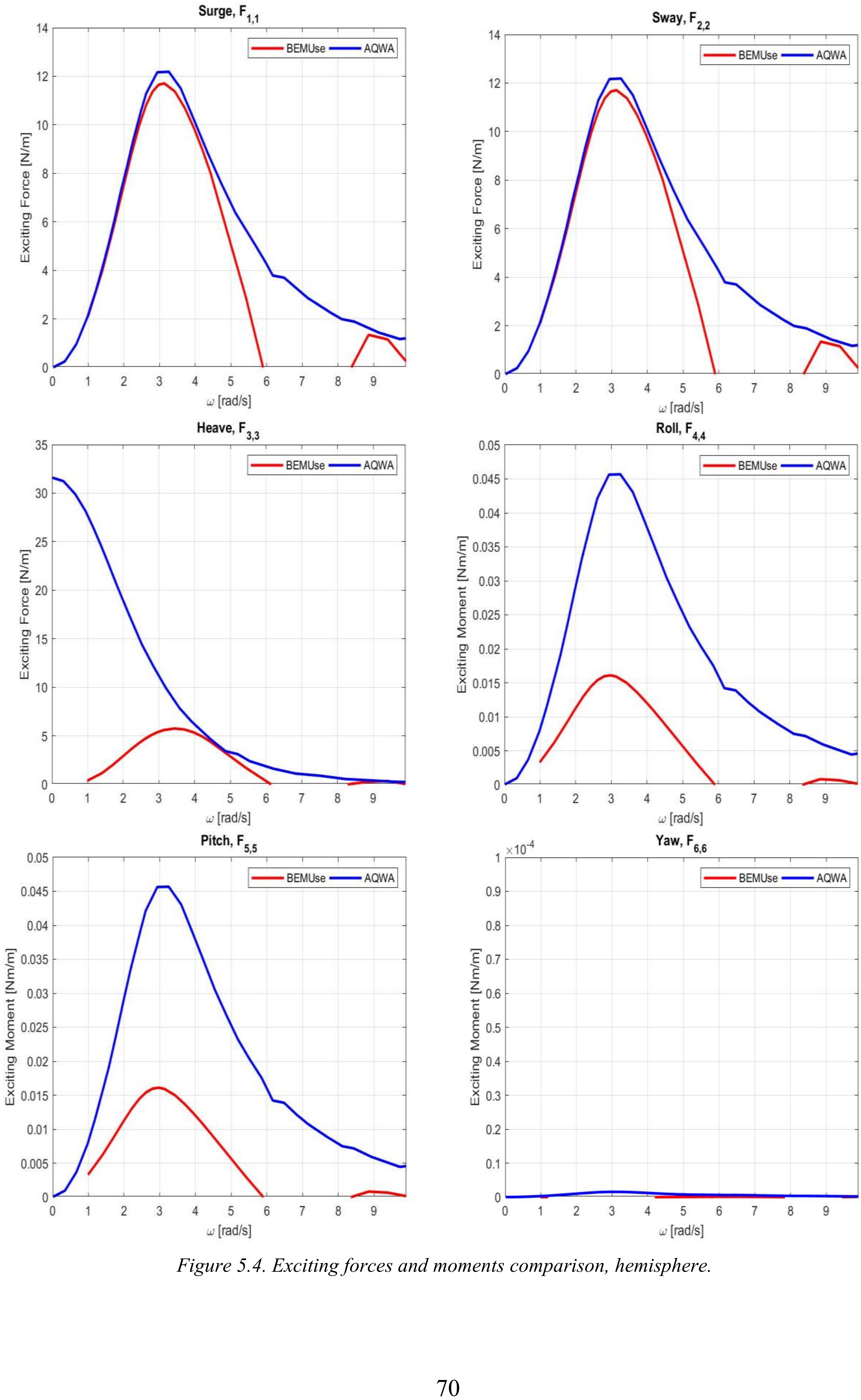

Figure 5.4. Exciting forces and moments comparison, hemisphere.

5.1.4 Response Amplitude Operators

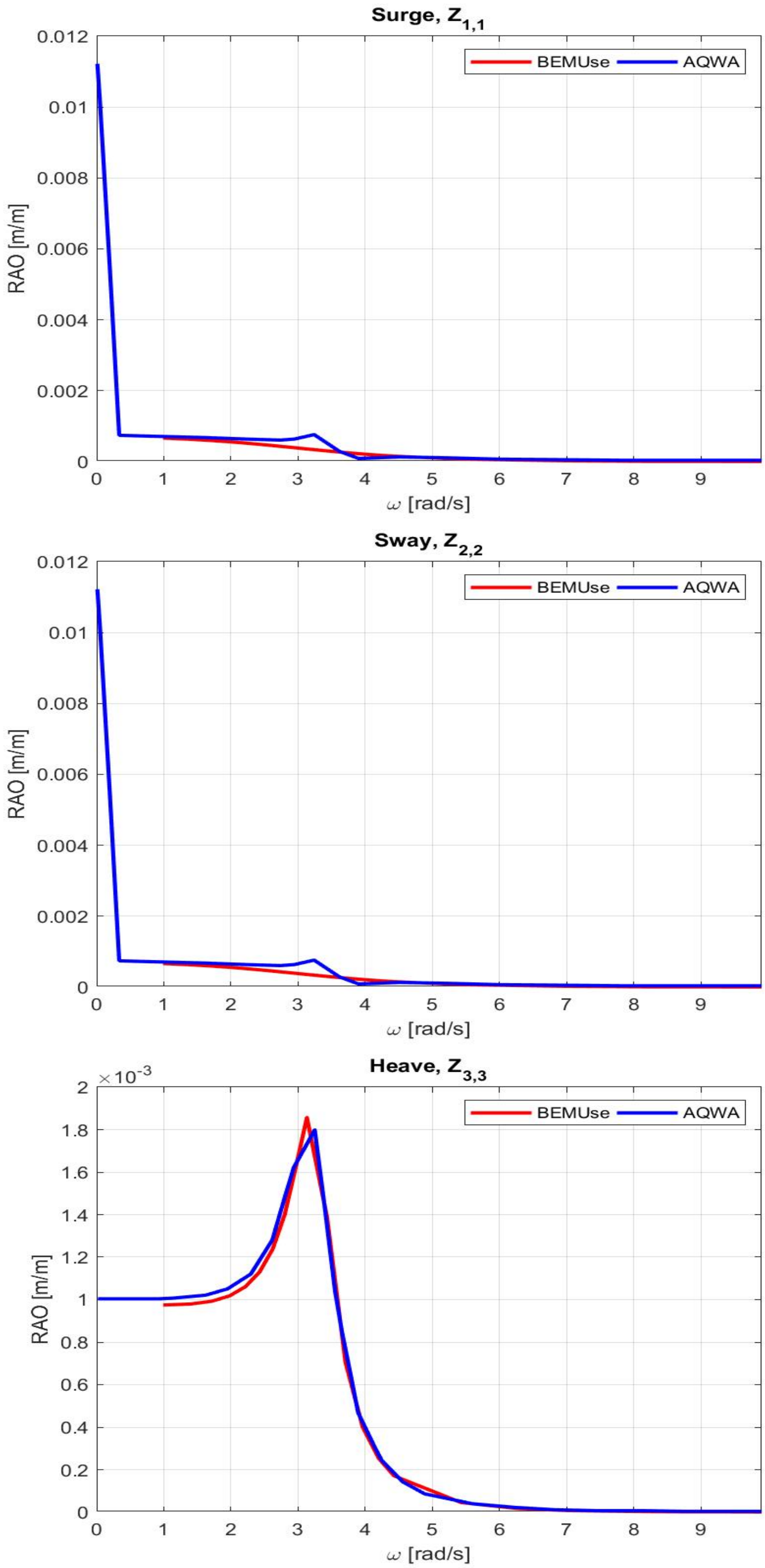

Figure 5.5. RAOs comparison, hemisphere.

For added mass, as hoped, the curves both agree with the analytical solution quite accurately, especially for surge, sway and heave. The rotational motions show some similarities in the shape of the curves, although the peaks and lows occur at different frequencies and the numerical values have varying distances between the two softwares.

Also for damping the results are fitting, as the translational motions agree almost perfectly, except for some unexpected irregularities in both curves, occurring at different frequencies. These are probably due to an imperfect irregular frequency removal procedure. The situation is different for the rotational motions, as the curves have a similar shape but do not coincide. This is probably a dimensional problem, as the values in AQWA were probably multiplied by a factor which was not possible to identify in this comparison.

For the exciting forces, the situation is quite different, as the curves show some similarities, but the comparison can only be deemed unsatisfactory for all directions of motion. The main issue here is that, apart from the evident differences in shape, the curves generated by BEMUse all reach negative values at some point in the plot, which is physically impossible.

The RAOs are again quite similar between the two softwares, but only the translational motions have been compared. The peak is visible in the plots at $\omega = 0\, rad/s$ for AQWA's curve is absent in BEMUse's because the analysis of the value 0 does not give a result there, so the first point evaluated was at $\omega = 1\, rad/s$. This is because the comparison with WAMIT has already shown there is something wrong in BEMUse with roll, pitch and yaw. Moreover, as the RAOs are calculated starting from the other three parameters, it has been considered meaningless to carry out this last comparison given the issues encountered previously, especially with the exciting moments.

Having proven that the two softwares give similar results, more complex geometries can be confidently analyzed.

5.3 CYLINDER

The next case-study is the same cylinder analyzed in the comparison with WAMIT. This choice was made first of all because comparing the three softwares on the same body is of high interest, and then because a cylinder that big is an excellent intermediate step between a pure geometrical test case and a commercial scale FOWT's platform, which will be examined in the next simulation.

For this simulation and the next the incoming waves had 20 different angular frequencies, going from $T = 4\ s$ to $T = 42\ s$, exactly like for the WAMIT comparison.

The same physical parameters as before (mass, moments of inertia, coordinated of the CoG) were set as input, and the results are shown in the next plots.

5.2.1 Added mass

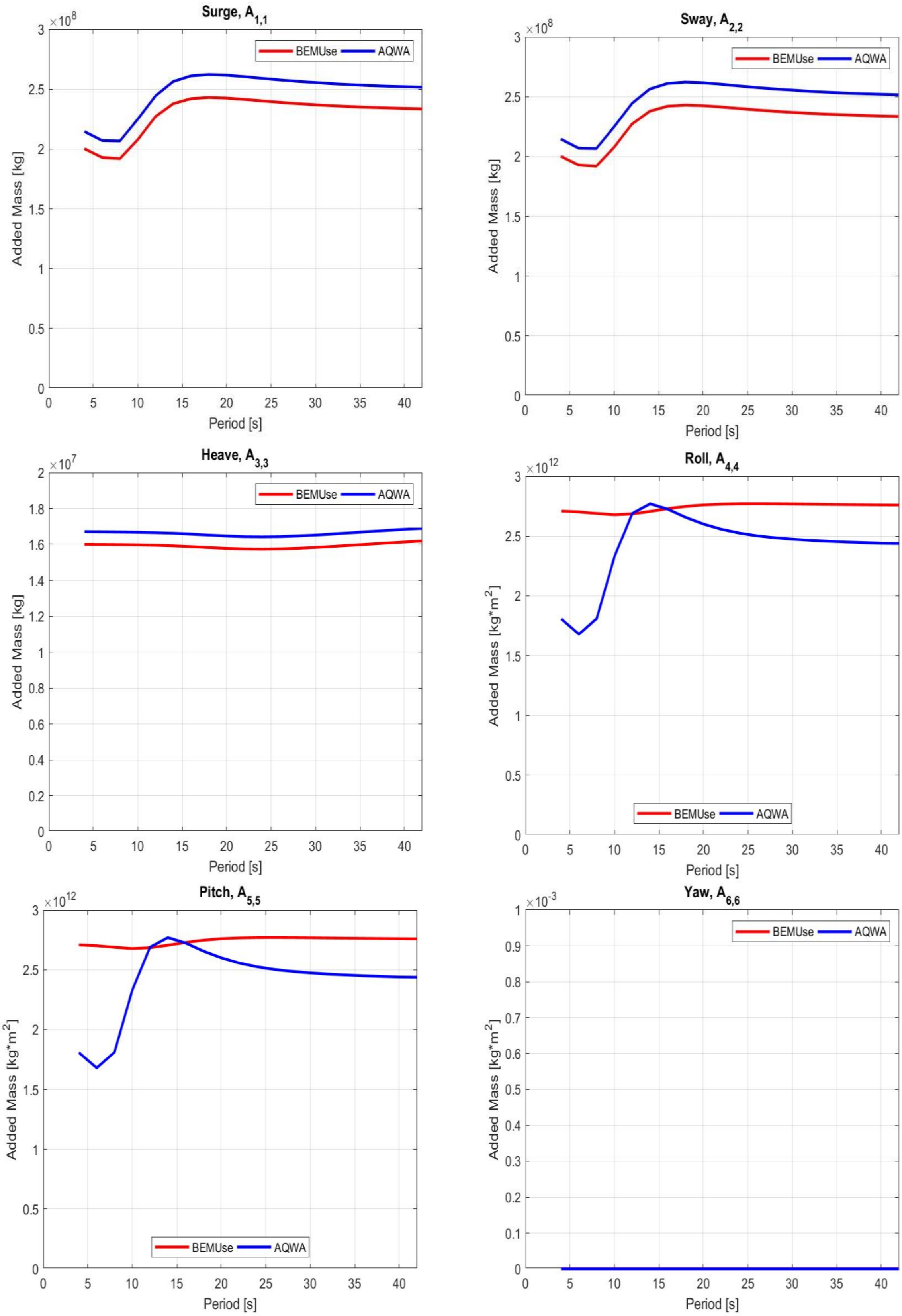

Figure 5.6. Added mass comparison, cylinder.

5.2.2 Damping

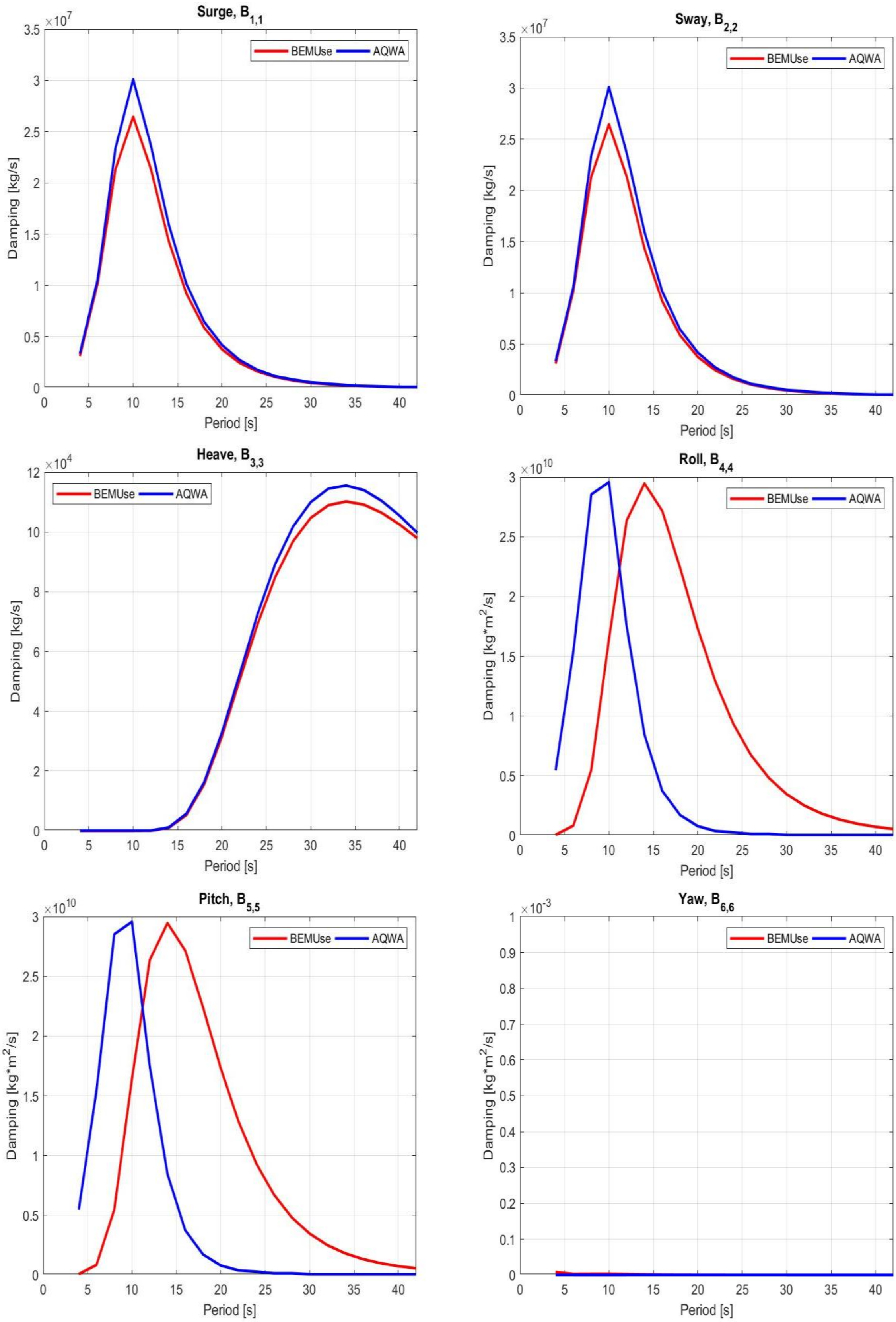

Figure 5.7. Damping comparison, cylinder.

5.2.3 Exciting forces and moments

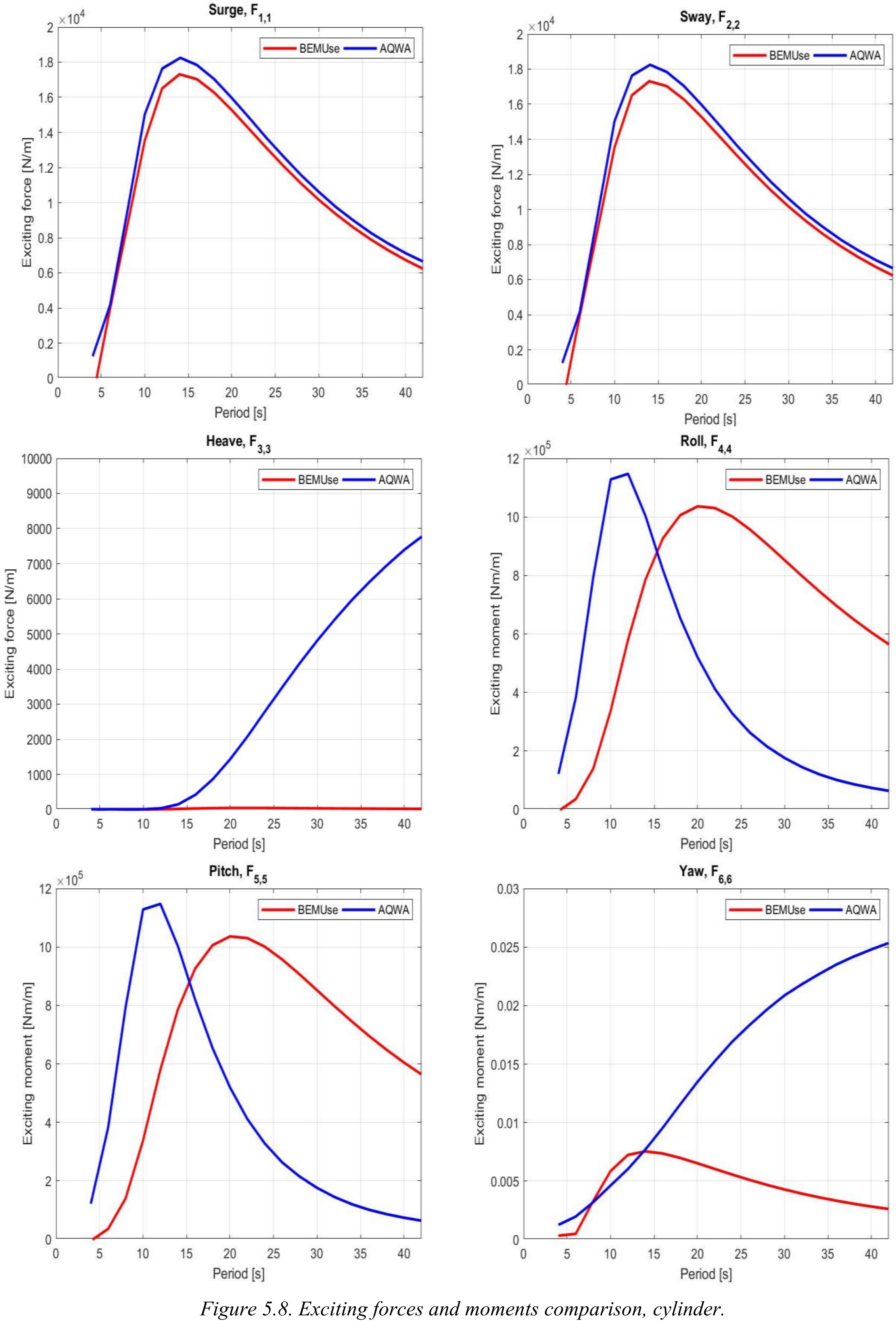

Figure 5.8. Exciting forces and moments comparison, cylinder.

5.2.4 Response Amplitude Operators

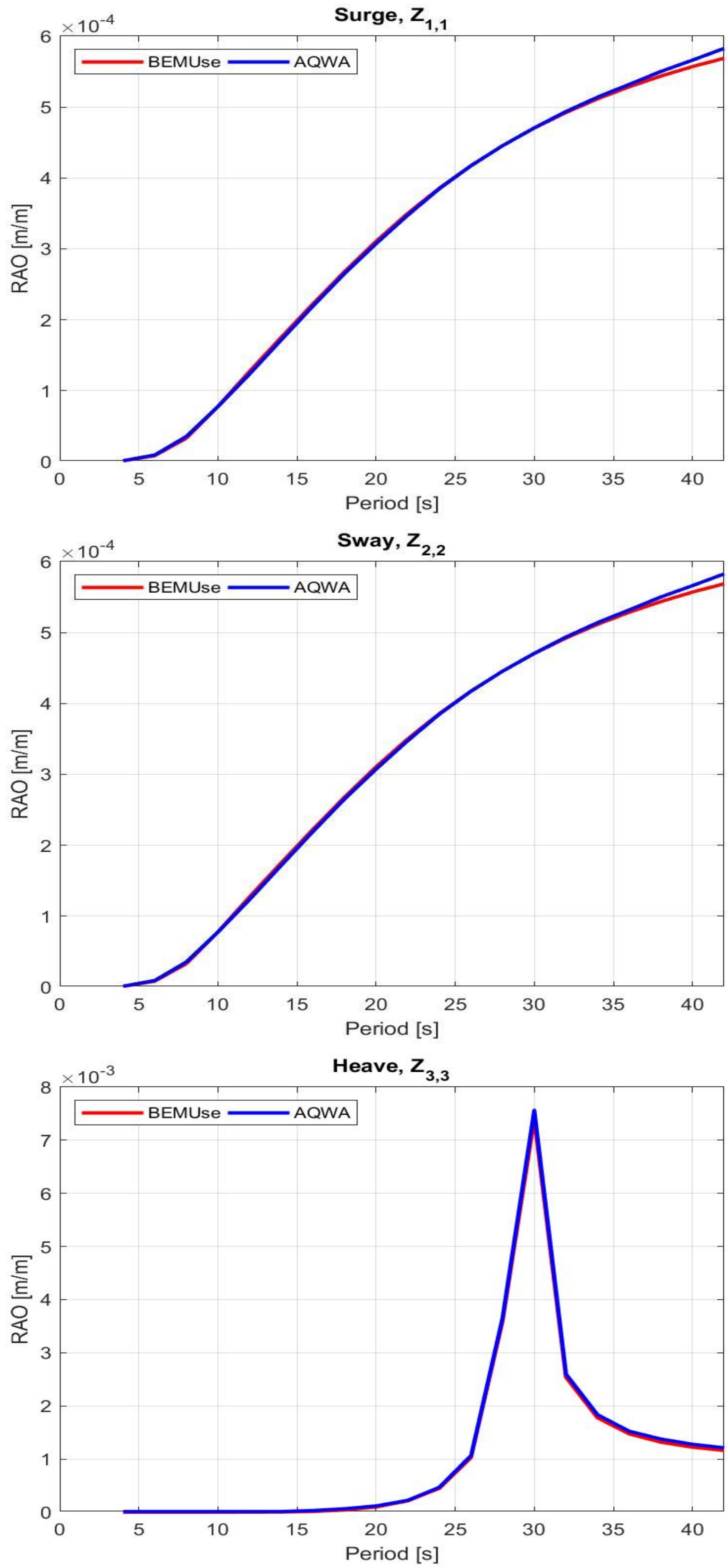

Figure 5.9. RAOs comparison, cylinder.

The results are quite surprising. For surge, sway and heave, the added mass plots show the same evolution for the two curves, but the numerical values obtained by BEMUse are approximately 10% lower than those of AQWA. This is probably due to different handling of the top of the geometry, which is not considered by AQWA but discretized in BEMUse. For roll, pitch and yaw, the differences in the two curves are more marked, with significant differences also in the shape.

The translational motions for damping agree almost perfectly between the two, while the rotational ones differ markedly both in the shape and values of the curves. The difference in outline is quite interesting though, as the two curves show similar behavior, but they peak at different frequencies.

The exciting forces that agree are only those for surge and sway, as heave has the unknown issues already encountered in WAMIT comparison, while roll, pitch and yaw do not coincide at all.

RAOs do instead agree almost perfectly for translational motions, while again, rotational ones haven't been compared.

5.3 BOX

The box already studied in the WAMIT comparison is studied with AQWA as well. All the geometrical and physical parameters are the same as before.

If the previous comparison had been more successful and the accordance more precise, the parallelepipedal geometry would not have been analyzed, considering the work redundant. Instead, as the issues encountered were more critical than expected, it has been thought better to compare the box as well, instead of turning the attention to other platforms of more practical interest. This choice, unfortunately, excluded from this thesis the analysis of the ISWEC platform, which is not a floating platform designed for wind turbines, but an innovative concept of a wave energy converter developed by a private company with a close collaboration with the Politecnico di Torino, which directly produces electricity from the motion of the waves.

This decision was made not only because of the reason just explained, but also because the data available for an analysis were not precise enough.

Anyway, the parallelepipedal box allows a further comparison between the three softwares, which is something probably more useful for the validation of a new hydrodynamic model.

The results for the four parameters considered are shown in the next plots.

5.3.1 Added mass

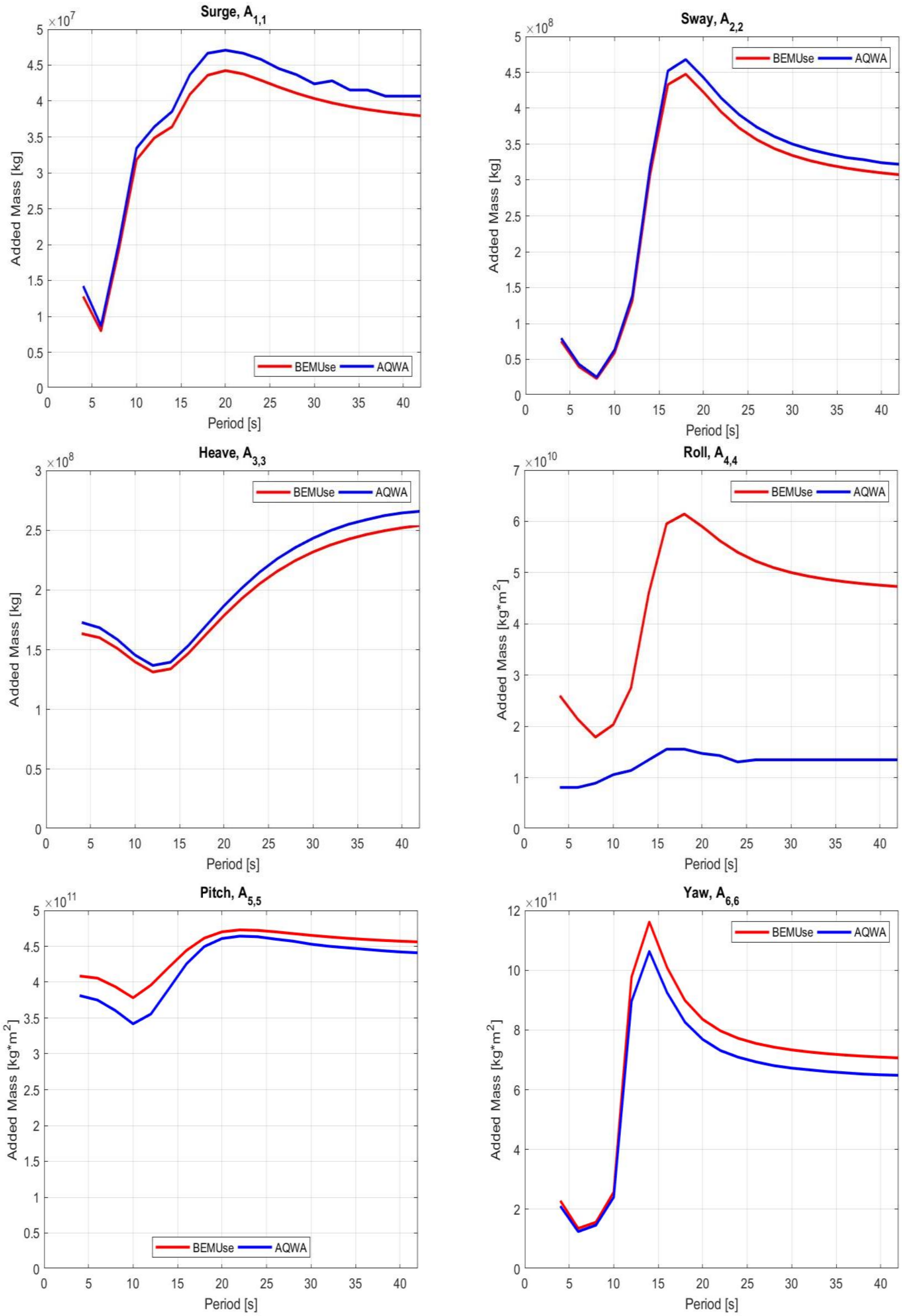

Figure 5.10. Added mass comparison, box.

5.3.2 Damping

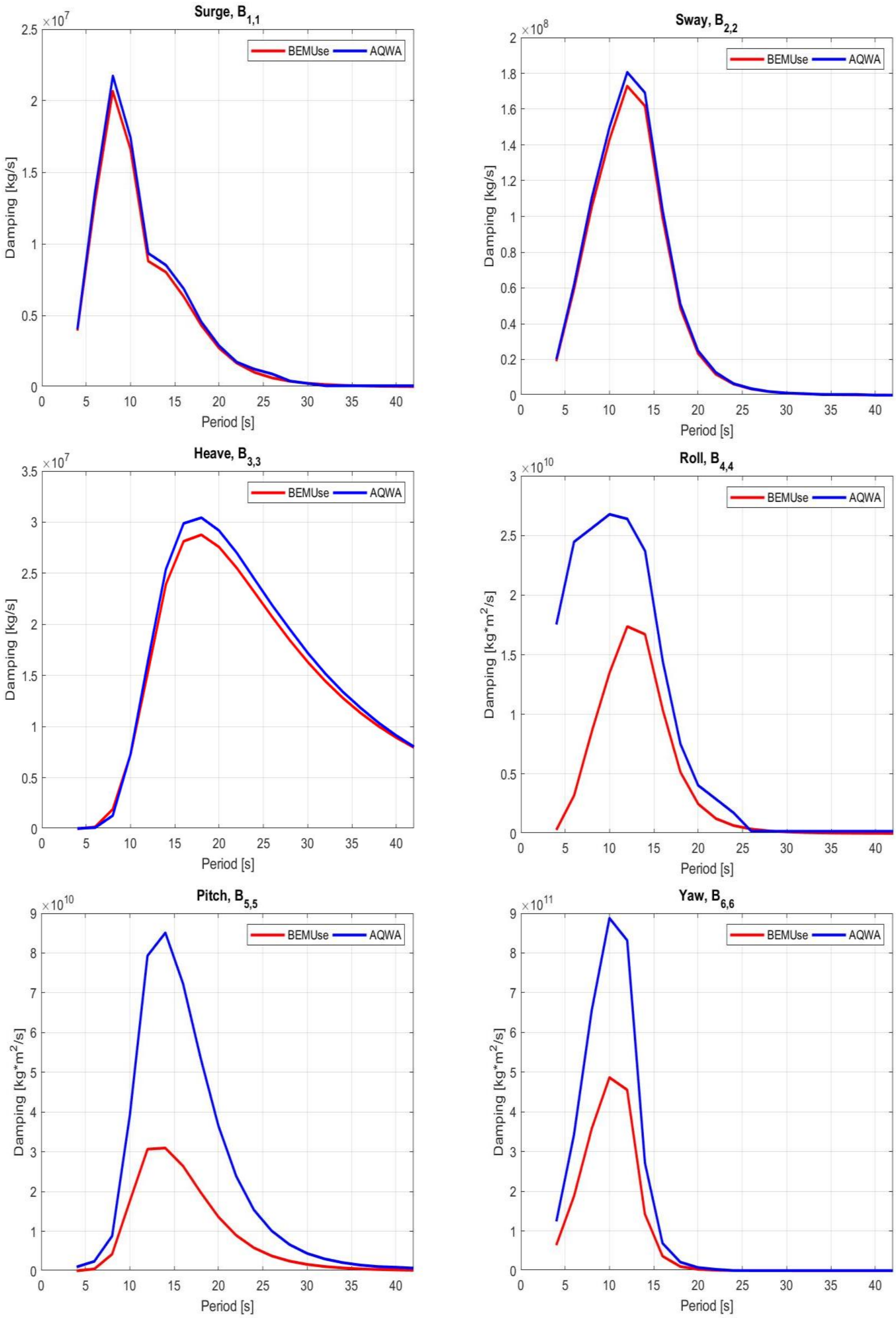

Figure 5.11. Damping comparison, box.

5.3.3 Exciting forces and moments

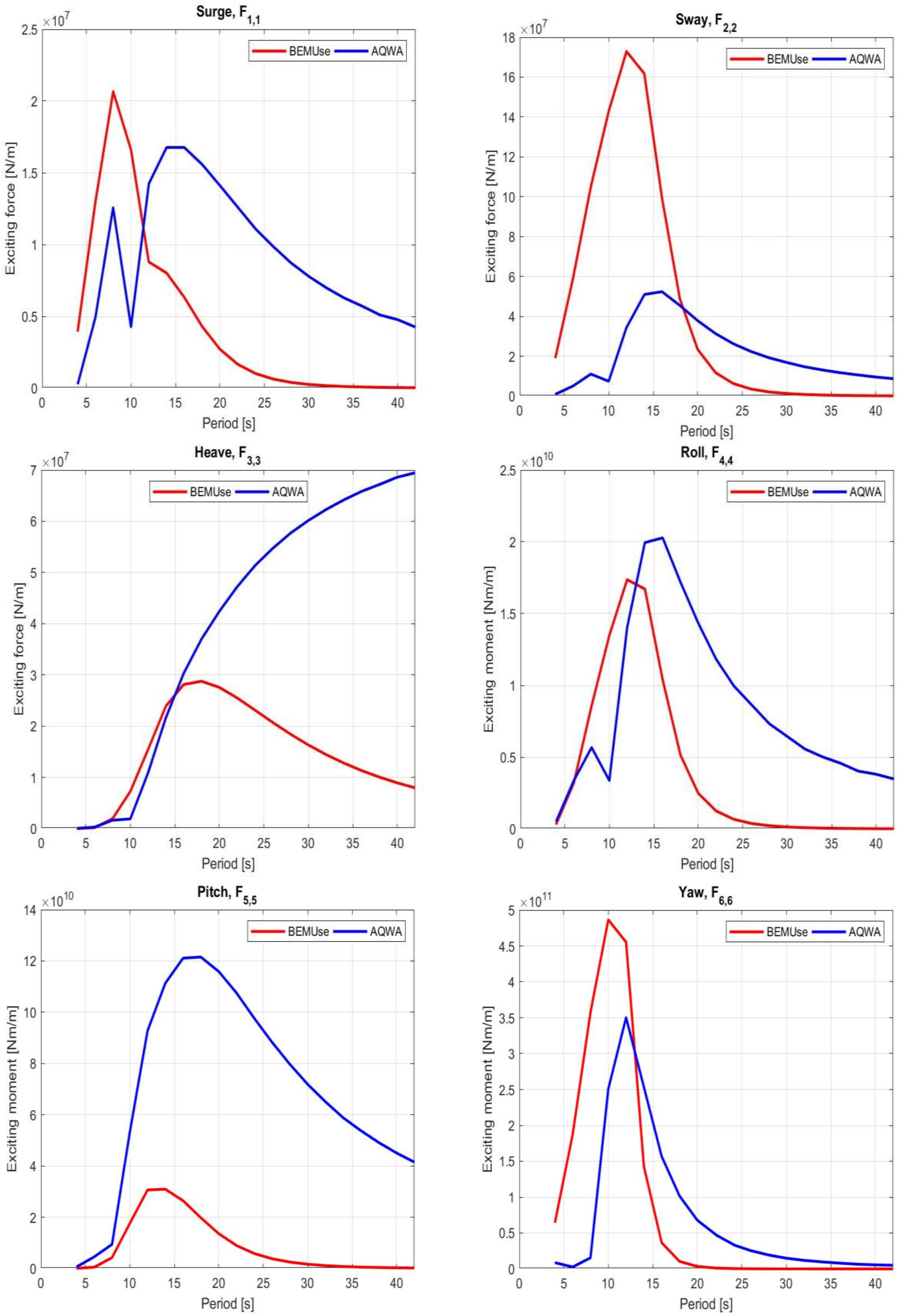

Figure 5.12. Exciting forces and moments comparison, box.

5.3.4 Response Amplitude Operators

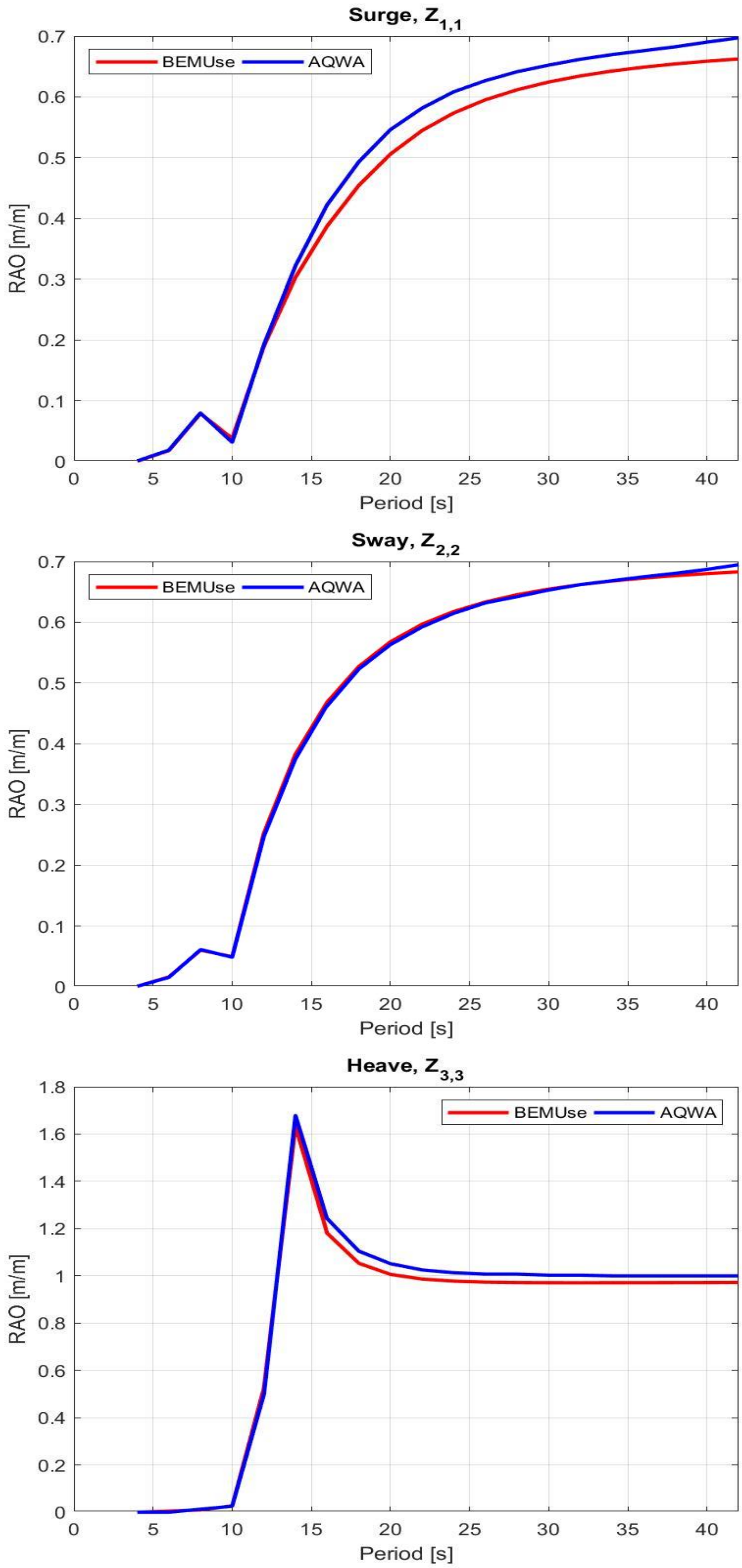

Figure 5.13. RAOs comparison, box.

For added mass, the results for surge, sway and heave agree closely between the two softwares. Unfortunately, there are no explanations for the behavior of the curve in the roll graph, while pitch and yaw show again a close agreement in form and values.

The same can be said for damping as well, but the differences between BEMUse and AQWA are more important than for added mass. In this case, the peak reached by the former in each plot is much lower than the one of the latter. Once again, the roll is the motion which gives more troubles.

Unfortunately, for the exciting forces none of the six motions agree, and the differences are marked. None of the curves agree with each other, with unexpected peaks and lows on all of them. Quite interestingly, though, this time it's the AQWA curves that show more irregularities. Anyways, further analysis should be carried out to try to understand what's wrong.

On the other hand, the RAOs for translational motions agree almost entirely, which is surprising as they derive directly from the other parameters. Again, only surge, sway and heave were studied.

5.4 OC3

Finally turning the attention on a test case of more practical importance, the choice fell on the OC3 platform for FOWT applications, as it is both easy to model - the shape is similar to a cylinder - and a promising design for commercial floating turbines.

Indeed, the OC3 platform is a spar-buoy type of platform 120 m high with a larger diameter of 4.7 m and the smaller of 3.7 m. The geometrical parameters of the platform are reported in the next table.

Physical parameter	Value
Depth to platform base below seawater level	120 m
Depth to top of taper below seawater level	4 m
Depth to bottom of taper below seawater level	12 m
Platform diameter above taper	6.5 m
Platform diameter below taper	9.4 m
Platform mass, including ballast	7 466 330 kg
Center of Mass location below seawater level	89.9155 m
Platform roll inertia about CoM	4 229 230 000 $kg \cdot m^2$
Platform pitch inertia about CoM	4 229 230 000 $kg \cdot m^2$
Platform yaw inertia about CoM	164 230 000 $kg \cdot m^2$

Table 5.1. Physical and geometrical parameters of the OC3 platform.

For this geometry, instead of the usual comparison with AQWA plots obtained directly on my calculator, the results obtained by BEMUse were compared against the paper published by Jonkman (2007) [32], which used AQWA himself in his study. This choice was made because getting the same results as the ones published by one of the leading experts on offshore platforms would mean a much more reliable validation than that obtained so far.

In the figure below, as done for all the other geometries, the geometry generated by BEMUse is reported. Except for the tapered part on top, the platform is basically a cylinder.

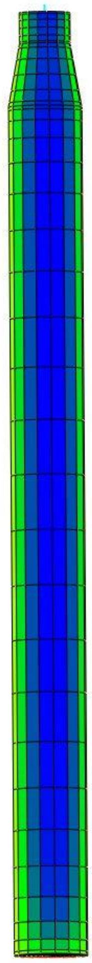

Figure 5.14. OC3 floating platform generated by BEMUse.

In this paper, only the results for added mass and damping were published, so the comparison could only be made for those parameters. The frequencies analyzed are different than the previous cases, as the values of the normalized frequency $\nu = \omega^2/g$ go from 0 to 5. Also in this analysis, the values of both added mass and damping are not normalized.

The results of the comparison are shown in the next couple of pages.

5.4.1 Added mass

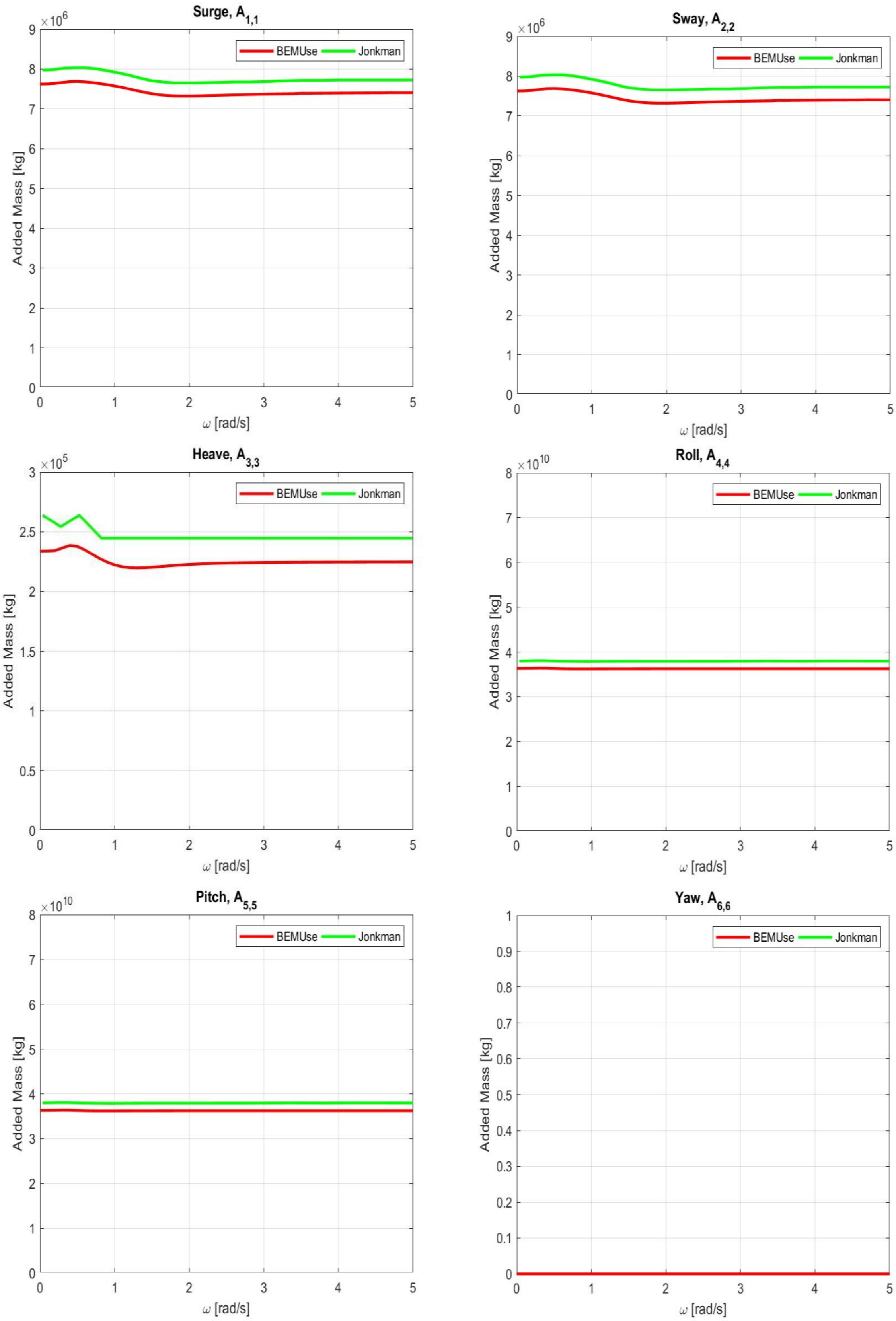

Figure 5.15. Added mass comparison, OC3.

5.4.2 Damping

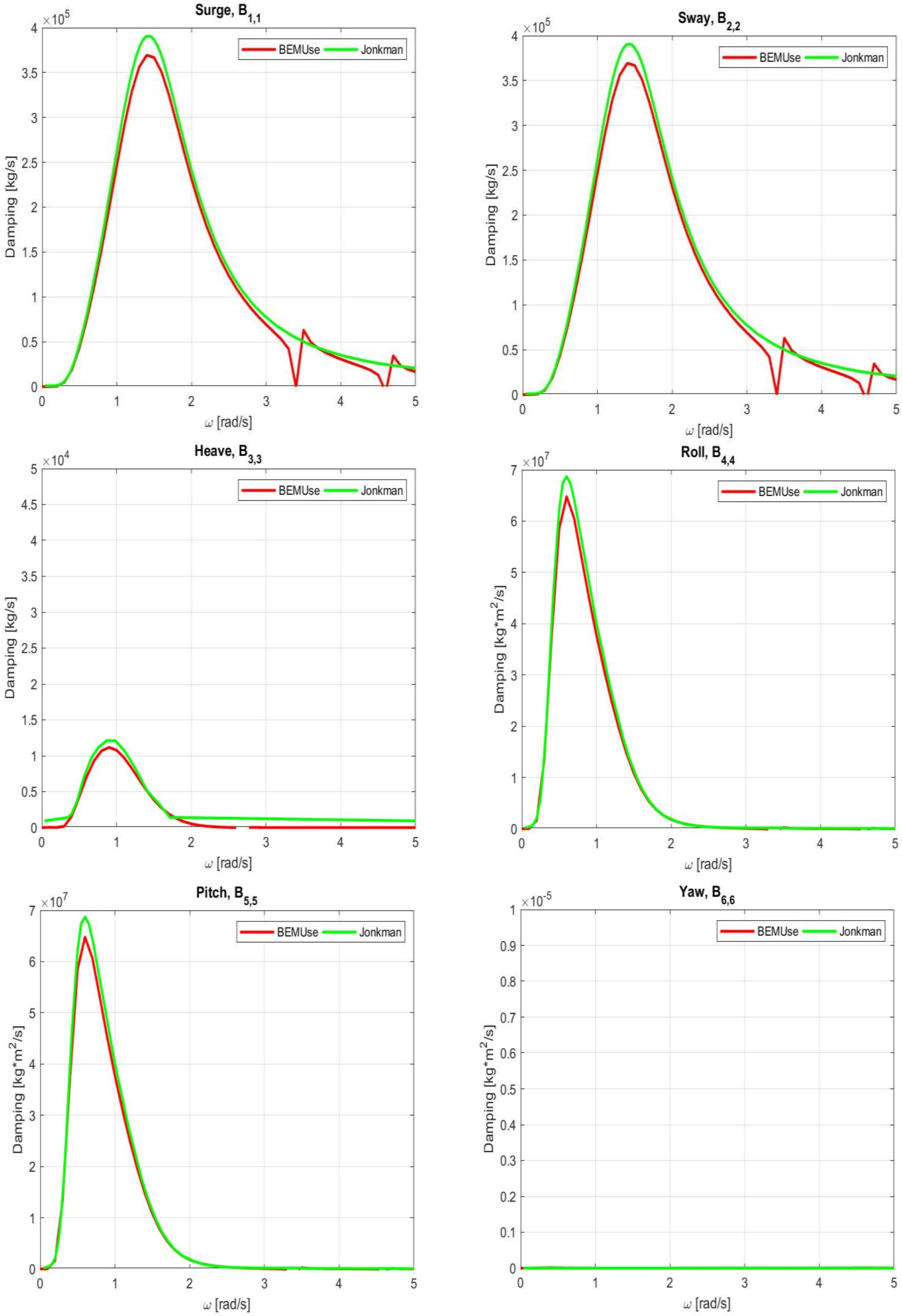

Figure 5.16. Damping comparison, OC3.

The first thing to make clear is that the reason why some of Jonkman's curves have sharp angles instead of smooth bends on the graphs is the way they were extracted from the plots published on the paper. The small figures, where all three translational motions on one and the rotational on the other were plotted together, didn't allow a precise acquisition of data. This is particularly evident in the heave plot for both added mass and damping.

The results of the comparison are satisfying. For added mass, the two curves show close similarity in shape, even though the numerical values obtained with BEMUse are slightly smaller than the reference ones for all the degrees of motion, but mainly for the translational ones. Various tries to solve this discrepancy couldn't find the reason why this difference is so marked.

In the damping plots, the two curves are much closer to each other on all the graphs. BEMUse's curves always have lower peaks, but the difference is less evident. For both surge and sway, at frequencies close to 3.5 and 4.5 *rad/s*, there are some unexpected irregularities on the BEMUse curves. These, due to some issues on the irregular frequency removal algorithm, are absent in Jonkman's plot.

Apart from these small issues, the comparison with the cited paper can be considered successful, even though only added mass and damping were considered.

6. CONCLUSION

As reported and explained in the previous chapters, this thesis had the objective to prove the validity and accuracy of BEMUse.

At the end of the tests, that target is successfully achieved, even though not completely.

6.1 WAMIT COMPARISON

Regarding the agreement of the BEMUse's results with WAMIT's, the curves are, for the most part, remarkably similar to each other, and they are even closer than initially expected. Added mass, damping, exciting forces except for heave motion, and the translational motions of RAOs agree almost perfectly for the three geometries under investigation. Some concerns remain on the four remaining parameters, which do not agree at all.

The reason for the errors in the rotational motions of RAOs is unfortunately unclear. RAOs are calculated directly from the other three parameters studied, as equation (3.38) states. Since all three of them are correct, it's uncertain why the BEMUse's results are so different.

It has necessarily got something to do with the definition of both the inertia matrix M and the hydrostatic restoring matrix C. Unfortunately, in the paper from which the test cases were taken, no explanation at all is given on how these two matrices were set. On BEMUse, on the other hand, they are configured precisely how the WAMIT User Manual [29] prescribes.

The definition of the two matrices is undoubtedly part of the problem, but it does not explain the sudden peaks that the researchers in Hull [30] found in their simulations, for all three geometries. This is because neither M nor C depend on the wave frequency ω, a factor that is necessary to explain these peaks.

The issues concerning the exciting force for the heave motion are unclear as well. For that, though, no explanatory hypothesis could be formulated.

Concerns also derive from the extensive unforeseen corrections needed to make the results of the two softwares agree. They were much broader than prescribed on the paper and, worst of all, were not consistent among the three geometries under investigation. This leads to the suspect that the results in the article were misreported, or at least the graphs have, in some cases, issues with the order of magnitude of the results. Another possibility is that there was some additional normalization made without a statement.

6.2 AQWA COMPARISON

The comparison with AQWA was less successful than the first one. The results never coincide as closely as they do with WAMIT, even though there are good similarities in the shape of the curves, which agree almost entirely in their evolution in both period and frequency in most cases.

Moreover, the numerical difference between the two is consistent, with BEMUse's results being often approximately up to 10% lower than AQWA's. One possible explanation of this could be the different way the two softwares treat the upper surface of the geometries studied, i.e. the surface at z = 0, the free water surface.

AQWA does not consider it since the geometries it uses are thin hollow surfaces obtained cutting solid bodies.

BEMUse, on the other hand, discretizes and creates panels on the top surface of each geometry, which then obviously are considered in the calculations. Subsequently, since the most significant contribution to the hydrodynamic parameters under investigation comes from near the free water surface, the difference between the two results surely depends on this.

For the same reason, as the mesh in AQWA is automatically generated and cannot be controlled by the user, the greater contribution near the body's edges and the water surface cannot be adequately taken into account as it is impossible to increase the mesh refinement near these particularly important areas.

Finally, it can be noted how the plots generated by AQWA show in some cases the effects of a non-optimal removal of irregular frequencies. These sudden peaks are not to be seen in BEMUse, as its removal procedure is, like the one in WAMIT, much more efficient.

The comparison with Jonkman (2007) [32] is considered successful and of particular importance, as it validates BEMUse on a geometry with practical applications in the field of FOWTs, against a paper published by one of the leading experts at NREL, the National Renewable Energy Laboratory in the USA.

Summarizing, the validation of BEMUse as a reliable hydrodynamic analysis software can be considered successful, as the results compare quite nicely with both WAMIT and AQWA. This is just the first step though, as there is plenty of work to be done before the library can be successfully and confidently incorporated inside QBlade. In the next chapter, the future objectives to be achieved in the development of BEMUse are briefly illustrated.

6.3 FUTURE WORK

The work of validation carried out in this thesis is just the first step in the development of a well-established and acknowledged hydrodynamic analysis model. However, the encouraging results of this study demonstrate the potential of BEMUse as an open-source, easy-to-use alternative to expensive softwares like AQWA and WAMIT.

Before being able to include it in QBlade, giving the users the possibility to simulate the behavior and the performance of FOWTs like they nowadays do with fixed-bottom turbines, BEMUse needs to undergo significant additional development. In this chapter, the next steps in its development are briefly assessed.

First, the issues faced during this work of validation need to be corrected. It's fundamental to understand why the exciting force for the heave motion is always wrong, and especially where is the issue with the RAOs for the rotational motions. Until then, this whole work of validation cannot be considered completely successful.

For the moment, all the simulations are carried out in the infinite-depth configuration, which does not consider the effect of the seafloor on the velocity potential. This is because the finite-depth case requires another form of the Green function, which is much more challenging to implement on a software.

Numerous researchers in recent years have faced this issue, and various solutions have been proposed. Liu, Iwashita, and Hu (2015) [33] suggests using different equations depending on the ratio between the characteristic length of the body to be studied and the water depth *h*. The four equations become progressively challenging to implement numerically as *h* increases, and the ratio consequently decreases.

Newman (1985) [15], on the other hand, proposes one single equation to be used, no matter how deep the water is. The problem is that for reasons of computational efficiency, he transforms the integral of the Green function in a sum, whose rate of convergence depends again on the ratio *L/h*. This series is practically useless for small values of *L/h* since each summand contains a logarithmic singularity when *L/h* tends to 0. Moreover, it's been proven that the number of terms required in the sum for a given accuracy is proportional to *h/L*, which means that the computational cost of the calculation increases rapidly.

Chen (2018) [34] recently proposed a new and improved formulation of the sum computed by Newman, but the issues are not solved, and therefore, the computational cost is still very high. Additionally, Chen proposed a sum formulation also for the derivative of the Green's functions both in the horizontal direction and in the vertical one. When trying to implement Chen's sums in BEMUse, the results were quite correct even though they didn't converge to 0 when the wave angular frequency ω was 0.

For the moment, BEMUse only calculates first-order forces and moments. Once the previous two improvements will be completed, the second-order problem also needs to be implemented in the model. Second-order waves are generated from the quadratic interaction of two linear wave components in the discrete spectrum. The second-order problem is much more challenging to study and implement because of the increased complexity of the solving equations.

There are a lot of other features that need to be added in BEMUse before it could confidently be used in place of other hydrodynamic modeling softwares. This chapter only gave an idea of where the work at Hermann-Föttinger-Institut will focus in the near future to soon provide a reliable, efficient and free-to-use hydrodynamic analysis model.

Humanity cannot afford to wait anymore to change the energy sources on which to rely on, and my hope is that BEMUse will soon help with the research on FOWTs, which have the potential to become one of the leading technologies in the urgent transition to a fossil-free world.

7. BIBLIOGRAPHY

[1] Global Wind Energy Council. 2017. "Global Wind Energy Report: Annual Market Update 2017."

[2] https://www.ge.com/renewableenergy (Website). 2017. "Haliade-X Offshore wind turbine platform." https://www.ge.com/renewableenergy/wind-energy/offshore-wind/haliade-x-offshore-turbine

[3] Boccard, N. 2009. "Capacity Factor of Wind Power Realized Values vs. Estimates." *Energy Policy* 37(7):2679–88.

[4] Sclavounos P. D. 2007. "Floating Wind Turbines." *Lecture presentation*. Massachusetts Institute of Technology, USA.

[5] Musial, W., Butterfield, S., and Boone, A. 2004. "Feasibility of Floating Platform Systems for Wind Turbines." *Collection of ASME Wind Energy Symposium Technical Papers AIAA Aerospace Sciences Meeting and Exhibit* (November 2003):476–86.

[6] Golbert, D. R., Blanco, P. J., Clausse, A., and Feijóo, R. A. 2016. "Corrigendum to 'On the Search of More Stable Second-Order Lattice-Boltzmann Schemes in Confined Flows' [J. Comp. Phys. 294 (2015) 605-618] Doi: 10.1016/j.Jcp.2015.03.065." *Journal of Computational Physics* 311(June):374.

[7] https://pmiind.com (Website). Burger T. 2016. "Pros and Cons of Floating Platforms in Marine Renewable Energy." https://pmiind.com/pros-cons-floating-platforms-marine-renewable-energy/

[8] Myhr, A., Bjerkseter, C., Ågotnes, A., and Nygaard, T. A. 2014. "Levelised Cost of Energy for Offshore Floating Wind Turbines in a Lifecycle Perspective." *Renewable Energy* 66:714–28.

[9] Lazard. 2018. "Lazard's Levelized Cost of Storage Analysis — Version 12.0." *Lazard's Levelized Cost of Storage - Version 12.0* (November):0–19.

[10] Babarit, A., Delhommeau, G. 2015. "Theoretical and Numerical Aspects of the Open Source BEM Solver NEMOH." *Proceedings of the 11th European Wave and Tidal Energy Conference.* (September 2015):1–12.

[11] Penalba, M., Kelly, T., and Ringwood, J. V. 2017. "Using NEMOH for Modelling Wave Energy Converters : A Comparative Study with WAMIT." *12th European Wave and Tidal Energy Conference* 10.

[12] Lee, C. H. 1995. "WAMIT Theory Manual." *WAMIT Theory Manual* 1–19.

[13] Newman, J. N. 1999. "Marine Hydrodynamics." *Marine Hydrodynamics* 3–5. Maple-Vail, Inc. Massachussets Institute of Technology. USA.

[14] Wehausen, J. V. and Laitone, E. V. 1960. "Surface waves." *Handbuch der Physik*: 9, 446-778. Springer, Berlin.

[15] Newman, J. N. 1985. "Algorithms for the Free-Surface Green Function." *Journal of Engineering Mathematics* 19(1):57–67.

[16] Newman, J. N. 1992. "The approximation of free-surface Green functions". *Wave Asymptotics.* P. A. Martin & G. R. Wickham, editors, Cambridge University Press.

[17] Newman, J. N., Sclavounos, P. D. 1988. “The computation of wave loads on large offshore structures.” *5th International Conference on the Behaviour of Offshore Structures*. Trondheim.

[18] Newman, J. N. 1993. “Note on bodies and panels in the free surface.” Unpublished report.

[19] Zhu, X. 1994. “Irregular Frequency Removal from the Boundary Integral Equation for the Wave-Body Problem.” *MSc Thesis*. Dept. of Ocean Eng., Massachussetts Institute of Technology. USA.

[20] Lee, C. H., Newman, J. N., and Zhu, X. 1996. “An Extended Boundary Integral Equation Method for the Removal of Irregular Frequency Effects.” *International Journal for Numerical Methods in Fluids* 23(7):637–60.

[21] van Garrel, A. 2016. “Multilevel panel method for wind turbine rotor flow simulations.” *PhD Thesis.* University of Twente.

[22] van Garrel, A. 2003“Development of a Wind Turbine Aerodynamics Simulation Module.” *ECN-C--03-079*. Energy research Centre of the Netherlands, 2003.

[23] Newman, J. N. 1986. “Distributions of sources and normal dipoles over a quadrilateral panel.” *Journal of Engineering Mathematics*, 20(2):113–126.

[24] Laforce, T. and June, C. A. 2006. “PE281 Boundary Element Method Course Notes.” *Tara* (June):1–12.

[25] Costabel, M. 1987. “Principles of Boundary Element Methods.” *Computer Physics Reports* 6(1–6):243–74.

[26] Edwards, E. N.d. “Introduction to the Linear Panel Method.” *Lecture notes.*

[27] Liang, H., Wu, H., and Noblesse, F. 2018. “Validation of a Global Approximation for Wave Diffraction-Radiation in Deep Water.” *Applied Ocean Research* 74(May):80–86.

[28] Baghfalaki, M., Das, S. K., and Das, S. N. 2012. “Analytical Model to Determine Response Amplitude Operator of a Floating Body for Coupled Roll and Yaw Motions and Frequency-Based Analysis.” *International Journal of Applied Mechanics* 4(4).

[29] WAMIT, Inc. n.d. “WAMIT 6.2 User Manual.” *WAMIT 6.2 User Manual* 4.1–4.8.

[30] McDermott, R.J. 2000. “WAMIT-MOSES Hydrodynamic Analysis Comparison Study.” (July):1–30.

[31] Eatock Taylor, R., and Jefferys, E. R. 1986. “Variability of Hydrodynamic Load Predictions for a Tension Leg Platform.” *Ocean Engineering* 13(5):449–90.

[32] Jonkman, J. M. 2007. “Dynamics Modeling and Loads Analysis of an Offshore.” *NREL* (November).

[33] Liu, Y., Iwashita, H., and Hu, C. 2015. “A Calculation Method for Finite Depth Free-Surface Green Function.” *International Journal of Naval Architecture and Ocean Engineering* 7(2):375–89.

[34] Chen, Z. 2018. “New Formulation of the Finite Depth Free Surface Green Function.”

ACKNOWLEDGMENTS

First, I want to thank my supervisor at TU Berlin, Joseph Saverin, for the chance he gave me. Working on my thesis in such a prestigious university was the perfect ending to my academic career. Your help and support were fundamental during the nine months we worked together, and I genuinely appreciate all the time you spent tutoring me.

Special thanks are also due to Ing. Giovanni Bracco, who was supportive and present from Torino every time I needed him. Not only did you allow me to live this abroad experience, but as a final gift you helped me find the perfect job for the beginning of my working career, and I will be forever thankful for that.

After six hard years of studying, there are plenty of people that I want to thank for sharing this important period of my life with me.

And how can I not start with my parents? Dear Papi and Mami, your unconditional support has been invaluable. You've always let me organize and live my life as I wanted to, allowing me to make my mistakes and learn from them; but in the time of need, I always knew I could count on your help and support. You have two very different ways to show it, but I know you are there for me no matter what. You even backed me up when a crazy idea that involved guns and lethal animals recently brought me to South Africa. Even in my wildest dreams, I could not have hoped for better parents.

Dear Gogo, you worked hard and took bold choices to get where you are now. I'm incredibly happy and proud of what you are achieving. You taught me a lot about what it takes to reach your dreams, and I'm thankful for all the help and the advice you manage to give me even living far away. I'm sure that you will get wherever you want to go with your life, and I will always be by your side.

Dear Anna, all the hard work and the efforts you put on a daily basis are truly inspirational. You manage to succeed in a tough field of study while spending so much time and energy on your biggest passion. Maybe I don't say it too often, but I'm so proud of the young woman you've become, and you can always count on my help when you need it, never forget that. Thank you for teaching me that for our biggest passions, all the sacrifices are more than worth doing; and thanks for all the big and little things you do for me, I notice them all, even if sometimes I fail to show it.

There are then so many good friends in my life, incredible people that make my life incredible.

Thank you, Alice, for all the late-night talks in my car, discussing life, travels, and many other crazy ideas. Thank you for always being present in my life, no matter how far from each other we were. Our friendship is truly one that will survive distances and time unscathed.

Thanks to Simone and Giorgio, my best friends. I don't think there is much to add; I can't wait to build new unforgettable memories with you.

Thanks to Stefano, Emanuele, Marco, and all the other members of 'La Plaza'. You tried so hard to make me fail my exams, and I'm happy you didn't succeed in that. But you are the best group for a fun night or a nightmare car trip. together, we rarely get where we thought we would, but we always end up with a cool story to tell afterward.

Thanks to the members of the legendary ‘GruppOtto’, you all made my last year at Politecnico by far the best one. A very special mention is due to Marta. Even though we will never end up being Instagram superstars partying in Porto Cervo, I’m so happy you decided to leave the beautiful Rome to come to the much nicer Torino. But I’m even happier you chose to pursue a career in engineering, instead of one in plant caregiving: that would have been a complete disaster.

Thank you, Stefano, because as you never fail to remind me, I would have never graduated without all your help, your wisdom, and, most importantly, your notes. You just started the most incredible and rewarding period of your life: Margherita is so lucky to have you as a father. No matter how many obstacles life throws at the three of you, you will go through everything.

Finally, I want to thank all the kids I’ve trained during these six years. No matter how bad my day had been, or how tired I was, you never failed to remind me that life can be much simpler, if you look at it with the smile and the lightheartedness of a child. I’m firmly convinced you taught me way more than what I taught you.

There are so many other extraordinary people in my life, great friends with whom I enjoy sharing a beer, an ice cream, or just some time together. My life is much richer with you in it. Thank you for sharing this journey with me, and thank you for being here with me today. I can’t wait to see what life has in store for us next.

Vittorio